CURRENT DRIVEN DYNAMICS OF MAGNETIC DOMAIN WALLS IN PERMALLOY NANOWIRES

A DISSERTATION
SUBMITTED TO THE DEPARTMENT OF MATERIALS
SCIENCE AND ENGINEERING
AND THE COMMITTEE ON GRADUATE STUDIES
OF STANFORD UNIVERSITY
IN PARTIAL FULFILLMENT OF THE REQUIREMENTS
FOR THE DEGREE OF
DOCTOR OF PHILOSOPHY

Masamitsu Hayashi
December 2006

I certify that I have read this dissertation and that, in my opinion, it is fully adequate in scope and quality as a dissertation for the degree of Doctor of Philosophy.

(James S. Harris) Principal Co-Advisor

I certify that I have read this dissertation and that, in my opinion, it is fully adequate in scope and quality as a dissertation for the degree of Doctor of Philosophy.

(Stuart S. P. Parkin) Principal Co-Advisor

I certify that I have read this dissertation and that, in my opinion, it is fully adequate in scope and quality as a dissertation for the degree of Doctor of Philosophy.

(Robert Sinclair)

I certify that I have read this dissertation and that, in my opinion, it is fully adequate in scope and quality as a dissertation for the degree of Doctor of Philosophy.

(Robert L. White)

Approved for the University Committee on Graduate Studies.

preface

The significant advances in micro-fabrication techniques opened the door to access interesting properties in solid state physics. With regard to magnetic materials, geometrical confinement of magnetic structures alters the defining parameters that govern magnetism. For example, development of single domain nano-pillars made from magnetic multilayers led to the discovery of electrical current controlled magnetization switching, which revealed the existence of spin transfer torque.

Magnetic domain walls (DWs) are boundaries in magnetic materials that divide regions with distinct magnetization directions. DWs play an important role in the magnetization reversal processes of both bulk and thin film magnetic materials. The motion of DW is conventionally controlled by magnetic fields. Recently, it has been proposed that spin polarized current passed across the DW can also control the motion of DWs. Current in most magnetic materials is spin-polarized, due to spin-dependent scattering of the electrons, and thus can deliver spin angular momentum to the DW, providing a "spin transfer" torque on the DW which leads to DW motion. In addition, owing to the development of micro-fabrication techniques, geometrical confinement of magnetic materials enabled to create and manipulate a "single" DW in magnetic nanostructures. New paradigms for DW-based devices are made possible by the direct manipulation of DWs using spin polarized electrical current through spin transfer torque.

This dissertation covers research on current induced DW motion in magnetic nanowires. Fascinating effects arising from the interplay between DWs with spin polarized current will be revealed.

Acknowledgement

First, I would like to thank Dr. Stuart Parkin for giving me an opportunity to work in his lab at IBM Almaden Research Center. It was a great pleasure to conduct research under his supervision. He also provided me with insights of the political world of research, which I very much enjoyed to hear about. I would also like to thank my co-supervisor, Professor James Harris for his encouragement and kindness during my time at Stanford. I am indebted to Luc Thomas, who has been my mentor at IBM and taught me how to conduct research as well as to move domain walls.

In addition, I would like to thank Professor Robert Sinclair for serving on my thesis committee and for his class on crystallography, which provided me with the fundamentals of materials science. I am grateful to Professor Robert White who also served on my thesis committee and his deep understanding on magnetism.

I acknowledge Professor Bruce Clemens and Professor David Goldhaber-Gordon for serving on my defense committee, Stephanie Sorensen and Doris Chan for helping me on all the administrative issues and Gail Chun-Creech for her kind support on arranging schedules with Coach. I'm grateful to all the faculties, staff members and my friends at the Department of Materials Science and Engineering at Stanford University.

This work would not be possible without the support by Charlie Rettner, who provided me with excellent samples and some slang to characterize the unimaginable effort put for making devices. I also thank Rai Moriya and Xin Jiang for their professional support in sample preparation.

I acknowledge Yaroslaw Bazaliy, who provided fundamental insights to the underlying physics involved in this project. On a similar note, I am grateful to Anthony

Ndirango for sharing his deep understanding in all area of physics.

I thank the staff members in the Parkin research group: Mahesh Samant for managing all the equipments in the lab, Kevin Roche for his indispensable knowledge on softwares and controlling electronic devices and Sally Floyd and Liz Fedde for helping me on IBM's complicated human resource problems.

I acknowledge the other members in the Parkin research group: Bastiaan Bergman for his insights to optical measurement setups and also for being my best officemate, See-hun Yang for his support in sample deposition and his entertaining discussions on papers waiting to be submitted, Brian Hughes for maintaining the deposition systems and humorous opinions at everyday lunch, Hyunsoo Yang for sharing his knowledge on analog circuit and also for car-pooling to save gas, Li Gao for his advice on my job search, Genole Jan for his deep understanding on materials and mechanics, Rekha Rajaram for the template tex file which was critical in writing this dissertation and Nicholas Weiss for his advices on building systems and warnings on filing the tax claims. I also thank the past members in the Parkin research group: Alex Panchula, Christian Kaiser, Roger Wang and Andreas Ney. I wish good luck for Justin Brockman as he started his PhD project at IBM. I thank Larry Lindabauer, Rob Polini, Bob Erickson, Manny Hernandez, Dave Altknecht and all the other members of model shop for their incredible support on mechanics and electronics.

Finally, I thank my family, in particular, my parents for their patience and understanding. I thank my brother for his optimistic view of life. Last, and furthest from least, I thank my wife Michiko for all her support and encouragement.

Contents

Chapter 1

Introduction

1.1 Magnetic domain walls

Magnetic domain walls (DWs)[1] are boundaries in magnetic materials that divide regions with distinct magnetization directions. DWs play an important role in the magnetization reversal processes of both bulk and thin film magnetic materials and consequently have been intensively studied for many decades.

In the mid 1960s and 1970s, substantial research effort was conducted to understand the physics of the motion of DWs in thin films, because DWs were considered to be important for potential memory and logic devices. The materials that were most extensively investigated were magnetic oxides, in particular, the orthoferrites and ferrimagnetic garnets[2]. These materials are called ”magnetic bubble” materials because of the form of the magnetic domains that they form.

There was a substantial theoretical effort to describe and understand the dynamics of magnetic bubble domains in the late 1960s [3, 4]. These theories were based on the phenomenological Landau-Lifshitz (LL) or Landau-Lifshitz-Gilbert (LLG) equations. The agreement found between the theoretical predictions and descriptions of the magnetization dynamics of magnetic bubbles and experimental results from that period are remarkable. Indeed, the basis of DW dynamics was firmly established at this time.

However, most of the bubble material based devices, particularly bubble memories, either did not make it or did not survive long in the marketplace. This was partly because other technologies, in particular commercially available hard disk drives and other solid state memories, outpaced bubble memories both in performance and cost. In addition, there were also some technical issues and limitations with bubble based devices. Since most of these devices were based on the controlled motion of bubbles using magnetic fields, electromagnets were needed to generate magnetic fields, which required a lot of space. The other problem was the speed of operation. Since the bubbles had to be moved to be written or to be read, the operational speed of such devices was limited by how fast these bubbles could move.

The phenomenon of magnetization switching has been investigated intensively over the past several decades, particularly with regard to storage device applications. The first prototype of magnetic random access memory (MRAM) used current passing through metal wires to generate local magnetic fields to switch the magnetization direction of the targeted memory element which was arranged in a crosss-point array[5]. The writing performance of this device (∼2.5 ns) was limited by the CMOS electronic circuit speed rather than any fundamental limitation of the magnetic switching process itself. Indeed, it has been shown that magnetic devices can be switched very rapidly by tuning the magnetic field pulse length to the precession frequency of the magnetic element. Using this approach a magnetization switching time of less than 200 ps has been demonstrated [6, 7], although even shorter switching times, approximately one hundred times smaller, have been demonstrated using sophisticated synchrotron based techniques [8, 9].

In modern MRAM devices, which are based on magnetic tunnel junction (MTJ) storage elements, it is not the switching time that is a problem but rather the generation of sufficiently large magnetic fields without the need for excessive and impractical currents. The field to switch such MRAM elements can be reduced by design of the MTJ element but this can lead to poor thermal stability of such elements due to the superparamagnetic effect. The thermal instability of these magnetic elements can be improved by magnetic engineering, particularly by replacing the magnetic layers in the MTJ device with anti-ferromagnetically coupled magnetic bilayers. The bilayers have smaller net magnetic moments but allow for larger magnetic anisotropies of the component layers. When the storage layer is comprised of such a bilayer, the state of this layer may be switched using a special sequence of magnetic fields, commonly termed toggle mode switching [10, 11, 12]. This mode of switching is particularly useful in stabilizing half-selected devices against thermal fluctuations but scaling of this approach will not allow it to be used for devices beyond the 45 nm technology node. More recently, current induced magnetization switching of MTJ devices has been studied as an alternative to magnetic field induced switching and is generally believed to have great potential for highly dense MRAM. This concept is discussed in the following section in more detail.

Several other possible methods of switching magnetic nanodevices without the use of magnetic fields have been reported. These methods include magneto-optical interactions and electric field phenomena. For example, in ferrimagnetic oxides, magnetization switching has been demonstrated using the inverse Faraday effect by shining photons onto the magnetic layer [13, 14]. The switching speed is extremely fast - of the order of few hundred femto-seconds - but the magnitude of the effect is typically quite small. For details of such magneto-optical effects, see references [15, 16, 17]. By changing the carrier concentration in the ferromagnetic semiconductor (GaMnAs), magnetization switching was achieved [18, 19]. Current induced domain wall motion in this material has also been reported as will be discussed below.

1.1.1 Current induced domain wall motion

Current in most magnetic materials is spin-polarized due to spin-dependent scattering of the electrons. In highly spin polarized materials, the direction of the conduction electron spin can be assumed to be aligned with the direction of the local magnetic moments at equilibrium. In Co and Ni the electron spin is aligned parallel with the magnetization (majority spin direction) whereas in Fe the electron spin is aligned in the opposite direction (minority spin direction)[20]. Thus, when an electron crosses a DW, it changes its spin direction from the magnetization direction of the domain where the electron originated to the magnetization direction of the domain which it enters. The change in the electron spin direction can be regarded as a change in the angular momentum of the system. To conserve angular momentum, this change in the angular momentum must be compensated by some other means. The concept of spin transfer driven DW motion assumes that the change in this angular momentum is compensated by motion of the DW. That is, the angular momentum that is transferred from the electrons causes a change in the direction of the local magnetization moments, which results in DW motion.

This concept was first proposed by Berger in 1984 [21, 22]. Berger described this as an exchange interaction between the electrons and the DW and performed a number of experiments to study the effect of the current on DWs [23, 24, 25, 26, 27]. Microseconds long DC current pulses were applied to unpatterned NiFe thin films and the motion of DWs was detected using the Faraday effect. Current densities of $10^5 - 10^8 A/cm^2$ were needed to observe DW motion, with DW displacements observed of up to ~14 μm.

All of the aforementioned works were carried out using relatively thick NiFe films (sim100-800 nm). One of the difficulties in studying current induced DW motion in thick NiFe films is that, in addition to the exchange interaction, other current induced effects can take place that may cause DW motion. Eddy current and self-field effects[27] become increasingly dominant as the film thickness is increased. In addition, the presence of DWs can cause the current flow to be distorted by either the normal or the anomalous Hall effect. These Hall effects generate a local magnetic field that can cause DW motion. This effect was predicted by Berger [28, 29] as a hydromagnetic domain drag and was confirmed experimentally in perpendicularly magnetized CoGdAu films [30, 31]. Thicker films typically result in more complex extended DW structures which may include, for example, Bloch lines, Bloch points and cross tie walls. These different magnetic configurations complicate the DW motion, which may therefore be difficult to analyze. Furthermore, in extended films, random pinning may cause the DWs to be distorted when driven by current and/or field, which also affect the DW motion. Thus extended thick films are not the best system to study the effect of current on DW motion. Nevertheless, these pioneering studies of Berger *et al.* established the basic notion of current induced DW motion.

In 1996, Slonczewski predicted that a flow of spin polarized current can exert torque, or spin transfer torque, on magnetic moments and consequently can reverse the magnetization direction[32]. This prediction was confirmed experimentally by Tsoi et.al.[33] and by Myers et.al.[34] in point contact geometries in multilayer films. Later, current induced magnetization reversal was also observed in a homogeneous system where magnetic multilayers which were patterned into nanopillars with cross-sections of the order of 100×100 nm^2[35]. In order to observe the spin transfer torque effect, it is important to reduce the effect of the self field which is generated by the current passing through the system. When the self field becomes too large it can influence the direction of the magnetic moments so complicating the reversal process. Since the self field increases with the size (radius) of the nanopillars it's role can be minimized by reducing the size of the nanopillars (or nanowires). Typically, nanopillars need to be less than ∼100 nm in diameter for the self-field to be smaller than that of the current. Thus advances in micro-fabrication techniques are indispensable to studies of current induced magnetic moment switching.

Partly triggered by the recent experiments on current induced magnetization reversal in spin-valve nanopillars, current induced domain wall motion has again attracted interest, this time not in extended films but rather in magnetic nanowires. The nanowires are typically formed from a soft magnetic material (e.g. permalloy, Ni_81Fe_19) and are patterned using modern lithographic techniques. Since the width of permalloy nanowires can be made smaller than that of domain walls in permalloy, it is possible to create a single DW across the nanowire. In addition, since the cross sectional area of the nanowire is reduced, self field and eddy current effects can be minimized. Thus magnetic nanowires are ideal systems to study current induced domain wall motion.

There have been a number of reports of the observation of current induced DWs in magnetic nanowires. Nanowires patterned from single layer permalloy films are used in most of these studies [36, 37, 38, 39, 40], where the (critical) current density needed to move the DW is reported to be $\sim 5 \times 10^7 - 5 \times 10^8$ A/cm^2. Magnetic multilayers exhibiting giant magnetoresistance (GMR) effects have also been used to study DW motion in permalloy layers [41, 42], although in a much smaller number of studies. Surprisingly, the critical current density has been reported to be orders of magnitude lower than in the single layer permalloy nanowires. It is not clear why this would be the case. Other materials, including the ferromagnetic semiconductor GaMnAs[43], electroplated Ni nanowires [44, 45], CoFe [46] and CoPt [47, 48] nanowires have also been studied. The critical current density for GaMnAs is extremely low near its Curie temperature (~90 K), typically of the order of $\sim 10^5 - 10^6$ A/cm^2. This is partly attributed to its much lower saturation magnetization compared to permalloy; theory predicts that the critical current should be proportional to the saturation magnetization if nothing else changes (e.g. the spin polarization of the electrical current). However, the origin of such low critical current density is not clear, although theoretical explications are under development[49].

Reports on the theoretical description of current induced DW motion [50, 51, 52, 53, 54, 55, 56, 57, 58, 59, 60, 61, 62] have increased since the recent interest in experimental studies of the phenomenon in magnetic nanowires. The basic idea is to extend the well established phenomenological Landau-Lifshitz (LL) or Landau-Lifshitz-Gilbert (LLG) equations by incorporating additional terms that include the spin transfer torque. The LL or LLG equations have been used to successfully account for the field driven dynamics of domain walls. Details of these models are briefly introduced in Chapter 2.2. Although all theories agree on the basic phenomenology of the spin transfer torque, one problem that has not yet reached any consensus is the manner by which damping is applied to this spin-torque term. Depending on how damping is included in the LL or LLG equations, there can be an additional spin transfer torque term, often termed the non-adiabatic spin transfer torque term. This term strongly modifies the basic properties of current induced DW motion and thus, its very existence, and, if it exists, its size and sign, are of considerable interest. One of the objectives of the work is to study the size of the non-adiabatic spin transfer torque term.

In addition to the current induced motion of DWs, the DW structure itself may be distorted by the current via spin-transfer torque, as reported in Refs. [63, 64]. Large current densities may also result in the generation of domain walls (see Refs. [65, 66]).

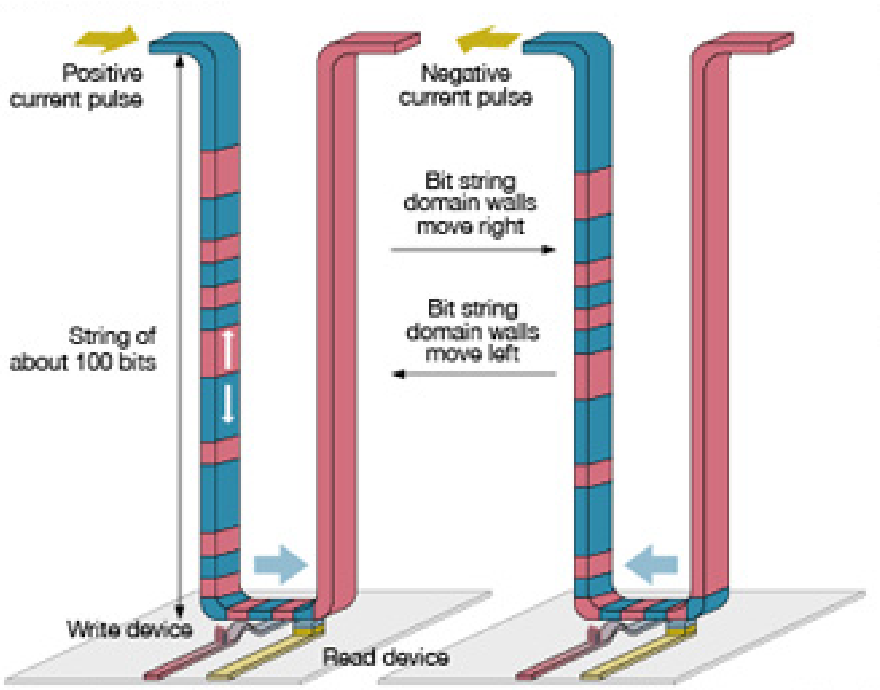

Figure 1.1: Schematic illustration of the magnetic racetrack memory.

1.2 Magnetic Racetrack Memory

A number of innovative proposals have been reported which use domain walls (DWs) in nanowires as information bits for memory[67] or logic devices [68, 69, 70, 71]. Some of these concepts have roots in bubble devices developed several decades ago. One of the objectives of this work is to demonstrate that DW based nanodevices are viable. In particular, the potential of a memory shift register based on DWs called the Magnetic Racetrack Memory[67] is highly attractive since it has the capability of not only replacing current silicon based memories but magnetic hard disk drives as well. The basic operation of this racetrack memory is described here.

Figure 1.1 shows a schematic image of the racetrack memory. Magnetic wires are created vertically above the surface of a substrate. Red and blue colors represent the direction of the magnetization along the nanowire, i.e. the racetrack. The boundary between the magnetic domains is the DW. Either the magnetic domain or the DW acts as the data bit. The data is read out from a read device, possibly a magnetic tunnel junction, which is located near the substrate. A writing element, possibly a magnetic nanowire containing a DW, may also be located in or near the substrate. In order to write bits into the racetrack, a DW is passed through this lateral magnetic nanowire (using current pulses). The DW is associated with a large localized magnetic stray field. This stray field can be used to set the magnetization direction of the targeted bit in the racetrack.

In order to either read or write one bit, the targeted bit has to be moved to the reading or writing device, respectively. To do so, all the data bits, i.e. all the DWs, have to be moved together under the influence of a single current pulse, so that the targeted bit reaches the reading or writing element without disturbing the other stored bits. This requires that all the DWs need to move in a synchronized fashion with a single current pulse excitation. DWs are moved around the racetrack, in a correlated fashion, with a sequence of current pulses through the spin transfer torque effect. This is the prime motivation for the work described in this thesis.

1.2.1 Objective of this work

There are several important aspects that need to be addressed to make a viable racetrack memory. The first, and perhaps the most critical issue, is to reduce the critical current density to move the DWs along the magnetic nanowire. Currently, the reported critical current densities are so high [36, 72, 38, 40] such that significant Joule heating occurs during the current pulse application. Lower critical current densities are also required for lower power consumption. A second important problem is to understand the relationship between the DW velocity and the magnitude of the current density. Not only are the number of reports on current driven DW velocities limited, but the reported DW velocities are orders of magnitude lower [36, 38] than those predicted theoretically. High DW velocities are required for fast operation speed of the racetrack memory. Addressing these questions are the main objectives of this work.

1.3 This thesis

The following chapter describes the basic model of domain wall dynamics based on the Landau-Lifshitz-Gilbert equation. The chapter starts from an introductory description of the spin transfer torque acting on domain walls. Then the one dimensional model of DW dynamics, extended to include the spin transfer torque term, is derived.

Chapter 3 describes the experimental setup and methods used in this work. Since the anisotropic magnetoresistance (AMR) effect is used to characterize the DWs in the nanowires, a brief description of the AMR effect is first given. Followed by the descriptions of the samples and the experimental setup, methods of injecting domain walls into permalloy nanowires[73] are introduced. In particular, the local field generation method, used throughout this work, will be described in detail. Finally, definitions of the structures of the DWs that appear in this work are listed.

Since large current densities need to be passed through permalloy nanowires to observe current DW induced motion, Chapter 4 describes the consequence of Joule heating in such nanowires. Time resolved resistance measurements are used to characterize the temperature increase in permalloy nanowires due to Joule heating as a function of the nanowire thickness and width.

Chapter 5 describes the field and current induced depinning of domain walls from artificially created pinning centers in permalloy nanowires[74]. Details of the characterization method to measure injection, propagation, pinning and depinning of domain walls using resistance measurements, are introduced in this chapter. The threshold current needed to depin a DW from its pinning center is studied as a function of the domain wall structure and its chirality, the pinning strength of the pinning center, the current pulse length as well as the applied magnetic field. An oscillatory dependence of depinning[75] and transformation probability on the current pulse length are reported. All of the experimental results are compared to the one dimensional model of DW dynamics including spin transfer torque.

Chapter 6 describes measurements of domain wall velocity in permalloy nanowires. Time resolved anisotropic magnetoresistance measurements are used to estimate the field and/or current driven domain wall velocity[76]. Current driven domain wall velocities exceeding the rate of spin angular momentum transfer are reported[77].

Chapter 7 describes the dynamics of domain walls propagating along permalloy nanowires. It is shown that the field-driven motion of domain walls is associated with a periodic change in their chirality, due to the coherent precession of the propagating domain wall. The frequency and phase of this domain wall precession can be tuned by using a combination of magnetic field and current[78].

A brief summary of this work concludes this thesis.

Chapter 2

1D model

2.1 Landau-Lifshitz and Gilbert equation

The starting point of the 1D model is to use the phenomenological Landau-Lifshitz (LL) or Gilbert (LLG)[79] equation. The LL equation reads

$$\frac{\partial \overrightarrow{m}}{\partial t} = -\gamma_{LL} \overrightarrow{m} \times \overrightarrow{H}_{eff} + \alpha_{LL} \overrightarrow{m} \times (\overrightarrow{m} \times \overrightarrow{H}_{eff}) \tag{2.1}$$

and the Gilbert equation reads

$$\frac{\partial \overrightarrow{m}}{\partial t} = -\gamma \overrightarrow{m} \times \overrightarrow{H}_{eff} + \alpha \overrightarrow{m} \times \frac{\partial \overrightarrow{m}}{\partial t} \tag{2.2}$$

where $\overrightarrow{m}$ is the unit vector representing the direction of the local magnetic moments, $\overrightarrow{H}_{eff}$ is the effective field, γ is the gyromagnetic ratio and α is the Gilbert damping constant[80]. The form of the effective field will be discussed in Section 2.3. In the LL equation, α_{LL} and γ_{LL} are the effective damping and the effective gyromagnetic ratio, respectively. Although the forms are different, the Eqs. (2.1) and (2.2) are equivalent[1] when $\alpha_{LL} = \frac{\alpha\gamma}{1+\alpha^2}$ and $\gamma_{LL} = \frac{\gamma}{1+\alpha^2}$ are assumed; the calculated responses of $\overrightarrow{m}$ under any magnetic field excitations are the same.

2.2 Spin transfer torque terms

The microscopic origins of the spin transfer torque are still under debate. Current consensus is that there are at least two mechanisms that can cause DW motion by current. The first one is to transfer angular momentum from the conduction electrons to the localized magnetic moments, i.e. a concept similar to what was originally proposed by Slonczewski[32] in magnetic multilayer systems. In this case, it is assumed that when the electrons move across the DW, they adjust their spin orientation adiabatically to the direction of the local moments while transferring angular momentum to the DW. The form of this adiabatic spin transfer torque is given[52] as

$$\overrightarrow{T}_{\alpha} = -u(\overrightarrow{j} \cdot \nabla)\overrightarrow{m} \tag{2.3}$$

where $\overrightarrow{j}$ is the unit vector representing the direction of the current flow and u is the magnitude of this spin transfer torque. Note that u is in units of velocity.

The second mechanism, which is under debate, originates from the spatial mistracking of the conduction electron spins and the local moments. When the conduction electron spin orientation does not follow the the spin direction of the local moments, the electrons can be reflected from the local moments so changing its direction of motion. This in turn can transfer linear momentum from the conduction electrons to the local moments, which can also result in DW motion. This mechanism is generally called the non-adiabatic spin transfer process, where the non-adiabaticity represents the mistracking of the conduction electron spins and the local moments. The form of this non-adiabatic spin transfer torque is given[52] as

$$\overrightarrow{T}_{\beta} = \beta u\overrightarrow{m} \times (\overrightarrow{j} \cdot \nabla)\overrightarrow{m} \tag{2.4}$$

where β represents the relative contribution of the non-adiabatic spin torque term to the adiabatic spin torque term.

When the conduction electrons are reflected from the local moments due to the mistracking, additional resistance arises [81, 82, 83]. This additional resistance, known as the DW resistance, is also investigated in many systems [84, 85, 86, 87, 88, 89, 90, 91, 92, 93]. Note that the DW resistance is typically orders of magnitude smaller than the AMR effect in permalloy[87].

These two terms can be incorporated into either the LL or the Gilbert equation to examine the response of the magnetization to the current excitations. However, when the spin transfer torque terms are added, the two equations are no longer equivalent to each other. In particular, the addition of the adiabatic spin transfer torque term to the LL equation is equivalent to the addition of both the adiabatic and non-adiabatic spin transfer torque terms to the Gilbert equation with β set equal to α. Microscopically, whether the LL [55, 59] or the Gilbert [50, 51, 56, 52, 53, 54, 57, 61, 62] equation should be used as the basic equation is still under investigation. See Ref. [94] for a review of this discussions. Here we use the Gilbert equation as the basic equation to study the two spin transfer torque terms.

2.3 Model description

The Gilbert (LLG) equation including the adiabatic and non-adiabatic spin torque terms reads

$$\frac{\partial \overrightarrow{m}}{\partial t} = -\gamma \overrightarrow{m} \times \overrightarrow{H}_{eff} + \alpha \overrightarrow{m} \times \frac{\partial \overrightarrow{m}}{\partial t} - u(\overrightarrow{j} \cdot \nabla)\overrightarrow{m} + \beta u \overrightarrow{m} \times (\overrightarrow{j} \cdot \nabla)\overrightarrow{m} \tag{2.5}$$

where $\overrightarrow{m}$ and $\overrightarrow{j}$ are the unit vectors representing the direction of the local magnetic moments and the current flow, respectively. The effective field is defined as $\overrightarrow{H}_{eff} = \frac{1}{M_S}\frac{\delta w}{\delta \overrightarrow{m}}$, where w is the total energy density of the system and M_S is the saturation magnetization. Note that $\frac{\delta w}{\delta \overrightarrow{m}}$ is a functional derivative of w with respect to $\overrightarrow{m}$. The parameter u represents the magnitude of the spin transfer torque and is proportional to the charge current density J and the spin polarization P of the current, i.e. $u = \frac{\mu_B J P}{e M_S}$, where μ_B is the Bohr magnetron, e the electron charge and M_S is the saturation magnetization.

We now follow the procedure of [3] to deduce the equation of motion for a domain wall in a one dimensional (1D) system. When the spherical coordinate systems are employed, the direction of each magnetic moment can be expressed as

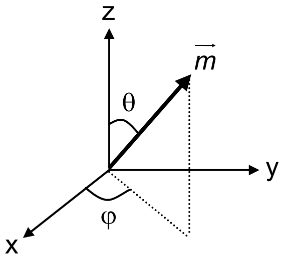

Figure 2.1: Definition of the coordinate system used in the 1D model of the DW.

$\vec{m} = \vec{m}(x,y,z) = (1, \theta(x,y,z), \varphi(x,y,z))$, where the dependence on the position of the moments is explicitly given. Note that since $\vec{m}$ is a unit vector, its amplitude is defined as 1. Definitions of the coordinate system are shown in Fig. 2.1. In a one dimensional system, it is assumed that $\vec{m}$ is a function of one spatial coordinate, i.e. $\vec{m} = \vec{m}(y) = (1, \theta(y), \varphi(y))$, where the y-axis is chosen to be the unique axis here. In other words, $\vec{m}$ is constant in the x and z direction. The LLG equation in the spherical coordinates then can be simplified and reads,

$$\dot{\theta} = -\frac{\gamma}{M_S}\frac{\delta w}{\delta \varphi} - \alpha \sin\theta \dot{\varphi} - u\frac{\partial \theta}{\partial y} - \beta u \sin\theta \frac{\partial \varphi}{\partial y} \tag{2.6}$$

$$\sin\theta \dot{\varphi} = \frac{\gamma}{M_S}\frac{\delta w}{\delta \theta} + \alpha \dot{\theta} - u \sin\theta \frac{\partial \varphi}{\partial y} + \beta u \frac{\partial \theta}{\partial y}. \tag{2.7}$$

This is a general form of the LLG equation, including the spin transfer torque terms, in a one dimensional system. Note that in Eq. (2.6) and (2.7) the current flow direction is defined to be in the y-direction and it is assumed to be homogenous. In order to further simplify the model, the azimuthal angle φ of the moments is assumed to be independent of position. The time dependence of both variables are derived, so that $\theta = \theta(y,t)$ and $\varphi = \varphi(t)$. Thus the spatial derivatives of φ in Eq.(2.6)and (2.7) vanish. The LLG equations (2.6)and (2.7) can be rearranged to show the functional dependence of the energy density w on the moment direction,

$$\frac{\delta w}{\delta \theta} = \frac{M_S}{\gamma}(\dot{\varphi}\sin\theta - \alpha\dot{\theta} - \beta u \frac{\partial \theta}{\partial y}) \tag{2.8}$$

$$\frac{\delta w}{\delta \varphi} = -\frac{M_S \sin\theta}{\gamma}(\dot{\theta} + \alpha\dot{\theta}\sin\theta + u\frac{\partial\theta}{\partial y}). \tag{2.9}$$

The functional derivatives of w with respect to the moments' direction in Eqs. (2.8) and (2.9) must be known to solve the partial differential equations. In order to calculate the functional derivative, first the variables are changed, which explicitly show that the changes in the moments's direction occur where the DW is located. The magnetization profile is thus assumed to be

$$\theta(y,t) = 2\arctan(\exp[\frac{y - q(t)}{\Delta}]) \tag{2.10}$$

$$\varphi(t) = \psi(t). \tag{2.11}$$

See Fig. 2.2 for illustration of the function $\theta(y,t)$. The newly introduced parameters are the central position of the DW $q(t)$ and the averaged tilt angle of the DW, $\psi(t)$. This particular profile is used because of its mathematical convenience, as it will become clear below. By carrying out this variable conversion, the spacial dependence of the variables is now removed. Note that the spacial independence of the azimuthal angle φ is now explicitly shown by using a different variable $\psi(t)$.

In order to remove the functional derivative, the areal energy density $\sigma = \int w dy$ is used instead of the volume energy density w. The change in the areal energy density can be expressed using the functional derivatives,

$$d\sigma = \int \delta w dy = \int \left((\frac{\delta w}{\delta\theta})\delta\theta + (\frac{\delta w}{\delta\varphi})\delta\varphi \right) dy. \tag{2.12}$$

The integration limit is from -∞ to ∞. Equations (2.8) and (2.8) can be substituted into Eq.(2.12) to calculate this integral. In doing this, several useful expressions, derived from Eq. (2.10), can be used to perform the integration more easily. The spacial and time derivatives of θ gives $\frac{\partial\theta}{\partial y} = \frac{\sin\theta}{\Delta}$ and $\dot{\theta} = -\dot{q}\frac{\sin\theta}{\Delta}$, respectively. In addition, $\delta\theta = -(\frac{\partial\theta}{\partial y})dq = -\frac{\sin\theta}{\Delta}dq$ and $\delta\varphi = d\psi$. Substituting these expressions into the integral (2.12) gives

$$d\sigma = -\frac{2M_S}{\gamma}(\frac{\alpha\dot{q}}{\Delta} + \dot{\psi} - \frac{\beta u}{\Delta})dq + \frac{2M_S}{\gamma}(\dot{q} - \alpha\dot{\psi}\Delta - u)d\psi. \tag{2.13}$$

Thus the functional derivatives of the energy density w can now be converted to partial derivatives of the areal energy density σ,

$$\frac{\partial\sigma}{\partial q} = -\frac{2M_S}{\gamma}(\frac{\alpha\dot{q}}{\Delta} + \dot{\psi} - \frac{\beta u}{\Delta}) \tag{2.14}$$

$$\frac{\partial\sigma}{\partial\psi} = \frac{2M_S}{\gamma}(\dot{q} - \alpha\dot{\psi}\Delta - u). \tag{2.15}$$

Rearranging Eq. (2.14) and (2.15 leads to the equation of motion of a DW in the one dimensional system.

$$(1+\alpha^2)\dot{q} = -\frac{\gamma}{2M_S}[\alpha\Delta(\frac{\partial\sigma}{\partial q}) - \alpha(\frac{\partial\sigma}{\partial\psi})] + (1+\alpha\beta)u \tag{2.16}$$

$$(1+\alpha^2)\dot{\psi} = -\frac{\gamma}{2M_S}[(\frac{\partial\sigma}{\partial q}) + \frac{\alpha}{\Delta}(\frac{\partial\sigma}{\partial\psi})] + \frac{\beta-\alpha}{\Delta}u \tag{2.17}$$

The remaining task is to compute the energy density σ of the system. In general, the energy of the system is expressed in terms of the volume energy density w using θ and φ to express the moments' direction. It is easy to calculate w in a homogenous system, however, the task gets very complicated when the variables θ and φ exhibit a nonlinear dependence on the spacial coordinates. To overcome this problem, we again integrate the volume energy density to obtain the areal energy density, which removes the spacial coordinate dependent variables. The volume energy density w mainly consists of exchange, anisotropy, demagnetization and zeeman energy terms. We define the y-axis as the easy axis. Each energy density can be expressed as

$$w_{EX} = A(\nabla\overrightarrow{M})^2 \tag{2.18}$$

$$w_{ANI} = K\sin^2\theta \tag{2.19}$$

$$w_{DEMAG} = \frac{1}{2}\overrightarrow{H_d}\cdot\overrightarrow{M} \tag{2.20}$$

$$w_{ZEEMAN} = -\overrightarrow{M}\cdot\overrightarrow{H_{EXT}} \tag{2.21}$$

Here A is the exchange constant, K is the uniaxial anisotropy energy, H_d is the

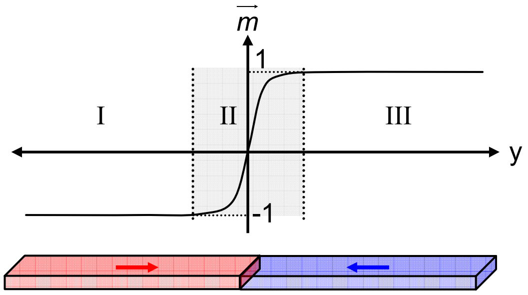

Figure 2.2: Illustration of the magnetization profile and the definition of the three regions, I, II, II used in the 1D model

demagnetization field and H_{EXT} is the applied external field. To proceed, we divide the system into three regions by introducing fictitious boundaries as shown in Fig. 2.2. The three regions consist of two outer regions (I, III) where the magnetization is homogeneous and a middle region (II) where the magnetization changes from -1 to 1, i.e. the region where the DW sits.We first compute the energy density in region II w_{DW}. Using the approximations, $\theta = \theta(y,t)$ and $\varphi = \varphi(t)$, w_{DW} reads

$$w_{DW} = A(\frac{\partial\theta}{\partial y})^2 + K\cos^2\theta + \frac{1}{2}M_S^2 N_z \sin^2\theta \sin^2\varphi + w_{Zeeman}^{DW}. \tag{2.22}$$

The Zeeman energy can be divided into two terms, i.e. contributions from the longitudinal magnetic field $-\overrightarrow{M} \cdot \overrightarrow{H}_A$ and from the transverse magnetic field, $-\overrightarrow{M} \cdot \overrightarrow{H}_T$. The total Zeeman energy is expressed as $w_{Zeeman}^{DW} = -M_S H_A \cos\theta - M_S H_T^z \sin\theta \sin\varphi - M_S H_T^x \sin\theta \cos\varphi$.

Integrating w_{DW} from $q - \frac{\Delta}{2}$ to $q + \frac{\Delta}{2}$ over y gives

$$\sigma_{DW} = \frac{2A}{\Delta} + 2K\Delta + M_S^2 N_z \Delta \sin^2\psi - \pi M_S \Delta (H_T^z \sin\psi + H_T^x \cos\psi). \tag{2.23}$$

Note that the Zeeman energy contribution from the longitudinal component disappears.

The energy density outside the DW (region I and III) w_{out} only contains the Zeeman energy, since it is assumed to be a perfect single domain in which the moments point along the easy axis. The integration runs from -∞ to $q - \frac{\Delta}{2}$ and from $q + \frac{\Delta}{2}$ to ∞. Doing the integral exactly gives

$$\sigma_{out} = -2qM_S H_A \tag{2.24}$$

The total energy per unit area is thus

$$\sigma_{tot} = \frac{2A}{\Delta} + 2K\Delta + M_S^2 N_z \Delta \sin^2\psi - \pi M_S \Delta (H_T^z \sin\psi + H_T^x \cos\psi) - 2qM_S H_A \tag{2.25}$$

In order to describe local pinning effects, a phenomenological pinning energy can be added to Eq. (2.25). The following form of the pinning energy will be added to σ_{tot}.

$$\sigma_{pin} = \frac{Vq^2}{d}\vartheta(|q| - d) \tag{2.26}$$

where V and d are the depth and width of the pinning potential and $\vartheta(q)$ is a bidirectional heaviside function.

We now have all the ingredients to construct the equation of motion for a DW in a quasi-one dimensional wire. Taking the partial derivative of σ_{tot} with respect to q and ψ and substituting them into Eq.(2.16) and (2.17) gives

$$(1+\alpha^2)\dot{q} = \frac{1}{2}\gamma\Delta(H_K \sin 2\psi - \pi H_T) + \alpha\gamma\Delta(H_A - \frac{Vq}{M_S d}) + (1+\alpha\beta)u \tag{2.27}$$

$$(1+\alpha^2)\dot{\psi} = -\frac{1}{2}\alpha\gamma(H_K \sin 2\psi - \pi H_T) + \gamma(H_A - \frac{Vq}{M_S d}) - \frac{\beta - \alpha}{\Delta}u \tag{2.28}$$

where H_K=$M_S N_z$, $H_T = H_T^z \sin\psi + H_T^x \cos\psi$ and V is redefined to include the heaviside function, $V = V\vartheta(|q| - d)$. This is the final form of the equation of motion for a DW in a one dimensional system. In order to simplify the equation, non-dimensional parameters are introduced. We first define the following parameters. $\omega_K \equiv \frac{1}{2}\gamma H_K$, $\omega_{pin} \equiv \gamma\frac{V\Delta}{M_S d}$, $\omega_A \equiv \gamma H_A$, $\omega_T^{z(x)} \equiv \frac{1}{2}\pi\gamma H_T^{z(x)}$, $p \equiv \frac{\omega_{pin}}{\omega_K}$, $a \equiv \frac{\omega_A}{\omega_K}$, $a^{z(x)} \equiv \frac{\omega_T^{z(x)}}{\omega_K}$ and $v \equiv \frac{u}{\Delta\omega_K}$. The space and time coordinates are also normalized, $x \equiv \frac{q}{\Delta}$, $x_d \equiv \frac{d}{\Delta}$ and

$\tau \equiv \frac{t}{\omega_K}$. The equations of motion Eq.(2.27) and (2.28) are rewritten as

$$(1+\alpha^2)\dot{x} = \alpha(a - px + \beta v) + (\sin 2\psi + a_x \cos 2\psi + a_z \sin 2\psi + v) \qquad (2.29)$$

$$(1+\alpha^2)\dot{\psi} = (a - px + \beta v) + \alpha(\sin 2\psi + a_x \cos 2\psi + a_z \sin 2\psi + v) \qquad (2.30)$$

2.4 Parameters in 1D model

For reference, a list of definitions of the parameters used with their descriptions are shown.

Constants
γ: gyromagnetic ratio (1.76×10^7 Oe^{-1}s^{-1})
μ_B: Bohr magnetron (0.927×10^{-20} erg/Oe)
e: electric charge (1.6×10^{-19} C)

Material parameters
H_K: anisotropy field, see Fig. 2.4 (a)
Δ: DW width, see Fig. 2.4 (b)
M_S: saturation magnetization
α: Gilbert damping constant
ω_K: frequency corresponding to H_K, $\omega_K = \frac{1}{2}\gamma H_K$

Parameters characterizing the pinning potential
V: depth of the parabolic pinning potential
d: width of the parabolic pinning potential
ω_{pin}: frequency corresponding to pinning, $\omega_{pin} = \frac{\gamma V \Delta}{M_S d}$
p: normalized pinning strength, $p = \frac{\omega_{pin}}{\omega_K} = \frac{V\Delta}{2M_S d H_K}$
x_d: normalized width of the pinning potential, $x_d = \frac{d}{\Delta}$

Parameters characterizing magnetic field
H_A: applied magnetic field along the nanowire

ω_A: frequency corresponding to applied field, $\omega_A = \gamma H_A$
a: normalized applied field, $a = \frac{\omega_A}{\omega_K} = \frac{H_A}{2H_K}$
H_T: applied transverse field
ω_T: frequency corresponding to transverse field, $\omega_T = \frac{1}{2}\pi\gamma H_T$
$a^{z(x)}$: normalized transverse field, $a^{z(x)} = \frac{\omega_T}{\omega_K} = \frac{\pi H_T}{H_K}$

Parameters characterizing current and spin transfer torque
J: current density
P: spin polarization of the current
u: spin transfer torque term, $u = \frac{\mu_B JP}{eM_S}$
β: non-adiabatic spin transfer torque term
v: normalized spin torque term, $v = \frac{u}{\Delta\omega_K}$

Parameters characterizing the DW
q: position of the DW
x: normalized position of the DW, $x = \frac{q}{\Delta}$
ψ: tilt angle of the DW
τ: normalized lab time, $\tau = \frac{t}{\omega_K}$

Finally, a method using micromagnetic simulations to deduce H_K and Δ of a DW in a magnetic nanowire is introduced. First, the magnetic field dependence of the DW velocity, in the absence of current, is calculated. A typical DW velocity versus magnetic field curve is shown in Fig. 2.3. Two parameters are extracted from this curve. The low field slope of the curve is defined as the mobility μ of the DW. The field at which the velocity peaks is called the Walker breakdown field H_{WB}. See Fig. 6.7, 6.10 and 6.11 for experimentally measured field dependences of the DW velocity. From the Walker breakdown field and the mobility, the anisotropy field H_K and the DW width Δ are obtained as

$$H_K = \frac{2H_{WB}}{\alpha} \tag{2.31}$$

$$\Delta = \frac{\mu\alpha}{\gamma}. \tag{2.32}$$

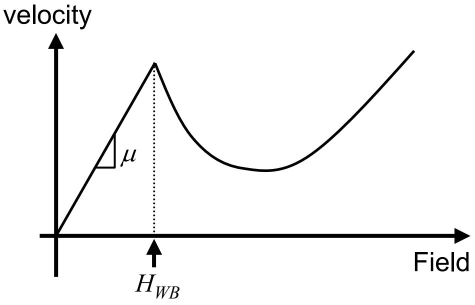

Figure 2.3: Schematic illustration of typical DW velocity versus magnetic field curve. The low field slope of the curve is defined as the mobility μ of the DW. The field at which the velocity peaks is called the Walker breakdown field H_{WB}.

The derivation of Eq. (2.31) is shown in Chapter 6 (see Eq. (6.17)). The definition of Δ was first introduced by Thiele[95] and was later extended by Nakatani et.al.[96]. Note that Δ does not represent the physical size of the DW. See Ref. [97] and Ref. [98] for the actual DW width in permalloy nanowires. Thus Δ is termed the dynamical DW width to differentiate it from the actual DW width.

Calculated H_K and Δ are shown in Fig. 2.4 (a) and (b), respectively, for vortex and transverse walls in 10 nm thick permalloy nanowire (see the third panels of Fig. 5.4 (a,c) for the magnetic configuration of transverse walls and (b,d) for that of vortex walls). The dynamic DW width Δ increases with the wire width for both DW structures. However, note that the magnitudes are an order of magnitude smaller that the actual wall width (typically of the order of the wire width). By contrast, the dependence of the anisotropy field H_K on the wire width is different for the two DW structures. H_K increases when the wire width is increased for the vortex walls, whereas it decreases for the transverse walls. H_K is significantly larger for the transverse wall as the wire width is decreased. Discussions of these differences in H_K for the two DW structures are reported in Ref. [75]. Note that the wire width dependence of H_K changes when the thickness is changed.

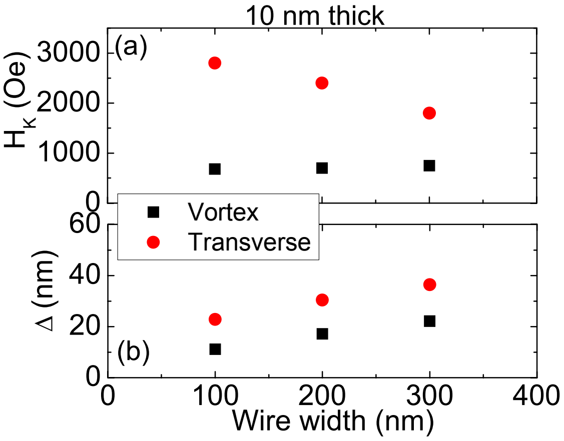

Figure 2.4: Calculate anisotropy field H_K and the dynamic DW width Δ plotted against the nanowire width in 10 nm thick permalloy nanowires. H_K and Δ are calculated for both vortex and transverse walls. Micromagnetic simulations and Eq. (2.31) and (2.32) are used to obtain these numbers.

Chapter 3

Experimental Description

3.1 Anisotropic magnetoresistance

The presence of magnetic domain walls (DW) in magnetic nanowires is detected through measurements of their resistance. The detection scheme relies on the anisotropic magnetoresistance (AMR) effect [99, 100, 101, 102, 103, 104]. The AMR effect is typically small (of the order of a few percent at room temperature) compared to the giant magnetoresistance effect (GMR, up to ∼20%)[105, 106, 107] or the tunneling magnetoresistance (TMR, 50-500%)[108, 109, 110, 111, 112] effects. However, using the AMR effect in single layer nanowires has several advantages over using the GMR or TMR phenomena in multilayered nanowires. From AMR, the presence of a DW can be directly measured through the resistance of the magnetic layer that carries the DW, since the AMR effect is a bulk scattering phenomenon. By contrast, the GMR and TMR effects require an additional reference magnetic layer in addition to the nanowire layer in order to detect a DW, since these phenomena are largely interface effects. Such a reference layer may well perturb the dynamics of the DW motion through, for example, dipolar coupling[113], or exchange coupling[114, 115]. Moreover, some of the driving current may well be shunted through the additional layers in the multilayer devices. The shunted current will likely generate Oersted fields which may futher perturb the DW's motion. One particular advantage of a GMR structure, however, is that the resistance of the nanowire varies almost linearly with the position of the DW along the nanowire so that the position of the DW can be directly determined. This is not the case with AMR which only detects the presence of a DW indepenent of its position along the nanowire.

There are several other possible methods of detecting a DW in a nanowire. One of these is the anomalous Hall effect which is a phenomenon exhibited by magnetic materials. However, depending on its implementation, it makes most sense to use a material whose magnetization easy axis points perpendicular to the nanowires' surface[43, 47]. For in-plane and out-of-plane magnetized systems, a well designed Hall bar may be used to detect the presence of a DW, but this requires a much more complex microfabricated device.

For these reasons, the AMR effect was chosen to detect the presence of DWs in permalloy nanowires. In order to obtain a reasonably large signal to noise ratio, materials with large AMR effects would be preferred. The AMR effect is typically large in Ni-based transition metal alloys[116, 117], with the largest AMR effects found in the NiCo and NiFe binary alloy systems. We chose to study $Ni_{81}Fe_{19}$, the NiFe composition with the largest AMR effect. $Ni_{81}Fe_{19}$ has an advantage over NiCo alloys since it exhibits nearly zero magnetostriction. Magnetostrictive materials may give rise to magnetic irregularities in nanowires, such as random localized pinning sites, through magneto-elastic effects since their magnetic properties are sensitive to local strains or stresses which may develop in the nanowire during etching.

The AMR effect in $Ni_{81}Fe_{19}$ (permalloy) is typically 1.5-2% (at room temperature). The dependence of the resistance of a permalloy film on the relative angle (φ) between the applied magnetic field and current direction is shown in Fig. 3.1 (b). Definitions of the directions of current flow (I), magnetization (M) and applied magnetic field (H) are shown in (a). The applied magnetic field is 500 Oe, large enough to saturate the magnetization. Thus the magnetic field direction coincides with the magnetization direction of the permalloy film. Here, zero degree indicates that the direction of the applied magnetic field and that of the current is parallel. As evident from Fig. 3.1, the device resistance reaches a minimum when the current flows perpendicular to the magnetization direction which is typical in Ni-based binary alloy systems. This is typical in Ni-based binary alloy systems. The device resistance scales with the angle

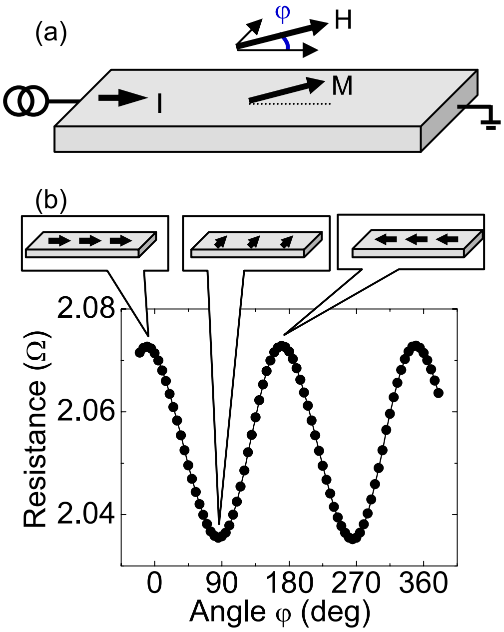

Figure 3.1: (a) Definitions of the directions of current flow (I), magnetization (M) and applied magnetic field (H). The angle φ stands for the relative angle between the field and the current. (b) Dependence of the resistance of a 10 nm thick permalloy film on the relative angle (φ) between the applied magnetic field and current direction. Illustrations of the magnetization configuration are shown at the top. Zero degree indicates that the direction of the applied magnetic field and that of the current is parallel. The applied magnetic field is 500 Oe, large enough to saturate the magnetization.

φ as

$$R = R_0 - \Delta R \cos^2 \varphi. \tag{3.1}$$

Thus, by measuring the device resistance, it is possible to infer the amount of magnetization that points perpendicular to the current flow direction. Details of the correlation between the resistance and the magnetic configuration are reported in Chapter 5.

3.2 Setup and sample description

3.2.1 Sample description

Permalloy nanowires are formed from films of 0.5 Fe/10 AlO_x/10 $Ni_{81}Fe_{19}$/0.5 TaN/5 Ru (units in nm), deposited by magnetron sputtering on highly resistive Si substrates (~800 Ωcm) on which a thin native Si oxide layer will have formed. The AlO_x layer is used to provide a very smooth and clean template layer on which the $Ni_{81}Fe_{19}$ layer is grown and is used to prevent silicide formation at the NiFe/Si interface. An ultra thin Fe layer is inserted to prevent silicide formation at the interface with the substrate. A thin Al layer is deposited on top of the Fe layer and a AlO_x is then formed by reactive dc magnetron sputtering of an Al target in an Ar-O_2 gas mixture. A 5 nm Ru layer is used for the capping layer because its oxide is conducting although the conductivity of the Ru oxide (RuO_2) is poor. A conducting oxide is preferred since most capping layers will oxidize and a low contact resistance with the subsequently deposited/patterned contact lines (5 nm Ta/45 nm Rh) is needed. Ru adversely affects the magnetic properties of permalloy so a 1 nm TaN is to used to separate the $Ni_{81}Fe_{19}$ and Ru layers. The TaN layer is also important because it is an oxidation barrier (even at elevated temperatures, which may be reached during subsequent processing) and therefore protects the $Ni_{81}Fe_{19}$ film from any oxidation.

Electron beam lithography and Ar ion etching are used to pattern 80-300 nm wide nanowires. Electrical contacts to the nanowire are formed by patterning 5 nm Ta/45 nm Rh film using electron beam lithography and Ar ion etching. The electrical contacts consist of large contact pads (150×100 μm) connected to the nanowire via a 500 nm wide line. A ground plane, also patterned from the same 5 nm Ta/45 nm Au film, surrounds the device. This ground plane acts as a noise shield and is also used when high frequency probes are used to contact the device.

Various nanowires were fabricated which can be categorized into two shapes, straight nanowires or nanowires with two straight arms connected to each other at right angles via a quarter circle whose radius is 3 μm (see Fig. 3.2). Both ends of these arms or the straight line are tapered to a sharp point to prevent nucleation of DWs from the ends of the nanowire and to assist annihilation of any DW that enters this region.

3.2.2 Experimental setup

All of the measurements are performed in a probe-station (Desert cryogenics, 6-axis tabletop, variable temperature down to 4.2 K) at room temperature. Small homemade electromagnets are introduced into the probe-station to generate magnetic fields up to ∼400 Oe. High frequency probes are used to make contact to the devices. The probes have bandwidth of either dc-5 GHz (Desert Cryogenics, Z50 probes) or dc-40 GHz (GGB Industries, customized probes designed for the probestation). Resistance of the device is measured by a two-point probe technique. A dc voltmeter (Keithley model 2002) and dc current source-meter (Keithley model 6430) are connected in parallel to the device to measure the resistance. In order to inject current pulses into the device, a constant voltage pulse generator (Picosecond Pulse Labs, model 10075A or 10300B) is used. Bias tees (Picosecond Pulse Labs, model 5547A, 5540B) and dc blocks (Inmet, model 8038) are used as required.

3.3 DW Injection

By fabricating magnetic nanostructures with widths and thicknesses comparable to magnetic domain wall widths, it is possible to inject and manipulate a *single* domain wall (DW) in such devices. In particular, in soft magnetic materials, where the domain configurations are predominantly determined by the shape of the device, manipulation of DWs can be carried out by applying suitable sequences of magnetic fields. In this chapter, various methods of injecting a DW into magnetic nanowires are introduced. In particular, the local field generation method, which is used throughout this work, will be discussed in detail in this section.

3.3.1 Injection using magnetic fields

Injecting a DW into a magnetic nanostructure or a nanowire is accomplished by reversing the magnetization direction locally in a portion of the structure. In soft magnetic materials, this can be achieved by using suitable structures and by applying an appropriate field sequence. Two examples of using a magnetic field sequence to inject a DW into a nanowire are discussed.

As a first example, Fig. 3.2 shows an scanning electron microscopy (SEM) image of a permalloy nanowire with two perpendicular arms connected via a curved region. The magnetization configuration of the nanowire is shown in the figure by blue and red arrows representing moment locally aligned along or against the direction of the nanowire. In Fig. 3.2 (a), the magnetization of the nanowire is aligned in the same direction all along the length of the nanowire. When a magnetic field is applied at an angle to each of the arms of the nanowire, as shown in Fig. 3.2 (b), the magnetization of the horizontal arm, in this case, becomes energetically unstable and eventually reverses its direction as shown in the figure. Note that the magnetic moment directions in the nanowire arms, at any given point in time, are determined by the relative strengths of the applied field and the demagnetizing field of the nanowire. Thus the moment direction will not lie exactly along the nanowire's length (as shown in the figure). Moreover, there will be a threshold field at which the magnetization of the horizontal arm switches its direction, whose strength will be determined by the saturation magnetization and crystalline anisotropy of the nanowire and the demagnetizing field of the nanowire (which is determined by the width and thickness of the nanowire). Consequently, when the magnetization direction switches in the horizontal arm, a 180 degree DW is formed in the curved portion of the nanowire (as indicated by a white bar in the figure). When the magnetic field is decreased to zero, due to the magnetic hysteresis of the nanowire, the DW remains in the nanowire. Thus, by using this field sequence, a DW is created or "injected" into the nanowire.

Another example is shown in Fig. 3.3, where a SEM image (far left) and a series of Photo Emission Electron Microscopy (PEEM) images of the permalloy element are shown. The permalloy element consists of a vertical arm with an elliptical injection pad attached to it. An artificial patterned defect (a notch) is fabricated in the middle of the permalloy arm. The contrast of the PEEM images reflects the magnetization direction. In these images, black and white contrast corresponds to local magnetic moments pointing up and down, respectively. Grey contrast represents magnetization

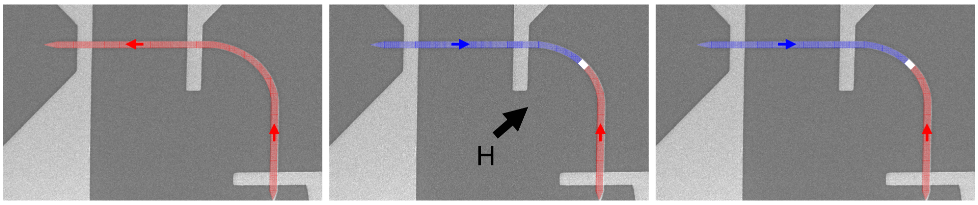

Figure 3.2: Illustration of a process where a DW is injected at the 90 degree corner of the nanowire using appropriate field application sequence. The colored arrows indicate the magnetization direction of the nanowire. The white line represent a HH DW.

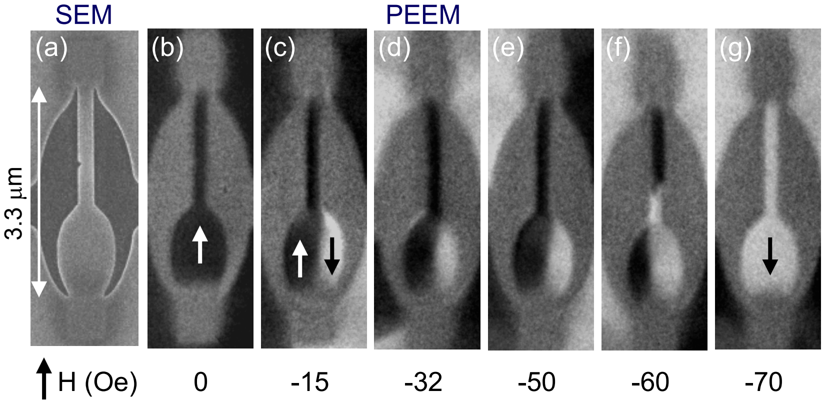

Figure 3.3: PEEM images of a permalloy nanowire after magnetic fields, listed at the bottom of each image, are applied. The images are taken at zero magnetic field. The black-white contrast reflects the magnetization component along the wire axis. The arrows indicate the direction of the magnetization.

pointing either horizontally (left or right) or zero net magnetization (averaged over the spatial resolution of the PEEM). The definition of positive applied field is indicated at the bottom left of the figure.

A DW is injected into the vertical arm by first, applying a large positive magnetic field to set the magnetization direction of the whole permalloy element in one direction. Then the direction of the field is reversed to the values shown at the bottom of the images. Subsequently, the field is reduced to zero and the PEEM images are taken. Fig. 3.3 (b) show the PEEM image where the element is homogeneously magnetized. When a small negative field is applied (c-e), the magnetization direction inside the pad changes; a vortex DW structure is created in the pad. Although it is difficult to see, a 90 degree DW is formed at the interface between the pad and the arm. A further increase in the field in the negative direction does not change the configuration until at -60 Oe the white contrast region extends into the arm. The white contrast region ends where the patterned defect is located. The transition between the white and black contrast regions, located in the arm, represents the DW. Again, by using a suitable field sequence, a DW is injected into the nanowire. A further increase in the magnetic field results in an extension of the white contrast region, in which the DW is erased and the permalloy element is fully magnetized.

3.3.2 Local field generation method

As stated before, DW injection is to reverse the magnetization direction locally. Instead of using geometrical irregularities of the magnetic material to inject a DW, one can simply apply a local magnetic field, large enough, to change the magnetization direction locally. From Maxwell's equation, magnetic fields are generated when a current passes through a conducting wire. The larger the current, the larger the magnetic field. By reducing the size of the conducting wire, it is possible to generate localized magnetic field around the wire. We use this concept to inject DWs into permalloy nanowires.

Figure 3.4 shows a scanning electron microscopy (SEM) image of the device with the experimental setup laid on top of it. The horizontal line is the permalloy nanowire.

The two vertical lines A and B are the contact lines to the nanowire made of 5 nm Ta/45 nm Rh. Note that these two lines are connected to each other via the permalloy nanowire. The width of the contact line is set to 500 nm and the resistance (from one end to the other) is ~80-85 Ω.

Current is passed through line A to generate localized magnetic field around the line. In order to generate maximum possible field, one needs to pass high amplitude current through the line. However, higher currents may result in Joule heating or electro-migration, which can significantly damage the sample. Thus to avoid these effects, we use current pulses to minimize the power delivered to the line. In addition, using current pulses to generate magnetic field provides a control of timing the magnetic field application, which is impossible to do when electro-magnets are used. In other words, one can control the timing of DW injection within the precision of less than a nanosecond.

A constant voltage pulse generator (Picosecond pulse labs, model 10300B (250 ps rise time) or model 10075A (75 ps rise time)) is connected to one end of line A. The input impedance of the pulse generator is nominally 50 Ω. The other end of line A is connected to a 50 Ω termination to avoid any multiple reflections of the injected pulse.

The voltage pulse injected from line A can be regarded as a current pulse as long as the resistance of the line does not change over the pulse application period. In Chapter 4, the Joule heating effects are investigated.

Using Biot-Savart's law, one can calculate the magnetic field generated by a current passing through a conducting wire, whose thickness and width is defined as t_L and w_L. The Y and Z component of the magnetic field at point (Y, Z) is expressed as[118]

$$B_X = \frac{\mu_0 J}{2\pi}\left[F(X+\frac{w_L}{2}, Z+t_L) - F(X+\frac{w_L}{2}, Z) + F(-X+\frac{w_L}{2}, Z+t_L) - F(-X+\frac{w_L}{2}, Z)\right] \tag{3.2}$$

$$B_Z = \frac{\mu_0 J}{2\pi}\left[G(X+\frac{w_L}{2}, Z+t_L) - G(X+\frac{w_L}{2}, Z) - G(-X+\frac{w_L}{2}, Z+t_L) + G(-X+\frac{w_L}{2}, Z)\right] \tag{3.3}$$

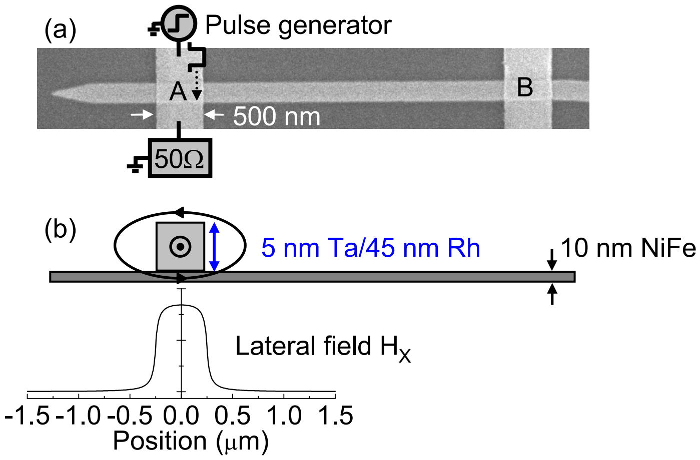

Figure 3.4: (a) Scanning electron microscopy image of a permalloy nanowire (horizontal) and its electrical contacts (vertical lines). A schematic illustration of the experimental setup is overlaid on the image. (b) Cross sectional image of the device shown in (a). The arrows show the direction of the local magnetic field generated when a current pulse is passed through line A. A schematic of the local magnetic field is shown at the bottom.

Note that B_X and B_Z are in units of Tesla. The coordinates X represents the horizontal distance from the center of the line, whereas Z represents the vertical distance from the bottom edge of the slab (see Fig. 3.5 for the definitions). Functions $F(x, z)$ and $G(x, z)$ are defined as

$$F(x,z) = z\arctan(\frac{x}{z}) + \frac{1}{2}x\log\{x^2+z^2\} \tag{3.4}$$

$$G(x,z) = -2z + 2x\arctan(\frac{z}{x}) + z\log(x^2+z^2) \tag{3.5}$$

Calculated magnetic fields using Eq. (3.2) and (3.3) are shown in Fig. 3.6 for fields (a) along the nanowire (H_X) and (b) perpendicular to the nanowire (H_Z). Both fields are plotted for three different positions at the Z-axis. The distance in the vertical direction is measured from the bottom edge of the line. The amplitude of the voltage pulse is set to 2 V, which corresponds to a current density of 0.96×10^8 A/cm^2 flowing through the line. It is clear that the magnetic field along the nanowire

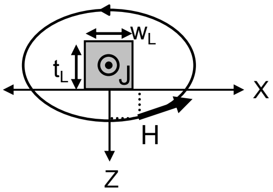

Figure 3.5: Coordinates of the system and definition of the directions of the local magnetic field generated around line A.

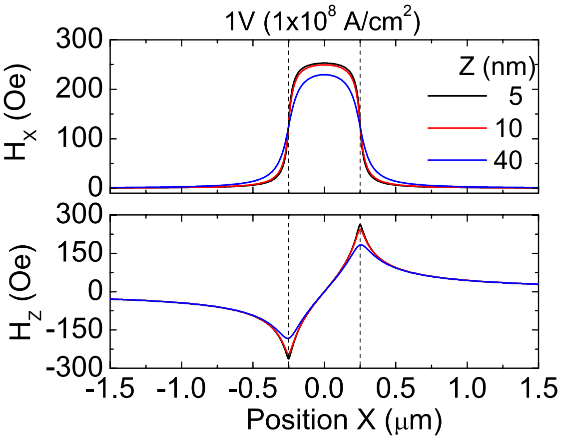

Figure 3.6: (a) X and (b) Z component of the calculated magnetic field plotted against the position along the nanowire. Fields are calculated at three different heights (along Z). The vertical dotted lines represent the edges of line A.

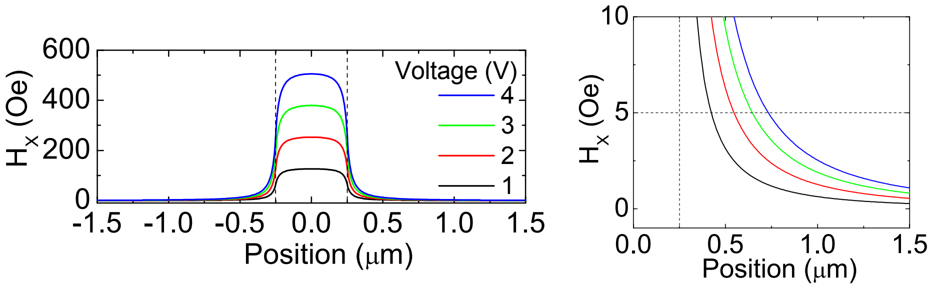

Figure 3.7: (a) X component of the calculated magnetic field plotted against the position along the nanowire. The amplitude of the input voltage pulse is varied. (b) Expanded image of (a), where the tail of the magnetic field near the edge of line A are shown. The vertical dotted lines represent the edges of line A.

(H_X) is confined to the width of the line. The perpendicular field takes its maximum value at each edge of the line. As the vertical distance from the line increases, the field profile near the line edges become more rounded.

The dependence of H_X on the amplitude of the injected pulse voltage is shown in Fig. 3.7 (a). The maximum field at the center of the line linearly increases with the voltage amplitude. To illustrate the confinement of the magnetic field, the vertical scale in Fig. 3.6 (a) is expanded and are replotted in Fig. 3.7 (b). Even at the maximum voltage amplitude, it takes only $\sim$500 nm from the edge of the line to reduce the magnetic field below 5 Oe.

A simple model is used to estimate the magnitude of the magnetic field needed to reverse the magnetization direction in magnetic nanowires. In order to locally reverse the magnetization direction, two different processes can be considered, i.e. domain wall nucleation and propagation, or magnetization rotation. The former can be a complicated process since it involves random nucleations. Here the latter model is employed, where the local moments are assumed to rotate coherently. Figure 3.8 (a-c) illustrates this process. As the localized field is generated, the magnetic moments under the line rotate from one direction (a) to the other (c) via a configuration where the magnetization points perpendicular to the wire's long axis (b). Since the nanowire is thin, it is assumed that the rotation occurs in plane.

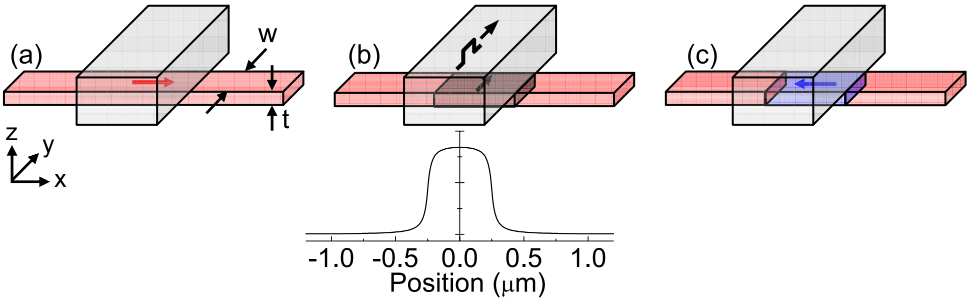

Figure 3.8: Schematic illustration of the local magnetization reversal process. The colors, red and blue, show the magnetization direction of the permalloy nanowire. The gray line on top of the permalloy nanowire is line A, through which the current pulse is passed. t and w correspond to the thickness and width of the permalloy nanowire. The definition of the coordinates x, y, z are shown together.

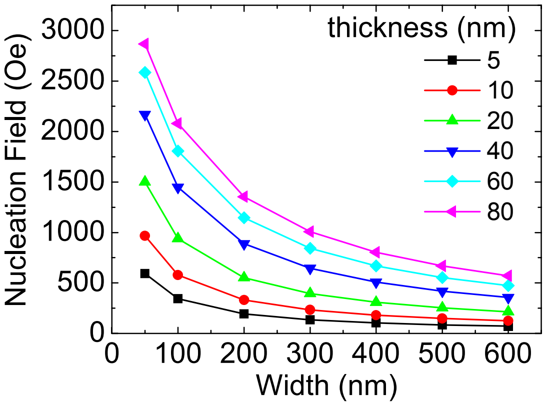

Figure 3.9: Calculated minimum fields required to the reverse the magnetization of a permalloy slab, plotted against the width and thickness of the slab. The length of the slab is set to 500 nm.

The Zeeman energy from the local magnetic field must overcome the energy needed to rotate the magnetization perpendicular to the wire's long direction. The energy difference ΔE between configuration (a) and (b) is

$$\Delta E = \frac{1}{2}\overrightarrow{M} \cdot \overrightarrow{H_d} V - \overrightarrow{M} \cdot \overrightarrow{H} V \tag{3.6}$$

where $\overrightarrow{M}$ is the magnetization, $\overrightarrow{H}$ is the applied local field, $\overrightarrow{H_d}$ is the demag field and V is the volume of the portion where the reversal occurs. When the rotation occurs in the nanowire's plane, the demag field can be expressed as

$$\overrightarrow{H_d} = N_y M \widehat{y} \tag{3.7}$$

where N_y and $\widehat{y}$ are the demag factor and a unit vector along the y-direction, respectively. The volume where the reversal occurs is defined as $V = tww_L$. Substituting these values into Eq. (3.6) and setting $\Delta E = 0$ gives the field (H_N) needed to reverse the magnetization locally,

$$H_N = \frac{1}{2} N_y M \tag{3.8}$$

The demagnetization factor N_y can be calculated for a rectangular slab[119]. The values of H_N for permalloy nanowires (M_S=800 Oe) are plotted in Fig. 3.9 as a function of the nanowire width for different permalloy thicknesses. As the aspect ratio of the nanowire cross section (t/w) decreases, H_N becomes larger. Realistically, ~1000 Oe is the limit of generating local magnetic fields using current pulses, so apparently this method does not work for certain nanowires. However, note that for larger nanowires, the DW nucleation and propagation process dominates the reversal process, thus H_N may be reduced than that shown in Fig. 3.9.

3.4 Types of DWs in permalloy nanowires

Finally, typical domain wall structures that exist in permalloy nanowires used in this work are shown in Fig. 3.10. From the permalloy film thickness (10 nm) used here, only Neel walls can exist[1]. In addition, due to the lateral confinement in patterned

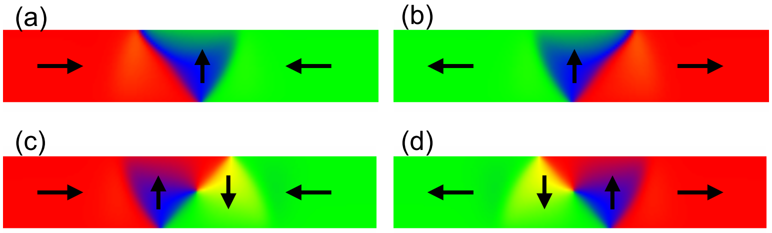

Figure 3.10: Images from micromagnetic simulations showing the transverse and vortex DW structures. The element size is 1700 nm×330 nm. (a) and (b) show transverse walls, whereas (c) and (d) show vortex walls. (a, c) show head to head DWs, whereas (b, d) show tail to tail DWs.

nanowires, the structure of DW can be generally divided into two types, transverse walls (a, b) and vortex walls (c, d). Other DW structures can be observed when the lateral dimension becomes larger (typically larger than ∼600 nm in 10 nm thick films). As shown in Fig. 3.10 (a, c), when the magnetization direction of the neighboring domains point to each other, the formed DW will be referred as a head to head (HH) DW . The opposite case (b, d) will be referred as a tail to tail (TT) DW . Although HH and TT DWs are essentially the same DW, their motion is different upon magnetic field application. For example, when a positive magnetic field (pointing towards right in Fig. 3.10, HH DWs will move to the right, whereas TT DWs move to the left. By contrast, note that when spin polarized currents are used to move the DW via spin transfer torque, both HH and TT DWs move in the same direction, i.e. along the electron flow direction.

Note that for the vortex walls, the chirality of the HH and TT DWs are opposite. The chirality of the vortex wall is defined as the rotation direction of the magnetization within the DW. For the images shown in Fig. 3.10, (c) is clockwise and (d) is anti-clockwise. The chirality of the transverse DWs can also be defined. Here the chirality of the transverse wall is defined as the rotation direction of the magnetization followed along the nanowire from the left domain to the right domain via the DW. Thus for the images shown in Fig. 3.10, both (a) and (b) are anti-clockwise transverse DWs.

A phase diagram of stable DW structures plotted against the nanowire width and

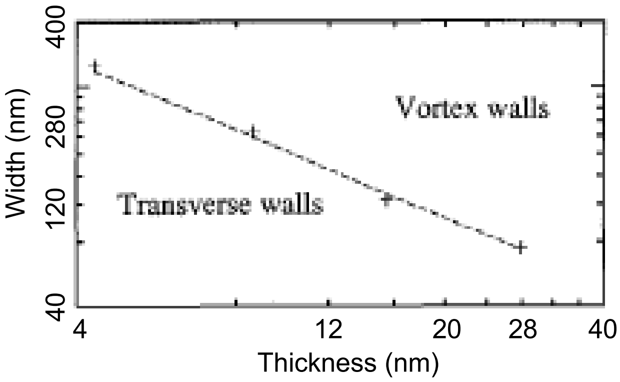

Figure 3.11: Calculated phase diagram, showing the stable DW structure in permalloy strips, from McMichael et.al.

film thickness were calculated by McMichael et.al.[97] using micromagnetic simulations and later on redefined by Nakatani et.al.[96]. Figure 3.11 shows the calculated phase diagram for permalloy nanowires from McMichael et.al.[97]. Neudecker et.al. used a magnetic imaging technique to experimentally obtain the phase diagram[120], however their observations were different from the above calculations. They pointed out that depending on how the DW is injected into the nanowire, the accessible DW structure changes. Thus the phase diagram they obtained do not represent the most stable DW structures, but rather the most accessible DW structures.

Chapter 4

Joule heating measurements

4.1 Introduction

Since current pulses are used to move domain walls (DW), Joule heating may occur at high current density. Various properties of magnetic material depend on temperature, thus it is important to know the temperature of the device to understand the essential contribution of the current pulses to the DW dynamics.

4.2 Experimental setup

The test device is 10-40 nm thick 4 μm long permalloy nanowires with its width varying from 80-300 nm. The nanowire is electrically connected to the contact pads, which are 100×150 μm large and made from 5 nm Ta/45 nm Rh, via a 500 nm wide contact line, also made from 5 nm Ta/45 nm Rh.

The experimental setup of measuring the Joule heating effect is shown in Fig. 4.1. A pulse generator (Picosecond Pulse Labs, model 10300B) is connected to contact line A. A sampling oscilloscope (HP54121A-54120B, 12 GHz bandwidth) is connected to line B. Broad bandwidth probes (GGB Industries, Picoprobe, dc-40 GHz) are used to make contact to the devices. A 100 ns long voltage pulse is generated from the pulse generator at a duty cycle of 1 kHz. The amplitude of the voltage pulse is varied from 0.1 V to 3.5 V. The sampling oscilloscope is triggered by the pulse generator's

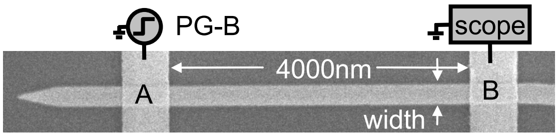

Figure 4.1: Scanning electron microscopy image of a permalloy nanowire (horizontal) and its electrical contacts (vertical lines). A schematic illustration of the time-resolved resistance measurement setup is overlaid on the image.

trigger output. The scope samples 500 points (0.24 ns spacing) for each trace and takes 128 traces for averaging to obtain an adequate signal to noise ratio.

4.3 Estimation of resistance increase

The voltage pulse transmitted through the device is first measured using the sampling oscilloscope. The measured voltage pulse V_T is then normalized to the amplitude of the injected voltage pulse V_{IN} to obtain the transmission coefficient $T \equiv V_T/V_{IN}$. Figure 4.2 (a) and (b) show the measured transmission coefficient for 10 nm and 40 nm thick permalloy nanowire, respectively. The width of the nanowire is 300 nm. The amplitudes of the input voltage are shown at the right side of each figure. Since the resistance of the device is higher for the 10 nm thick nanowire, the transmission coefficient is smaller compared to the 40 nm thick nanowires. For both thicknesses, the transmission coefficient decreases when the amplitude of the input voltage increases. This indicates that the device resistance increases when the amplitude is increased, likely due to Joule heating.

Using simple circuit theory, the transmission coefficient can be estimated as

$$T = \frac{V_T}{V_{IN}} = \frac{2}{Z_{DUT} + 2Z_0} \tag{4.1}$$

where Z_{DUT} is the device impedance and Z_0 (=50 Ω) is the characteristic impedance of the transmission line. Since the device impedance is dominated by the nanowire resistance, we ignore parasitic inductances and capacitances of the device and assume

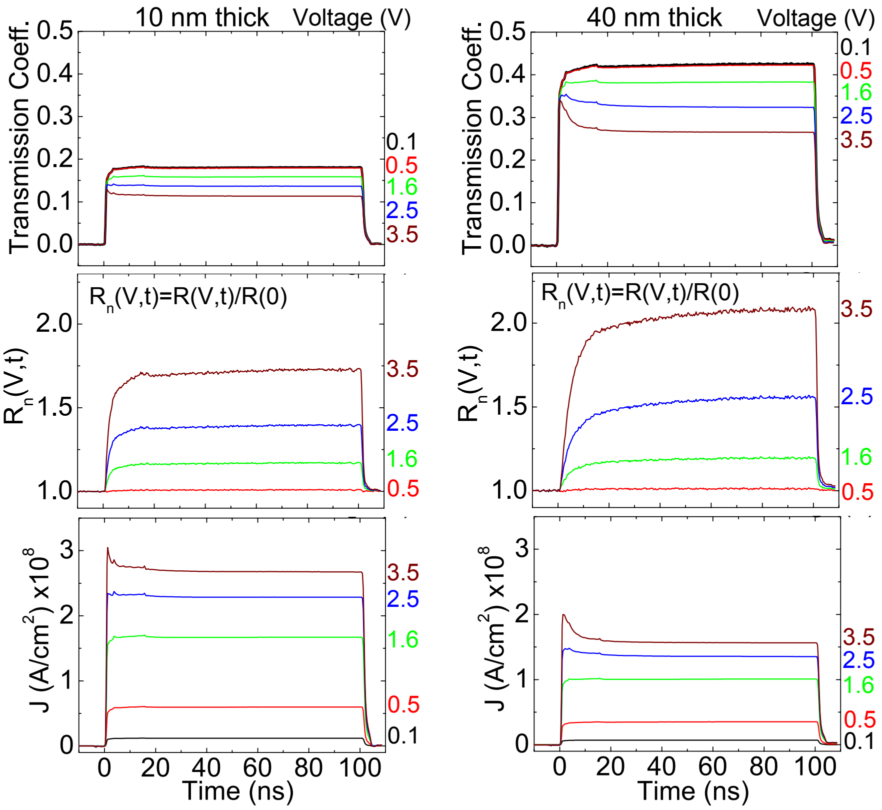

Figure 4.2: Transmission coefficients (a,b), estimated resistance (c,d) and calculated current density (e,f) of 10 nm (left panels) and 40 nm (right panels) thick 300 nm wide permalloy nanowires. The amplitudes of the input voltage pulse are shown on the right of each panel.

$Z_{DUT} \approx R_D + 2R_C \equiv R$, where R_D is the resistance of section A-B of the nanowire, R_C is the resistance of the contact line (from the pad to the intersection with the nanowire) and R is the total device resistance (see Fig. 6.1 (a) for the definitions of R_D and R_C, although they are not used in this chapter).

We first assume that Joule heating is negligible at the lowest pulse amplitude and take the transmission coefficient at this voltage as a reference, defined as $T(0)$. The difference between $T(0)$ and the transmission coefficient $T(V)$ when a voltage pulse with height V is injected is calculated, i.e. $\Delta T \equiv T(0) - T(V)$. The device resistance $R(V,t)$ when a voltage pulse of height V is injected into the nanowire can then be estimated from ΔV using the following relationship.

$$R(V,t) = \frac{\frac{2Z_0}{R(0)+2Z_0}R(0) + 2Z_0\Delta T}{\frac{2Z_0}{R(0)+2Z_0} - \Delta T} \tag{4.2}$$

where $R(0)$ is the device resistance without any Joule heating, i.e. the resistance at room temperature. It is convenient to work with a normalized resistance value since the conversion from resistance to temperature can be done directly. Thus the estimated device resistance are normalized to the room temperature resistance to define

$$R_n(V,t) \equiv R(V,t)/R(0). \tag{4.3}$$

Calculated values of $R_n(V,t)$ are shown in Fig. 4.1 (c) and (d) for 10 nm and 40 nm thick nanowires, respectively. Since the device resistance depends on the time, the time dependence are explicitly written in $R_n(V,t)$ and $R(V,t)$. Note that $R_n(V,t) = 1$ corresponds to no Joule heating. As the amplitude of the input voltage is increased, the device resistance nearly doubles in the 40 nm thick nanowire. Since the device resistance changes as a function of time, the current that flows into the nanowire is not constant. The current that flows into the device I_D can be calculated from $R(V,t)$ as

$$I_D(V,t) = \frac{2V_{IN}}{R(V,t) + 2Z_0} \tag{4.4}$$

The current density $J = I_D(V,t)/wt$ that flows in the nanowire is plotted in Fig. 4.1 (e) and (f) for 10 nm and 40 nm thick nanowires, respectively. The current density drops in the first tens of nanoseconds when the Joule heating becomes significant.

In order to obtain a expression that systematically describes the Joule heating, we separate the resistance increase to a time dependent term and a voltage dependent term. Two quantities $R_n(V)$ and $f(t)$ are defined as

$$R_n(V,t) \equiv f(t)R_n(V) \tag{4.5}$$

$$f(t) \equiv \frac{R_n(V,t) - 1}{R_n(V,t_{norm}) - 1} \tag{4.6}$$

$$R_n(V) \equiv R_n(V,t_{norm}) \tag{4.7}$$

where t_{norm} is an arbitrary pulse length. Here, $t_{norm} = 10$ ns is used. By definition, $R_n(V)$ is time independent. To show that the separation is valid, $f(t)$ must be independent of the pulse amplitude. Figure 4.3 (a) shows the calculated $f(t)$ at different amplitudes of the input voltage pulses. Clearly, the form of $f(t)$ does not depend on the pulse amplitude. It is useful to obtain an analytical formula for $f(t)$. From the form of Fig. 4.3 (a), we use the following expression,

$$f(t) = A\exp(-\frac{t}{\tau}) + at + b. \tag{4.8}$$

The fitted curve is shown in Fig. 4.3 (a) as a red dashed line. The agreement between Eq. 4.8 and the data is good. In Fig. 4.3 (b), $R_n(V)$ is plotted as a function of amplitude of the voltage pulse. The solid line is a fit to

$$R_n(V) = 1 + \alpha V^2 \tag{4.9}$$

where α is a fitting constant. The dependence of $R_n(V)$ on the amplitude of the voltage pulse is parabolic, consistent with Joule heating. Consequently, the normalized device resistance $R_n(V,t)$ can be estimated using Eq. (4.8) and (4.9) after a time t when a voltage pulse of height V is injected.

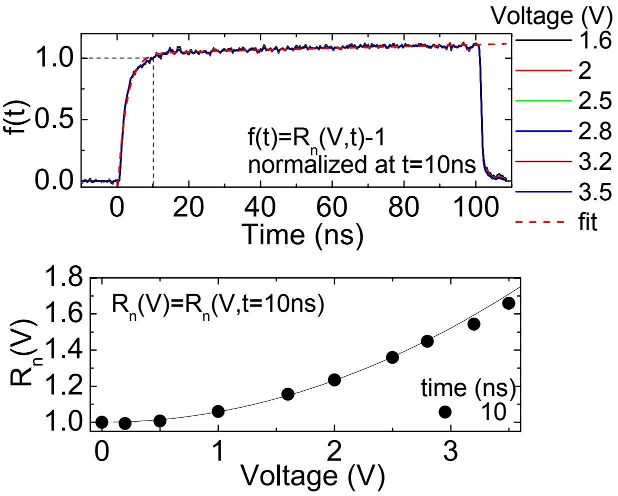

Figure 4.3: (a) Function f(t) of 10 nm thick 300 nm wide permalloy nanowire, calculated from the plots shown in Fig. 4.1 (c). The amplitudes of the input voltage pulse are shown on the right of each panel. The red dashed line is a fit to the data using Eq. (4.8). (b) Normalized resistance value (at 10 ns of the pulse) of 10 nm thick 300 nm wide permalloy nanowire plotted against the input voltage. The resistance values are taken from data shown in Fig. 4.1 (c). The solid line is a fit to the data using Eq. (4.9).

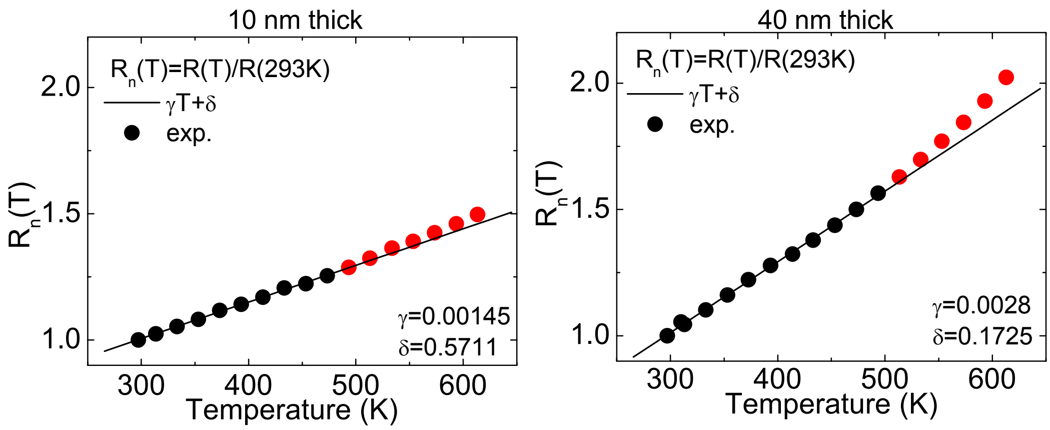

Figure 4.4: Resistance of (a) 10 nm and (b) 40 nm thick permalloy film, normalized to their room temperature resistance. The solid lines are linear fits to the data. The red colored data points are excluded from the fitting.

4.4 Resistance vs temperature in permalloy

To convert the estimated resistance into temperature, the temperature dependencies of the resistance in permalloy films are measured. Resistance measurements are conducted on films of 3 Ta/x $Ni_{81}Fe_{19}$/1 Ta/5 Ru deposited on Si/25 SiOx substrates. Units are in nanometers and x (x=10, 20, 40, 60, 80) represents the thickness of the permalloy layer. Four point probe resistance measurements are performed in a vacuumed anneal furnace. The temperature increment is set to 25 K. The maximum furnace temperature goes up to ~600 K. The temperature is increased at rate of ~1 K/min, and 15 min of waiting time is introduced before each resistance measurement. A magnetic field of 4000 Oe is applied throughout the annealing process. The obtained resistance is normalized to the resistance at room temperature to obtain

$$R_n(T) \equiv R(T)/R(T = 293K). \tag{4.10}$$

Figure 4.4 shows the temperature dependence of the normalized resistance measured for (a) 10 nm and (b) 40 nm thick permalloy films. The resistance shows a

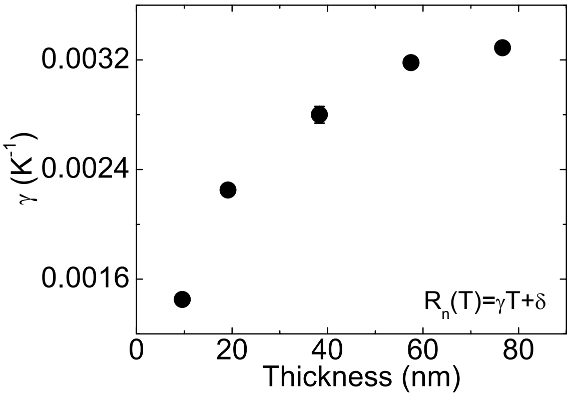

Figure 4.5: The slope of normalized resistance versus temperature plotted against the thickness of permalloy films.

thickness (nm)	γδ	
10	0.00145±2.1E-5	0.571±0.0082
20	0.00225±1.8E-5	0.359±0.0082
40	0.00280±6.1E-5	0.172±0.0277
60	0.00318±2.1E-5	0.048±0.0085
80	0.00329±1.8E-5	0.016±0.0075

Table 4.1: The slope γ and the offset δ of normalized resistance versus temperature are shown for various thicknesses of permalloy films.

linear dependence on the temperature and is fitted to a linear function

$$R_n(T) = \gamma T + \delta. \tag{4.11}$$

The fit is shown as a solid line and the fitting parameters are listed on the bottom right corner in each figure. The red circles in each figure represent irreversible resistance change due to diffusion or oxidation of the permalloy film. These data are excluded from the fitting. The slope γ of the normalized resistance versus temperature curve is plotted as a function of film thickness in Fig. 4.5. The slope saturates as the film thickness is increased. A complete list of the fitting parameters γ and δ are shown in Table 4.1.

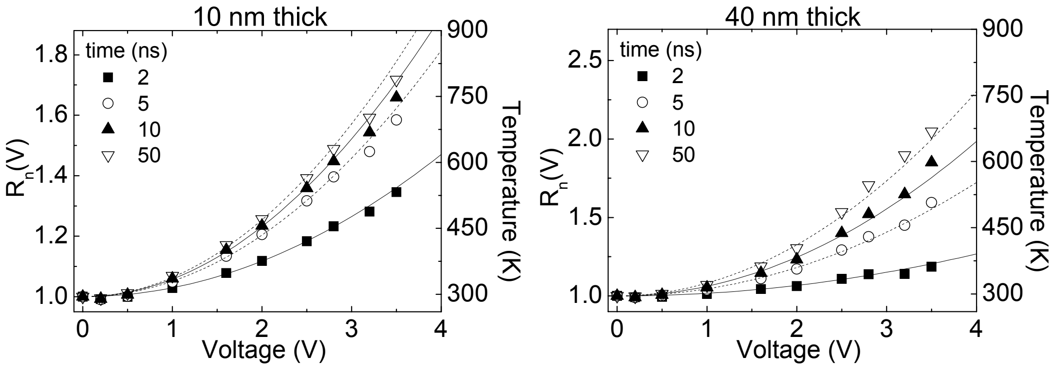

Figure 4.6: Normalized resistance value of (a) 10 nm and (b) 40 nm thick, 300 nm wide permalloy nanowires plotted against the input voltage. The resistance values at various time are plotted. The data are taken from that shown in Fig. 4.2 (c) and (d). The solid lines are fits to the data using Eq. (4.9). Estimated temperature of the nanowire are shown at the right axis.

4.5 Joule heating in permalloy nanowires

Equipped with all these formulas, the device temperature can be estimated by using Eq. (4.5), (4.8), (4.9) and (4.11). As an example, the estimated nanowire temperature is plotted as a function of the pulse amplitude in Fig. 4.6 (right axis) for (a) 10 nm and (b) 40 nm thick permalloy nanowires. Symbols represent the temperature at selected time. The temperature increases up to ~700-750 K at the maximum pulse amplitude at 50 ns. It is interesting to note that the temperature increases rapidly and tends to saturate for the 10 nm thick nanowire, whereas for the 40 nm thick nanowire, the increase is evenly divided in time and does not seem to saturate.

Next, the nanowire width dependence of the Joule heating is studied. Fig. 4.7 and Fig. 4.8 show the calculated (a) $f(t)$ and (b) $R_n(V)$ at 10 ns for 10 nm and 40 nm thick nanowire, respectively. The width of the nanowire varies from 80-100 nm. Since $f(t)$ does not depend on the pulse amplitude (see Fig. 4.3 (a)), representative curves when 2.0 V voltage pulse is applied are shown. For the 10 nm thick nanowire, $f(t)$ shows nearly no dependence on the nanowire width. On the contrary, for the 40 nm thick nanowire, the rise time of $f(t)$ increases when the width is increased. In

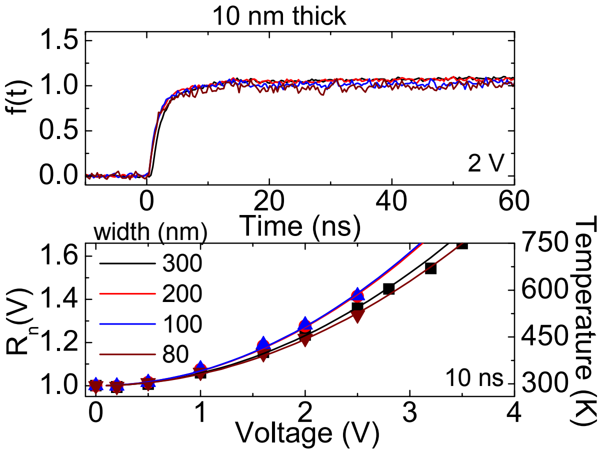

Figure 4.7: Nanowire width dependencies of the function f(t) (a) and the normalized resistance at 10 ns (b) are shown for 10 nm thick permalloy nanowires. Estimated temperature of the nanowire are shown at the right axis.

addition, for the 40 nm thick nanowires, $f(t)$ does not saturate even after ∼20 ns. With regards to $R_n(V)$ at 10 ns, there is little dependence on the wire width for 10 nm thick nanowires. On the other hand, for the 40 nm thick nanowires, the increase in temperature is greater for the narrower wires.

To illustrate these characteristics, the parameters obtained from the fittings using Eq. (4.8) and (4.9) are plotted against the wire width in Fig. 4.9. Figure 4.9 shows (a) the slope a after saturation and (b) the rise time τ of $f(t)$ before saturation. Clearly, the rise time τ is significantly larger for the 40 nm thick nanowires. Since the volume that needs to be heated is four times larger for the thicker nanowire, it takes longer to heat it up. For both film thicknesses, the wider the wire, the larger the rise time is. This is likely related to heat dissipation, which mainly takes place from the bottom surface of the nanowire to the substrate. Thus the dissipation rate would be proportional to the wire width. Consequently, it will take longer to heat up wider wires.

The slope (a) after saturation increases when the thickness and the width of the nanowire is increased. Since a seems to be proportional to the volume of the nanowire, it is likely that the gradual increase in the temperature after the first saturation is due

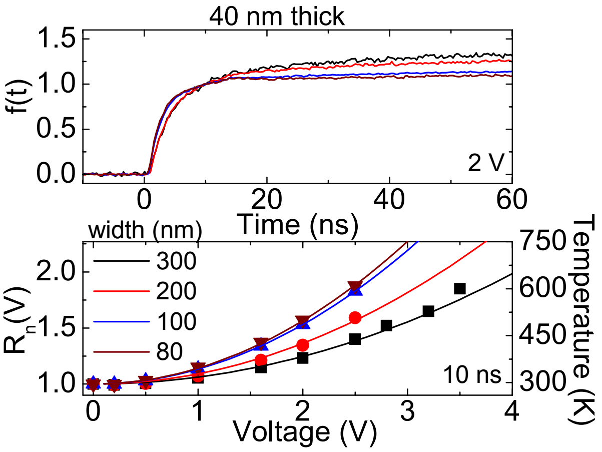

Figure 4.8: Nanowire width dependencies of the function f(t) (a) and the normalized resistance at 10 ns (b) are shown for 40 nm thick permalloy nanowires. Estimated temperature of the nanowire are shown at the right axis.

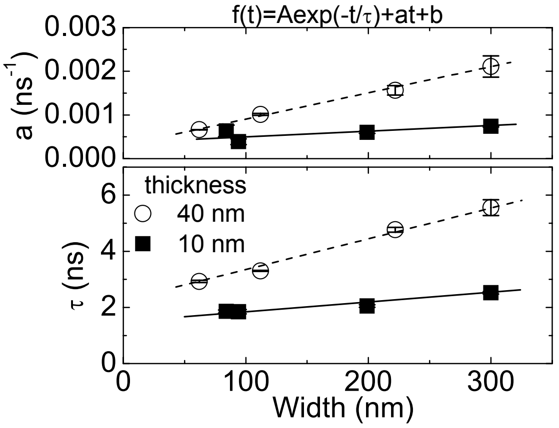

Figure 4.9: (a) Slope of the normalized resistance versus time after it the resistance saturates and (b) the rise time of the normalized resistance before saturation, obtained by fitting function f(t) to Eq. (4.8). The solid lines are guide to the eye.

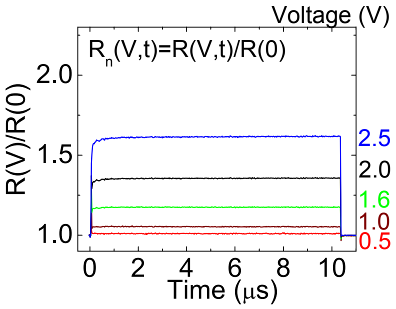

Figure 4.10: Time resolved resistance of 40 nm thick 200 nm wide permalloy nanowires normalized to its room temperature value. 10 μs long voltage pulse is applied to study the how long it takes for the resistance to saturate. The amplitudes of the input voltage pulse are shown on the right.

thickness	w (nm)	R_D (Ω)	R_C (Ω)	A	τ (ns)	a (ns^{-1})	b	α (V^{-2})
10 nm	84	1401	81	-1.040	1.859	6.34E-04	0.897	0.054
	94	1264	81	-1.077	1.845	3.89E-04	0.963	0.069
	199	638	81	-1.113	2.050	6.03E-04	0.973	0.068
	300	451	81	-1.187	2.520	7.39E-04	0.958	0.058
40 nm	62	427	68	-1.173	2.927	6.63E-04	0.979	0.141
	112	267	68	-1.183	3.302	1.01E-03	0.961	0.133
	222	168	68	-1.266	4.769	1.56E-03	0.983	0.091
	300	142	68	-1.265	5.554	2.11E-03	0.973	0.062

Table 4.2: Parameters characterizing the Joule heating of the nanowire.

to remanent heating. In order to study how long it takes to saturate the temperature in the thicker nanowires, a pulse generator (HP8116, 50 MHz bandwidth) that can generate micro-seconds long pulses is connected to contact line A to replace the one from Picosecond Pulse Labs. Fig. 4.10 shows the increase in the normalized resistance for a 200 nm wide 40 nm thick nanowire when a 10 μs long voltage pulse is applied. After the first saturation, it takes nearly $\sim$1 μs to reach the equilibrium.

A list of the parameters that characterize the Joule heating effect are shown in Table 4.2 as a reference. From these parameters, we can estimate the temperature when a voltage pulse with amplitude V and length t is injected, using Eq. (4.5), (4.8), (4.9) and (4.11).

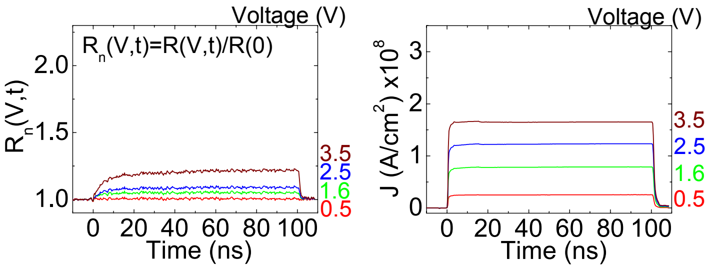

Figure 4.11: Estimated resistance (a) and the calculated current density (b) of 5 nm Ta/45 nm Rh contact lines (500 nm wide and few microns long). The amplitudes of the input voltage pulse are shown on the right of each panel.

Finally, Joule heating that occurs in the contact line is studied. The contact lines are made from 5 nm Ta/45 nm Rh films and patterned into 500 nm wide, few microns long wires, which attach to the $100 \times 150\mu\mathrm{m}^2$ contact pads. The resistance of the contact lines are $R \sim 80-85\Omega$ for 10 nm thick nanowires and $R \sim 65-70\Omega$ for 40 nm thick nanowires. Since these resistances are non-negligible, in particular for the thicker permalloy nanowires, it is important to characterize the heating in the contact line. Figure 4.11 shows the estimated resistance $R_n(V,t)$ (a) and the calculated current density (b) for the contact lines in the 10 nm thick permalloy nanowires. Considering the thickness (45 nm) of the contact line, the resistance increase is not as significant as the permalloy nanowires. However, the Joule heating is not negligible. Unfortunately, the relationship between the resistance and temperature is not available at this point. In order to characterize Joule heating of the permalloy nanowire more precisely, the contribution from the contact lines are needed to be taken into account.

Chapter 5

Depinning DW from a pinning center

5.1 Introduction

5.1.1 Background

Key to the successful operation of the racetrack memory is the controllable motion of DWs between pinning sites using current pulses. To begin with, it is important to provide well defined pinning sites in the device. There are several ways to create artificial pinning centers in magnetic materials. Owing to the advances of microfabrication technologies, one can pattern an artificial structural defect in magnetic nanostructures within the nanometer-scale length, which provides a precise positioning of the pinning center. In addition, the pinning strength of the pinning center can be controlled through the size of the artificial structural defect. On the other hand, we must be able to un-trap, or "depin" the DW from these artificial pinning sites using current pulses. Thus it is crucial to find a pinning center that provides both strong enough pinning, which can tolerate thermal activation, and "weak pinning" that can cause the DW to depin with low enough current density.

Note that in general, there are random pinning sites in magnetic materials due to either intrinsic structural or magnetic defects. The strength of these random pinnings differ depending on the type of defects and also on the host material. Therefore, it is also important to use a material that has little contributions from these random pinnings to avoid the DW being trapped in an undesired position. The coercivity of the material provides a good measure of the strength of these random pinnings. The pinning strength of these random defects are typically very small in soft magnetic materials. From this perspective, permalloy ($\mathrm{Ni}_{81}\mathrm{Fe}_{19}$) is chosen as a possible candidate for the racetrack memory.

5.1.2 Experimental Setup

A scanning electron microscopy (SEM) image of a typical nanowire is shown in Fig. 5.1. The distance between the two contact lines, labeled A and B, is 4 μm. The width of the nanowire varies from 80-300 nm. Both ends of the nanowire are tapered to a sharp point to prevent the formation of DWs outside the contact line [121] and to assist annihilation of any DW that enters this region. An artificial pinning center is patterned in section A-B, the region of the permalloy nanowire between contact line A and B. The pinning center is typically located either 2 or 3 μm away from line A. A triangular shaped pinning center (notch) is used with its depth varying from 10-30% of the wire width and its width having the same length with the depth. The notch is located along one edge of the nanowire.

High frequency probes are used to make contact to the devices. Most of the results shown in this chapter are taken using probes with bandwidth of dc-5 GHz. The local field generation method (chapter 3.3) is used to inject a DW into section A-B. A pulse generator (PG-A, Picosecond Pulse Labs, model 10075A) is connected to contact line A. A 50 Ω termination is connected to the other end of line A. This pulse generator is used to inject voltage pulse into line A which generates local magnetic fields. A dc-resistance measurement setup, consisting of a dc voltmeter (Keithley model 2002) and dc current source-meter (Keithley model 6430) connected in parallel, is connected to line B. This setup measures the total dc resistance of section A-B of the nanowire, contact lines A and B and the 50 Ω termination. A bias tee (Picosecond Pulse Labs, model 5547) is inserted between the dc measurement setup and the probe.

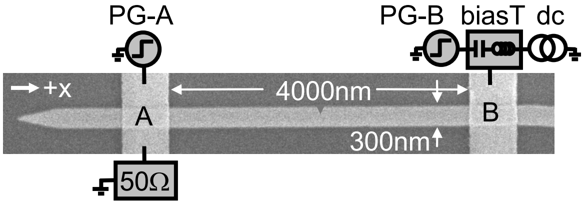

Figure 5.1: Scanning electron microscopy image of a permalloy nanowire (horizontal) and its electrical contacts (vertical lines). A schematic illustration of the quasi-static resistance measurement setup is overlaid on the image.

The capacitor end of the bias tee is connected to another pulse generator (PG-B, Picosecond Pulse Labs, model 10300B). This pulse generator is used to inject current pulses into the nanowire to excite or move the DW pinned at the pinning center.

5.2 Field-induced DW depinning

5.2.1 Correlation between DW structure and its resistance

The following procedure is used to inject a head to head (HH) DW into the wire. The nanowire is first magnetized along the wire by applying a large in-plane magnetic field H_{SAT} = -300 Oe in the -x direction (see Fig. 5.1 for the definition of x). Then a voltage pulse is passed along contact line A from pulse generator PG-A. The amplitude of the voltage pulse is set to pass large enough current into line A so that it generates a local magnetic field sufficiently large to reverse the magnetization direction of the portion of the nanowire that is located immediately underneath the line. Consequently, two DWs will be formed at both edges of line A. In addition, a global magnetic field, termed the injection field (H_{INJ}), hereafter, is applied to assist the nucleation and subsequent propagation of the DWs. H_{INJ} will cause the two DWs to move in opposite directions, one moving towards the notch (along the +x direction), and the other moving towards the wire's pointed end (along the -x direction). If H_{INJ} does not exceed the pinning field of the notch, one DW will consequently be trapped at the notch. The other DW will be annihilated at the pointed end. In order to create a tail to tail (TT) wall, the

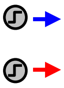

cycle	Field	Resistance
1	$-H_{SAT}$	
2	0	R_{SAT}
3	H_{INJ}	
4	0	R_i
5	H_B	
6	0	R_f
7	H_{SAT}	

Table 5.1: List of the field applied during the measurement to determine the critical current density. The resistance levels measured at the corresponding fields are shown on the right column. The field at which the injection voltage pulse, which subsequently injects a DW into section A-B of the nanowire, is applied is shown by the top blue arrow. The field at which the second voltage pulse, which triggers the depinning of the DW from the pinning center, is shown by the bottom red arrow. $\Delta R_i \equiv R_i - R_{SAT}$ and $\Delta R_f \equiv R_f - R_{SAT}$

direction of H_{SAT}, H_{INJ} and the polarity of the voltage pulse needs to be reversed.

The presence of a DW in section A-B of the nanowire is detected by measuring the dc resistance of the device. Due to the anisotropic magnetoresistance (AMR) of permalloy the presence of a DW lowers the resistance of the nanowire [74, 122]. Typically small contributions from the DW on the resistance[87] is ignored. Since this effect is small the resistance of the nanowire R_i is compared to that of its magnetized (no DW) state R_{SAT} immediately prior to injection of the DW. R_i and R_{SAT} are measured in zero applied field. See Table 5.1 for the field cycle used and the timing of the resistance measurements.

To illustrate this DW injection process, results from a 300 nm wide permalloy nanowire are shown in Fig. 5.2-5.5. A triangularly shaped notch with its depth being ~30% of the wire width is located 3 μm away from contact line A. As an example, a 2.1 V high 10 ns long voltage pulse is generated from PG-A to generate local field and inject a DW in section A-B. H_{INJ} = 12 Oe is used as the global assist field. Fig. 5.2 (a) plots the magnitude of the resistance change $\Delta R_i = R_i - R_{SAT}$ for a succession of measurements in which the magnetization and DW injection processes (cycle 1-4 in Table 5.1) are repeated many times. Note that $\Delta R_i = 0$ correspond to the magnetized states, whereas the non-zero ΔR_i values correspond to the state with

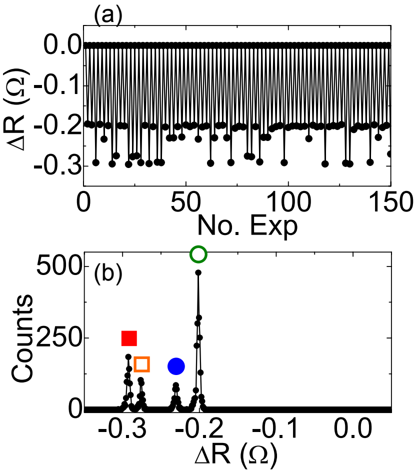

Figure 5.2: (a) Measurements of ΔR_i in a series of experiments in which the wire is first magnetized and a DW is subsequently injected (process 1-4 in Table 5.1). 2.1 V 10 ns long voltage pulse is used to inject a HH DW. H_{INJ}=12 Oe is used. (b) Histogram of ΔR_i values from (a). Note that only a subset of these data are shown in (a).

a DW in section A-B. For the latter, ΔR_i is negative in each case, consistent with AMR, but its magnitude varies from measurement to measurement. Figure 5.2 (b) shows a histogram of measured ΔR_i values. Four unambiguous peaks are observed in the histogram.

In order to investigate the origin of these distinct ΔR_i levels in the histogram, magnetic force microscopy (MFM) are used to image the state of the DW trapped at the pinning site. A DW is first injected into section A-B and subsequently being trapped at the notch using the above injection condition. ΔR_i is measured at zero field. The sample is then removed from the probe station and taken to the MFM. MFM imaging is conducted using a low moment tip to avoid strong interaction between the tip and the DW. After MFM imaging, the sample is brought back to the probe station to check whether the DW state has been changed or not. In order to check the state of the DW, the resistance of the device is first measured (R_i). A magnetic field is then applied and ramped up until the resistance of the device changes. The field is reduced to zero and the device resistance is recorded again (R_{SAT}). The

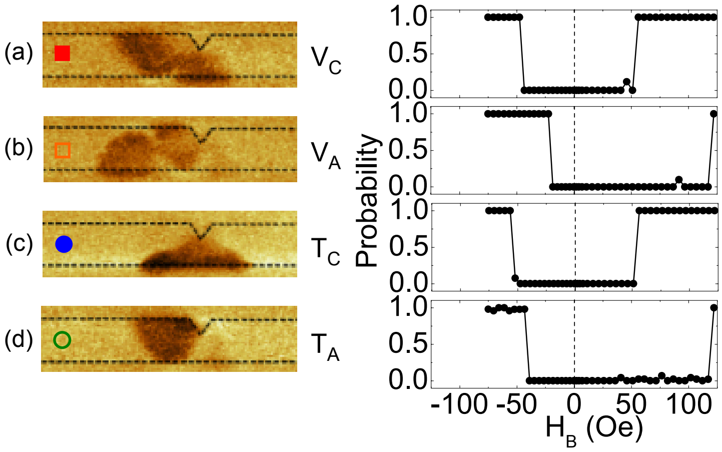

Figure 5.3: Left panels: MFM imaging of the four distinct ΔR_i states of Fig. 5.2 (b) (the symbols shown at the left side correspond to those in Fig. 5.2 (b)). Right panels: Field driven depinning probability plotted against the applied magnetic field for each DW state.

field at which the resistance change occurs is also recorded (see the discussion below regarding this field). The resistance difference $R_i - R_{SAT}$ will give the ΔR_i value of the DW after the MFM imaging. This value can be compared with the initial ΔR_i before the imaging to check the status of the DW.

The MFM images of the corresponding four distinct ΔR_i peaks are shown in the left panels of Fig. 5.3 (a-d). These experiments clearly demonstrate that the difference in the ΔR_i values correspond to different DW structures. The MFM images of these states are compared with micromagnetic simulations [123] to identify the underlying DW structures. The magnetic configuration of the nanowire with a notch is calculated by micromagnetic simulation. The notch profile is reproduced by loading the topography images of the nanowire, which are measured using atomic force microscopy (AFM). The MFM images are then reproduced by simulating a magnetic configuration whose magnetization divergence is close to those of the MFM images. In Fig. 5.4, the top panels show the MFM images and the corresponding simulated images are shown in the second and third panels. The second and third panels show the simulated images of the divergence of the magnetization and the direction of the local magnetization, respectively. Excellent agreement is obtained between the simulated and experimental images, allowing us to identify the four states as (a) transverse wall located in the notch (solid circle, labeled as T_C hereafter), (b) vortex wall located in the notch (solid square, V_C), (c) transverse wall located at one side of the notch (open circle, T_A) and (d) vortex wall located at one side of the notch (open square, V_A). Note that since the DWs are injected from the left side of the notch, i.e. from contact line A, they are more likely to be located at the left side of the notch. Interestingly, we find that the chirality of the DW determines whether the DW resides inside or to one side of the notch. This is because the energy of the DW is lowered (raised) when the component of its transverse magnetization within the notch is directed away from (to) the notch. We describe the chirality of these DWs as clockwise (T_C, V_C) and anticlockwise (T_A, V_A), respectively.

5.2.2 DW structure dependent depinning fields

Further insight into the characteristics of these different DW states is obtained by studying their field-induced depinning from the notch. DWs are injected into section A-B of the nanowire and subsequently being trapped at the notch using the aforementioned procedure. ΔR_i is measured in zero field to confirm the DW state prior to each depinning experiment. The field is then ramped up to a certain value H_B and is reduced to zero to measure R_f. R_f is compared to the nanowire resistance R_{SAT} of the magnetized state prior to the injection of the DW to obtain $\Delta R_f = R_f - R_{SAT}$. This process (Table 5.1 1-6 without the second voltage pulse application) is repeated for fields in the range from -120 Oe to 120 Oe, and is repeated 50 times for each field to obtain a statistical average. The depinning probability, the probability of ΔR_f equals zero at each field, is plotted against the ramped field H_B for each DW state and are shown in the right panels of Fig. 5.3. We define the depinning field H_{DP} as the minimum field at which the depinning probability exceeds 50%.

Interestingly, H_{DP} shows significant dependence on the DW state. For the DW with anti-clockwise chirality, the depinning fields are significantly different for positive and negative fields. Note that, since head to head DW is injected, positive depinning

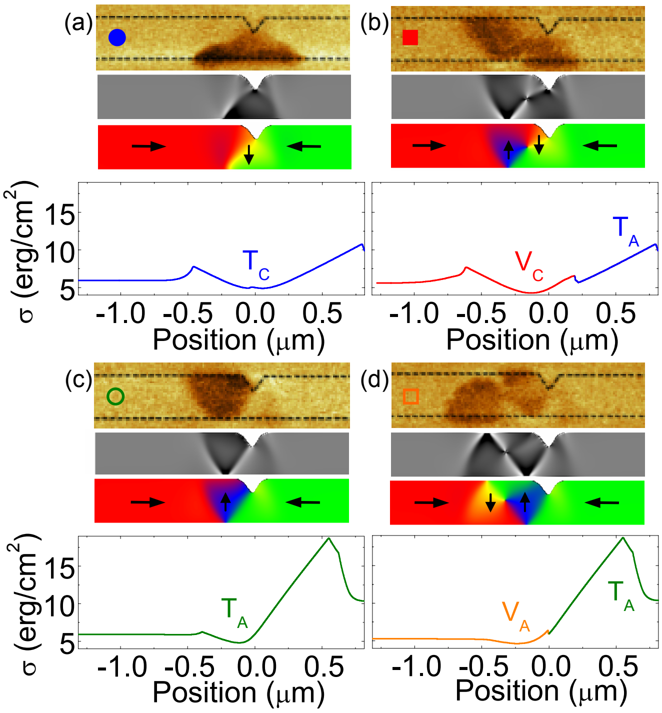

Figure 5.4: Each of the four panels (a)-(d), corresponding to the four distinct ΔR_i states of Fig. 5.2 (b), contain, from top to bottom: (1) MFM image (the symbols shown at the left side correspond to those in Fig. 5.2 (b)); (2) micromagnetic simulation of the divergence of the magnetization, which closely matches the measured MFM image; (3) the corresponding simulated image of the direction of the local magnetization, whose direction is indicated by color and arrows; (4) calculated pinning potential of the DW versus position along the nanowire. Note that the $\mathrm{V}_C(\mathrm{V}_A)$ states transform to $\mathrm{T}_C(\mathrm{T}_A)$ when the DW is moved across the notch to the right. The state of the DW is shown by color of the line and the label.

	Experiment		Simulation		
	H_{DP}^{+}	H_{DP}^{-}	H_{DP}^{+}	H_{DP}^{-}	H_{TRANS}
V_C	-45	54	-58	60	71
V_A	-20	120	-21	156	112
T_C	-54	54	-56	60	/
T_A	-41	119	-45	156	/

Table 5.2: Comparison of the depinning fields obtained experimentally and calculated using micromagnetic simulation for each DW state. H_{TRANS} represents the field at which the corresponding vortex wall transforms to a transverse wall.

field represents field needed to move the DW across the notch (toward +x direction) and depin it, whereas negative depinning field represents the field needed to pull the DW away from the notch (toward -x direction) and depin it. Since the DW is located on the left side of the notch for the anti-clockwise DWs, it is reasonable to infer that larger fields are needed to move the DW across the notch rather than to pull it away. For the clockwise DWs, the depinning fields are relatively symmetric in field, consistent with its location relative to the notch center. Note that in the MFM imaging measurements, H_{DP} is also measured after the imaging to confirm that the state of DW is not changed due to the stray fields from the MFM tips.

In order to provide a more quantitative understanding of the depinning fields, the notch pinning potentials for the four DW states are calculated by micromagnetic simulations. The pinning potential is calculated as follows. First, one of the four DW states is pinned at the notch. Second, a magnetic field is applied to move the DW. By incrementing the field $H_X(t)$ slowly and by using a large Gilbert damping constant ($\alpha = 1$) it is ensured that the DW follows the lowest energy path during its motion around the notch. The potential energy landscape σ for the DW is then obtained from the total energy $E_T(t)$ of the system minus the Zeeman contribution $-V_{sys}M_X(t)H_X(t)$, i.e. $\sigma = \left(E_T(t) + V_{sys}M_X(t)H_X(t) + E_0\right)/wt$, where V_{sys} is the total volume of the system, E_0 is the reference energy, $M_X(t)$ is the x-component of the magnetization and w, t are the width and thickness of the nanowire, respectively.

The bottom panels of Fig. 5.4 show the calculated pinning potentials for the

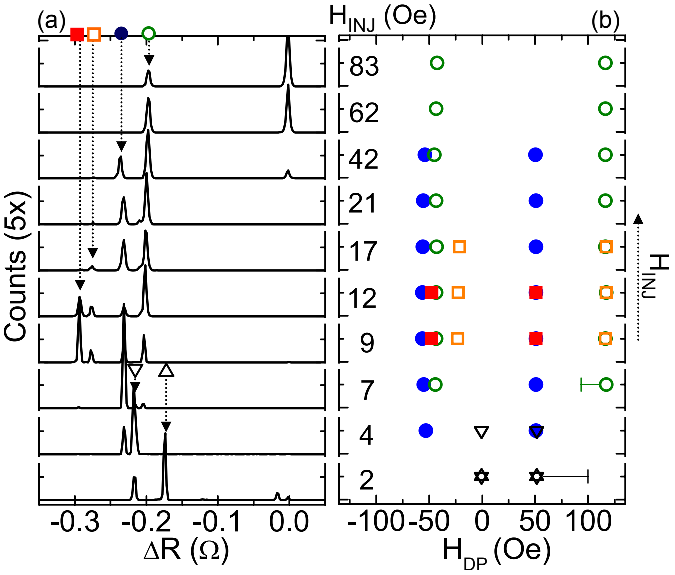

Figure 5.5: (a) Histogram of ΔR_i values as a function of injection field H_{INJ}. Corresponding injection fields for each histogram are shown in (b) (units: Oersted). Symbols indicate different DW states. (b) Depinning field for each peak observed in (a). Symbols correspond to those shown in (a). Error bars (20-80% depinning probability) are smaller than the symbols except where shown. The vertical axis represents the magnitude of the injection field with arbitrary spacing.

corresponding four DW states. In the system we used, $V_{sys} = 9.529 \times 10^{-12}$ erg and $E_0 = 0.16658 \times 10^{-9}$ erg. The difference in the positive and negative depinning fields can be understood from the asymmetrical shape of the pinning potential. For example, there is a big barrier to overcome for the anti-clockwise DW to move across the notch, thus giving large positive depinning fields. The depinning fields for each DW state can be extracted from the corresponding energy landscape and are listed in Table 5.2 together with the experimental values. The agreement between the experiments and simulations are good. The simulations also show that for the vortex walls, the DW transforms to a transverse state when it is moved across the notch. This is represented by the change in color of the pinning potentials in Fig. 5.4(b) and (d). The estimated field that cause the transformation are shown together in Table 5.2.

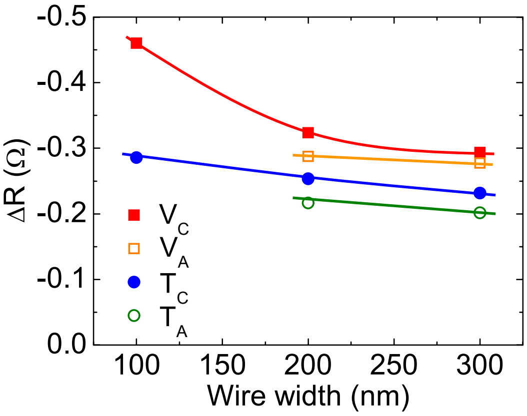

Figure 5.6: ΔR_i for the structures listed plotted against the nanowire's width. The DWs are trapped at a notch whose depth is designed to be 30% of the wire width.

The dependence of the ΔR_i and H_{DP} on the injection field H_{INJ} is summarized in Fig. 5.5 (a) and (b), respectively. For H_{INJ} larger than 4 Oe, the four main peaks are observed with the same H_{DP}. Note that neither the absolute value of ΔR_i nor H_{DP} depend on H_{INJ}, confirming that states with the same ΔR_i have the same magnetic state. The peak around $\Delta R \sim 0$ corresponds to states where no DW are formed. Interestingly, the relative size of the peaks in the histogram varies with H_{INJ}. Consequently, the number of accessible DW states can be varied by tuning H_{INJ}. Below 4 Oe, both the number and position of the peaks change abruptly. In this injection field range, the depinning field in the negative field direction is close to zero, indicating that the DW is not captured by the notch's potential well, and thus likely did not travel all the way to the notch. In other words, the "propagation field", the minimum field needed to move the DW along the nanowire, can be determined to be $\sim 4-5$ Oe.

Finally, ΔR_i for the vortex and transverse walls are plotted as a function of nanowire's width in Fig. 5.6. The notch is designed as triangular shape with its depth being 30% of the wire width. However, due to patterning issues, the actual depth of the notch is reduced for the narrower wires. The DW structure for the 100 nm wide nanowires are estimated from the depinning fields; MFM imaging was not

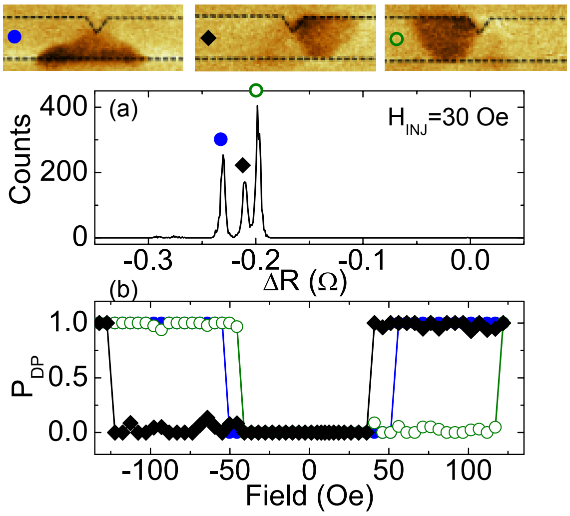

Figure 5.7: (a) Histogram of ΔR_i values when H_{INJ}=30 Oe. A 2.1 V 10 ns voltage pulse is used to inject a HH DW. Magnetic configuration corresponding to the three peaks in the ΔR_i levels are shown as MFM images. (b) Depinning probability of each DW state shown in (a) plotted against the applied magnetic field.

possible for these nanowires due to their weak pinning.

5.3 Overshoot effects in DW injection

Interesting effects occur when the injection field H_{INJ} is tuned to a particular field range. Fig. 5.7 (a) shows the ΔR_i histograms when H_{INJ} is set to 30 Oe and 2.1 V 10 ns long voltage pulse is used to inject a HH DW. In between the two transverse wall's ΔR_i levels, an additional peak arises at this injection condition. MFM image corresponding to this peak reveals that this new level represents a transverse (T_A) wall located on the right side of the notch (termed T_A^r hereafter). MFM images for the other two transverse walls are shown together for reference. Although the DW is injected from the left side of the notch (from line A), the MFM image indicates that the DW goes across the notch and get pinned at the right side of the notch.

To double check this observation, the zero current depinning field is measured. Figure 5.7 (b) shows the depinning probability plotted against the applied field for

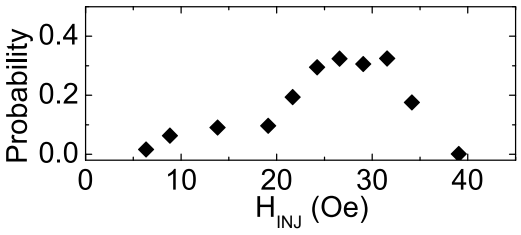

Figure 5.8: The probability of obtaining the T$_A$ wall trapped at the right side of the notch plotted as a function of H_{INJ}.

all three transverse walls, one T$_C$ wall and two T$_A$ walls with different positions (T$_A$ and T^r_A). As described before, the asymmetry in the positive and negative depinning fields ($H^{\pm}_{DP}$) derives from the position of the DW relative the notch center. If the DW sits on the left side of the notch, it costs more field to go across the notch, i.e. requires large H^{+}_{DP}, than to go to the left, i.e. requires small H^{-}_{DP}. For the T^r_A wall, the trend is the opposite, H^{-}_{DP} is significantly larger compared to H^{+}_{DP}, which indicates that the DW is located on the right hand side of the notch, consistent with the MFM imaging. In fact, $H^{\pm}_{DP}$ is completely symmetric with respect to that of the T$_A$ wall.

Since T$_A$ and T^r_A walls are symmetric with respect to the notch center, it is not obvious why the resistance level differs from each other. It is likely that due to the inhomogeneous current flow around the notch, the contribution of the DW to the resistance differs for the two walls. (The dc current flow is from line B to line A in Fig. 5.1, thus the symmetry with respect to the notch center is broken.)

The probability of observing T^r_A wall is plotted as a function of H_{INJ} in Fig. 5.8. The probability increases when H_{INJ} is set to 25-30 Oe. It is rather surprising that the probability of observing T^r_A wall can increase up to 30% in certain field range. As seen in Fig. 5.4 (a-d), there is quite a large barrier to overcome for the DW to go across the notch. Considering the depinning fields H^{+}_{DP} of the other DW structures, 25-30 Oe is too small for any of the DW states to move across the notch (see Table 5.2). It is likely that the appearance of the T^r_A wall in this field range is due to an dynamical overshoot effect of the DW entering the notch potential.

An analogue phenomena can be observed in classical mechanics. Consider a ball rolling down a board and a dent is placed in the middle of the board. Compare the slope of the board needed for the ball to move out from the dent when it is initially place in the dent or if it is initially placed above the dent and rolls down the hill to enter the dent. The slope needed when the ball is placed above the dent is nearly half of that when it is placed in the dent. This is because when the ball is placed above the dent, it obtains momentum by moving down the board and thus when it enters the dent it possesses finite momentum, which is not the case when it starts from the dent. The same condition applies for the DW, where the field (slope of the board) required to observe T_A^r wall (to see the ball go across the dent) is nearly half of the depinning fields of the DWs which are at rest in the notch (the slope needed to get the ball out from the dent when it is initially located in the dent).

5.4 Current-assisted DW depinning

We now apply current pulse to trigger the depinning of the DW from the pinning center. One of the important purpose of this chapter is to investigate the factors that determine the minimum current density needed to depin a DW from the pinning center (termed critical current density, hereafter). With regards to the racetrack memory, it is crucial to understand the relationship between the pinning strength and the critical current density. As stated before, on one hand, it is desirable to use a strong pinning center to avoid thermal fluctuation of the trapped DW. On the other hand, we must depin the DW from the pinning center to move it to the next pinning center, which indicates that too strong pinning may not be suitable. Thus the proper pinning strength needs to be determined. In addition, when the dimensions of the nanowires are changed, perhaps due to scaling, it is likely that the structure of the DW will change. Thus it is also important to understand the effect of the DW state trapped at the pinning center on the critical current density.

One obvious way to study these effects is to use nanowires with different pinning centers, wire widthes and film thicknesses. However, since each nanowire may exhibit different characteristics due to the uncertainty of the lithography techniques, it may become ambiguous to compare the critical current density from wire to wire, unless a large number of sampling is conducted. It is shown in the previous section that we can trap different types of DW at the same pinning center. Furthermore, these DWs exhibit different depinning fields, indicating that the pinning strength they feel from the same pinning center is different. Thus this is an ideal system to study the dependence of the critical current density on the pinning strength and the type of DW. In addition, the influence of magnetic field on the depinning process is studied.

5.4.1 Dependence on magnetic field

Again, we start from the results of 300 nm wide nanowire with a triangularly shaped notch located 2 μm away from contact line A. The depth of the notch is $\sim$30% of the wire width. First a DW is injected in the nanowire using the aforementioned injection procedure. The DW injection condition is chosen such that the number of accessible DW states is maximum. For this wire, a 2.1 V high 10 ns long voltage pulse is used to inject a DW in section A-B and $H_{INJ} = 12$ Oe is used (see Fig. 5.5 (a) for details). ΔR_i is measured after the injection process to determine the state of the trapped DW. Four DW states, two vortex walls and two transverse walls, each with two chiralities, can be pinned at the notch.

An external bias field (H_B) is then applied along the x-direction to assist the current induced depinning. With H_B turned on, a voltage pulse, generated from pulse generator B (PG-B in Fig. 5.1) is injected into the nanowire via contact line B. After reducing H_B to zero, the resistance (R_f) of the device is measured and compared to magnetized state resistance level (R_{SAT}) measured prior to the DW injection. The difference of the two resistance level, defined as $\Delta R_f = R_f - R_{SAT}$ gives the information of whether the DW is depinned and ejected from section A-B. The definitions of the applied field cycle and the corresponding resistance measured at each field are shown in Table. 5.1.

In order to obtain statistical average, this injection/depinning process (all cycles shown in Table. 5.1) is repeated 50-100 times at a fixed H_B, pulse voltage and pulse length. When a positive voltage pulse is injected from line B, a positive current will flow in the nanowire. Positive current is defined as the electrons flowing in the positive x direction in Fig. 5.1.

The voltage pulse injected from line B into the nanowire can be considered as a current pulse injected into the nanowire. However, since a constant voltage pulse generator is used, the actual current density flowing in the nanowire depends upon its resistance which may increase during the pulse due to Joule heating. Thus we correct the current density to the actual current density that flows into the nanowire which is estimated from the increase in the nanowire resistance during the pulse application (see Fig. 4.2 (c) for the resistance increase). In addition, when the Joule heating effect takes place, the amplitude of the current pulse is no longer constant within the pulse (see Fig. 4.2 (e) for the change in the current density during the pulse). Therefore we take the current density at the end of the pulse, not the maximum current density, as the "actual" current density.

Figure 5.9 (a-d) show the depinning probability plotted as a function of applied magnetic field H_B and pulse voltage. The voltage pulse length is fixed to 4 ns here. The initial structure of the DW is indicated at the bottom left of each panel. The color scale represents the probability of the DW being depinned either by field or by the combination of field, if any, and current. Red (blue) corresponds to 100% (0%) depinning probability. When H_B is below the zero current depinning field ($H_{DP}^{\pm}$) (see Fig. 5.3), non-zero current density is needed to depin the DW. The minimum current density needed to cause 50% or more depinning, i.e. the critical current density $J_C(H_B)$, is plotted in Fig. 5.9 (e-h) as a function of the magnetic field for the four initial wall structures.

The measured field dependencies of $J_C(H_B)$ show similar characteristics for DWs with the same chirality. For example, T_A and V_A walls show constant J_C over a large range of H_B at high positive fields. At negative H_B, J_C rapidly increases as H_B is reduced from the depinning field. For T_C and V_C walls, J_C is nearly symmetric with respect to the applied field direction. The blue lines represent the calculated critical current density using the 1D model of the DW. Details of this calculation and discussion about the comparison to the experimental results are discussed in Section 5.5. For most of the wall structures, the extrapolated J_C at zero field show similar values, i.e. $J_C(0) \sim 3 \times 10^8$ A/cm^2.

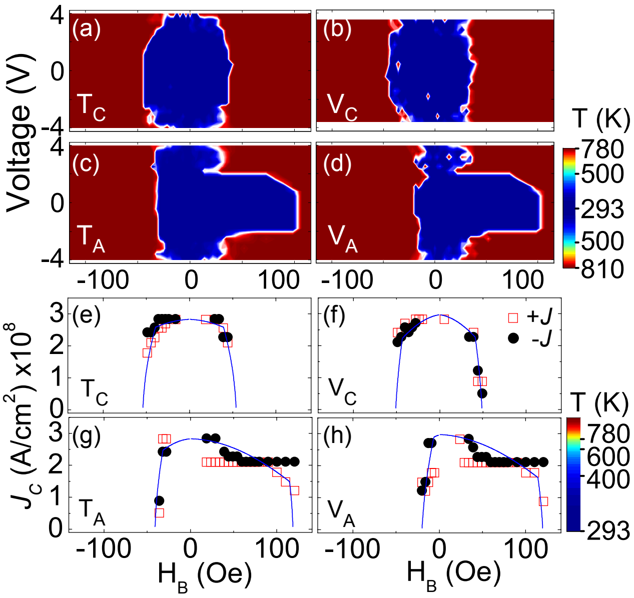

Figure 5.9: (a-d) Depinning probability maps plotted as a function of magnetic field H_B and the amplitude of the voltage pulse. Applied voltage pulses are 4 ns long. The color scale represents the depinning probability. Each panel shows the probability map for the corresponding initial DW structure indicated at the bottom left. Device temperature corresponding to the applied voltage pulse is shown at the right as color scales. (e-f) Critical current density extracted from the maps shown in (a-d) plotted as a function of H_B for the four initial DW states. Lines are a calculated using the 1D model. Device temperatures corresponding to the current density are shown at the right as color scales.

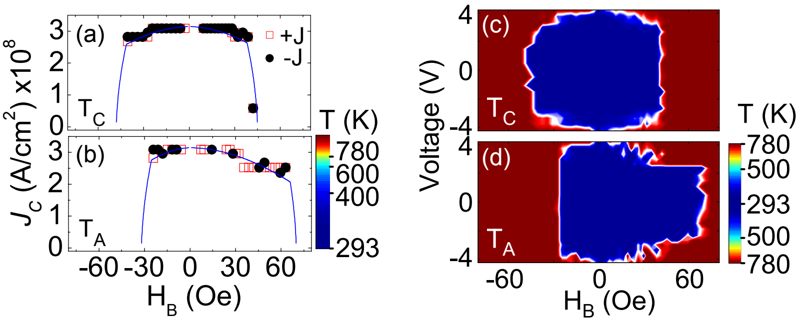

Figure 5.10: Depinning probability maps (a-d) and the critical current density (e-h) plotted as a function of magnetic field H_B for a 200 nm wide nanowire. Notch depth is 30% of the wire width. See Fig. 5.9 for details of the description of the figures.

The temperature reached during the 4 ns long pulse can be estimated by converting the measured resistance after the end of the 4ns pulse application to the device temperature using the dc resistance-temperature relationship measured for a permalloy film with the same thickness (see Fig. 4.4 for the conversion). Substituting the $t = 4$ ns in Eqs. (4.5), (4.8), (4.9) and (4.11) and using the parameters obtained in Chapter 4, the device temperature corresponding to each amplitude of the pulse voltage can be obtained. The estimated temperature corresponding to the current density are shown as color scales at the right side of the figures. The maximum temperature approaches the Curie temperature of permalloy (∼850K) at the highest currents needed to depin the DWs near zero applied field [124].

The depinning probability maps and the critical current densities of a 200 nm wide nanowire are shown in Fig. 5.10 (a,b) and (c,d), respectively. The notch depth is ∼30% of the wire width and is located 3 μm away from line A. Again, a 4 ns long voltage pulse is injected from line B to trigger the depinning. The device temperature reached at the end of the pulse is shown at the right side of each panel. The initial DW states are all transverse walls in this figure, which were confirmed by MFM imaging.

Similar characteristics are observed for the 200 nm wide nanowires. For example, the critical current density near zero field are similar for all the DW states. A field independent $J_C(H_B)$ are observed at positive high fields for the T_A walls. As was

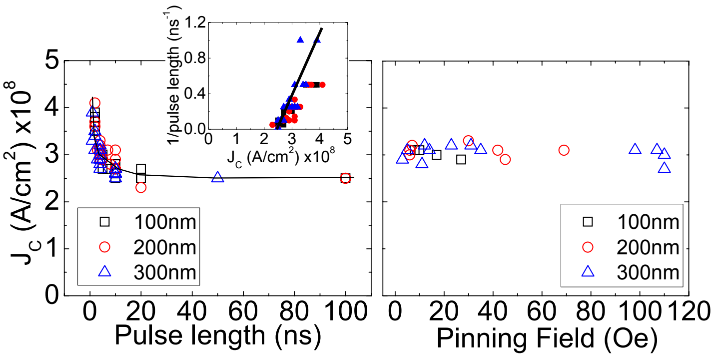

Figure 5.11: (a) Pulse length dependence of the critical current density at zero field estimated from extrapolating $J_C(H_B)$ to zero field. Inset shows the inverse of the pulse length plotted against the critical current density. (b) Zero field critical current density as a function of the pinning field of the notch. The pinning field is the average of positive and negative H_{DP}.

shown from the Joule heating experiment (Fig. 4.7), the device maximum temperature at the end of the 4 ns pulse depends little on the wire width, thus the maximum temperature reached at $J_C(0)$ is similar. Note that the depinning probability at zero field seems to be higher when the wire width is reduced. The cause of this difference is not clear yet.

The extrapolated critical current density near zero field for all transverse walls are plotted in Fig. 5.11 (a) and (b) as a function of the pulse length and the notch pinning strength, respectively. Data from 100-300 nm wide nanowires are shown all together. In both figures, the average of the positive and negative $J_C(0)$ are shown, where each $J_C(0)$ is the average of the extrapolated critical current density from positive and negative fields. In Fig. 5.11 (a), the critical current decays and saturate at longer pulse length. The inset shows the critical current dependence of the inverse of pulse length. The relationship is approximately linear. In Fig. 5.11 (b), the notch pinning strength is estimated by taking the average of zero current depinning fields H_{DP}^{+} and H_{DP}^{-}. $J_C(0)$ shows little dependence on the pinning potential strength, consistent with the results from a single nanowire, where $J_C(0)$ is similar for different DW states experiencing different pinning strength when located at the same notch.

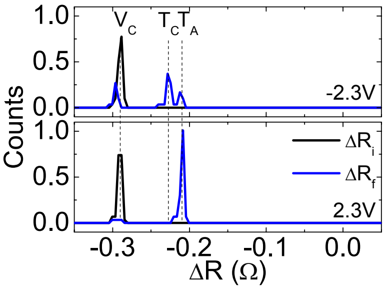

Figure 5.12: Histograms of the ΔR values before (black) and after (blue) (a) 2.3 V, (b) -2.3 V 4 ns long voltage pulse application. The applied magnetic field ranges from -5 Oe to 5 Oe to obtain the histogram.

5.4.2 Subthreshold current induced transformations

Thus far, the depinning probability was measured to study the dependence of the critical current on the wall structure, notch pinning strength and wire width. For the transverse walls, the zero field critical current seems to be relatively insensitive to these parameters. In order to obtain a detailed insight into this current-assisted depinning process, we study the effect of the current pulse below $J_C(H_B)$, i.e. the subthreshold characteristics. Since the correspondence between the resistance level (ΔR) of the nanowire and the DW state is known, ΔR_f provides information of the state of the DW after the current pulse application, i.e. if any transformations between different DW states were to occur, it is detectable.

As an example, Fig. 5.12 show the histograms of the ΔR values before (ΔR_i) and after (ΔR_f) the voltage pulse application. The V$_C$ wall is chosen as the initial DW state; the other DW states in the ΔR_i histogram are thus filtered out. A 4 ns long, 2.3 V (a) or -2.3 V (b) voltage pulse is injected into the nanowire. The applied field H_B ranges from -5 Oe to 5 Oe. The transition of the DW states are clearly seen in the ΔR_f histograms. From these histograms, the most probable DW state can be determined and are represented by the ΔR_f value corresponding to the peak position.

The most probable ΔR_f value after the current pulse application are mapped in the right panels of Fig. 5.13 (a-d) to show the most probable final state after the voltage pulse application. These maps represent the subthreshold characteristics of the those shown in Fig. 5.9 (a-d). Note that the maximum voltage in these maps are only 60% of that shown in Fig. 5.9 (a-d). The initial DW structures are listed at the left of each panel and the device temperature corresponding to the end of the 4 ns long pulse is again shown by the color scale at the right side of the bottom panel. To clarify the correspondence between the resistance level and the DW structure, the resistance level is color scaled. Four different colors, light blue (T_C), light grey (T_A), red (V_C), light red (V_A) represent the four DW states, whereas dark blue represent the magnetized state. One can clearly see transitions between different DW structures below $J_C(H_B)$[74]. The T_C wall appears to be the most stable state against current. The T_A wall transforms to either T_C or V_C at low H_B depending on the direction of current. Vortex walls also show transitions to transverse walls at high current density. Thus the wall chirality as well as the basic structure can be changed with a short current pulse. Note that the V_A wall transforms to a T_A wall without any current when H_B exceeds ~50 Oe, consistent with micromagnetic simulations, as shown in Fig. 5.4 (d). Interestingly, the depinning for high positive H_B for T_A and V_A walls likely involves wall structure transformations, i.e. $J_C(H_B)$ here represents the current density needed to transform the wall into either the T_C or V_C wall, which is then immediately depinned at these high H_B. The DW transformations observed here can be attributed to vortex core motion induced by spin polarized current [38, 125].

Up to this point, all of the results are from head to head (HH) DWs pinned at the notch. Since the current flow through the nanowire is not perfectly homogeneous, largely due to the 0.5 nm TaN/5 nm Ru layer deposited on top of permalloy that shunts the current, the Oersted field, or the self field from the current pulse, may play a role in the depinning process. This effect can be studied by comparing the depinning process between HH and tail to tail (TT) walls. The subthreshold characteristics maps of the TT wall are shown in the left panels of Fig. 5.13 (a-d).

From Fig. 5.13 (a-d), there is no significant difference between the HH and TT walls in the subthreshold current induced transformations when the initial structure is a transverse wall. However, for the vortex walls, the current induced transformation occurs for much lower current for the the TT walls, as evident from Fig. 5.13 (c) and (d). This could be attributed to the transverse field effect, which can cause the

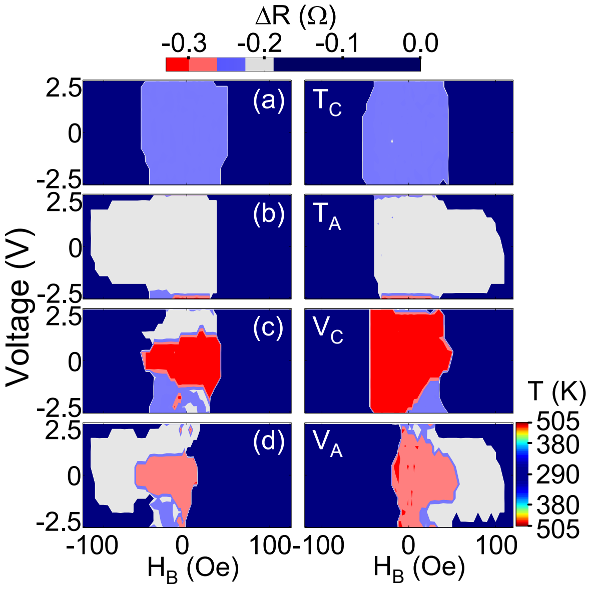

Figure 5.13: (a-d) Stability phase diagram for the four DW states shown in Fig. 5.9 (a-d). The most probable ΔR_f level after the application of a 4 ns long voltage pulses is plotted as a function of the pulse voltage and H_B. Color scale represent ΔR_f and are divided into five colors to correlate them to the DW states. Device temperature corresponding to the applied voltage pulse is shown at the right as color scales.

vortex core to move to the edge of the nanowire that results in transformation to transverse walls. When the initial wall structure is a transverse wall, a vortex core must be nucleated from the edge of the nanowire to initiate transformations, which may require larger fields. On the other hand, when the current direction is fixed, the final DW state after the transformation seems to be the same regardless of the DW type (either HH or TT). For example, when a negative voltage pulse is applied to a V_C wall, the final state tends to be the T_C wall at zero field. This effect cannot be explained by the sole effect from the transverse field. It is interesting to note that vortex core motion can also be induced by spin transfer torque. It is likely that the combination of spin transfer torque and the transverse field effect are causing the DW transformations.

5.4.3 Dependence on current pulse length

Next, the effect of the pulse length on the current induced depinning and transformations is investigated. In order to avoid Joule heating that causes damage to the device when long, high-amplitude pulses are used, the maximum amplitude of the voltage pulse is limited to 2.5 V. In addition, it is important to note that at higher pulse voltages, the current density is no longer constant during the pulse application (see Fig. 4.2 (e)). The current density through the nanowire is roughly constant up to 2.5 V.

Exemplary data of the pulse length dependence are shown from 300 nm wide nanowire with a triangularly shaped notch located $\sim 3\mu$m away from contact line A. The notch depth is roughly 30% of the wire width. The same injection condition is used, 2.1 V 10 ns voltage pulses with $H_{INJ} = 12$ Oe. Figure 5.14 and Fig. 5.15 show the depinning and transformation probability maps plotted as a function of the amplitude and length of the voltage pulse. The initial wall structures are the T_A wall (Fig. 5.14) and V_C wall (Fig. 5.15). Maps for both HH wall (a) and TT wall (b) are shown in each figure. In Fig. 5.14 (a) and (b), the top row represents the depinning probability maps, whereas the second and third rows show maps of the transformation probability to T_C and V_C walls, respectively. Similarly, in Fig. 5.15 (a) and (b), the top row represents the depinning probability maps, whereas the second and third rows show maps of the transformation probability to T$_C$ and T$_A$ walls, respectively. Each column show maps at fixed magnetic field (H_B) applied during the pulse. The applied fields are indicated at the top of each row. Transformation probability to the V$_A$ wall is not shown since the probability was low.

For the T$_A$ wall, most of the events, either depinning or transformation, are nearly independent of the voltage pulse length. It is also clear from these maps that the DW transformation plays an critical role in current induced depinning. For example in Fig. 5.14 (a), when the magnetic field is small, transformation to the T$_C$ wall occurs preferably. As the field is increased, the voltage range where the transformation occurred in the lower field maps now shows depinning. Another example can be found in Fig. 5.14 (b), at -41.0 Oe, where at low negative voltages, transformation to the T$_C$ wall occurs, however as the magnitude of the voltage is increased, the depinning process takes over.

For the V$_C$ wall, the pulse length dependence is more complex. The overall trend is similar to the T$_A$ wall, where transformation occurs first at low field, low voltage and depinning takes place at higher fields, high voltage. However, the pulse length plays a more significant role in this case, and in some occasions, the probability of either depinning or transformation oscillates with the pulse length. This is a remarkable effect and will be discussed in the next two sections. As was touched in the previous section, the TT vortex walls are more vulnerable to the current excitation; transformation and depinning are observed at lower voltages. Unfortunately, the injection probability of the V$_A$ wall was too low to plot these maps in these samples.

(a) Initial state: T_A (HH)

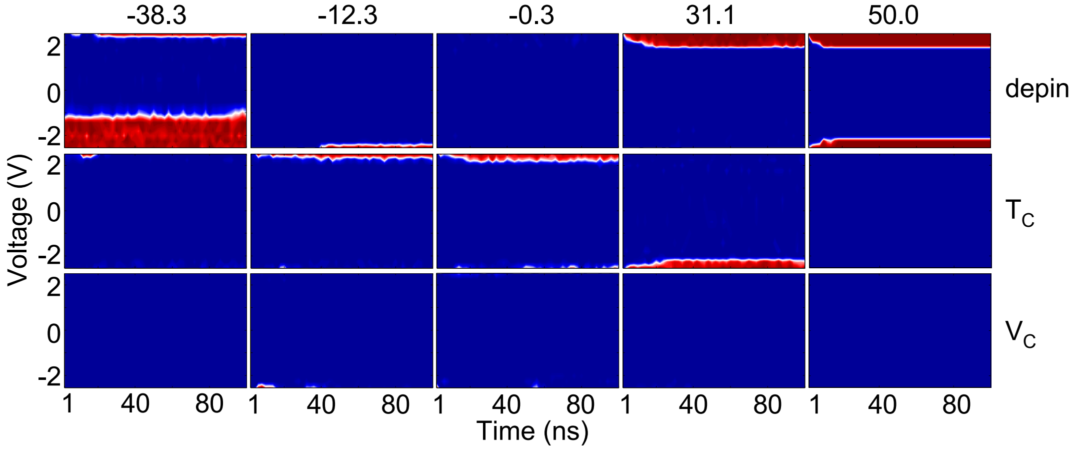

(b) Initial state: T_A (TT)

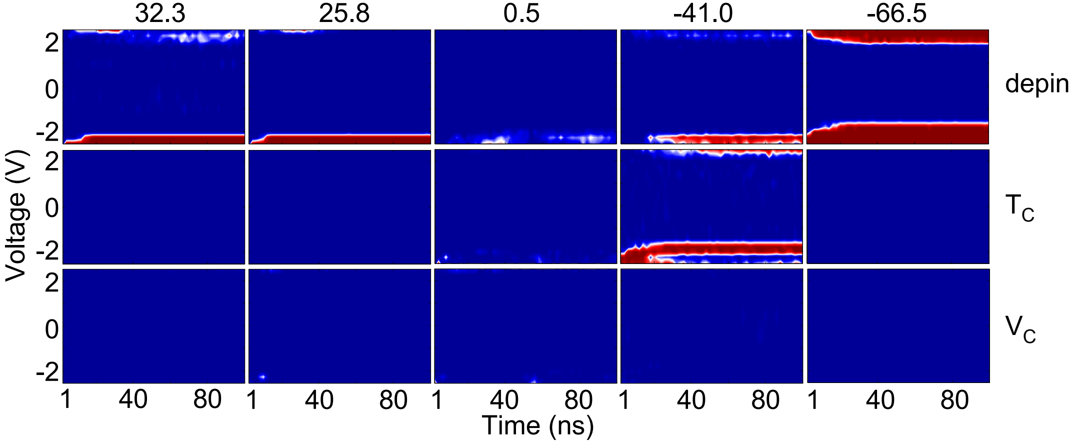

Figure 5.14: (a, b) Depinning and transformation probability maps plotted as a function of pulse voltage and pules length. The initial wall structures are (a) HH T_A wall and (b) TT T_A wall. The top row in each panel show the depinning probability maps, whereas the second and third row show maps of the transformation probability to T_C wall and V_C wall, respectively. Each column show maps at a fixed field, which are indicated at the top.

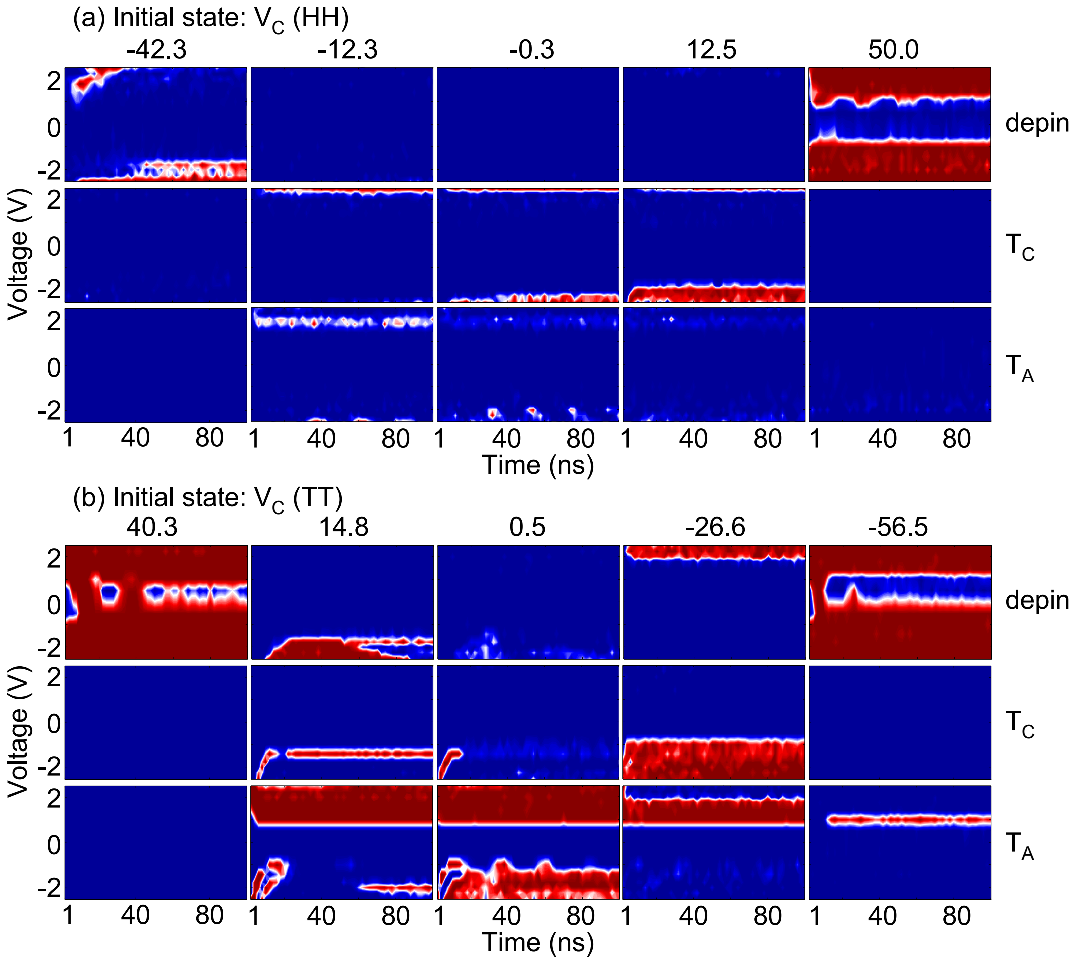

Figure 5.15: (a, b) Depinning and transformation probability maps plotted as a function of pulse voltage and pules length. The initial wall structures are (a) HH V_C wall and (b) TT V_C wall. The top row in each panel show the depinning probability maps, whereas the second and third row show maps of the transformation probability to T_C wall and T_A wall, respectively. Each column show maps at a fixed field, which is indicated at the top.

5.5 Analysis using the 1D model

5.5.1 Model description

In this section, we leave the experimental results and turn on to understand the underlying physics of depinning DWs using the one dimensional (1D) model. As was introduced in Chapter 2, the two ordinary differential equations derived from the LLG equation is used as a starting point, i.e. Eq.(2.29) and (2.30). For simplicity, the effect of the transverse fields are neglected here, i.e. set a_x and a_z zero. Thus the starting differential equations are

$$(1+\alpha^2)\dot{x} = \alpha(a - px + \beta v) + (\sin 2\psi + v) \tag{5.1}$$

$$(1+\alpha^2)\dot{\psi} = (a - px + \beta v) + \alpha(\sin 2\psi + v) \tag{5.2}$$

The pinning potential is assumed to take a parabolic shape, as defined in Eq.(2.26). In order to acquire an intuitive picture of how the DW moves within the potential well when excited by current and/or field, we start from numerically solving Eq.(5.1) and (5.2). Fig. 5.16 (a) and (b) show the temporal evolution of the position q and the angle ψ of the DW when a magnetic field is applied at time zero. The position and angle show damped oscillation with a 90 degree phase difference. In the steady state limit, or at equilibrium, ψ is zero whereas q takes a non-zero value. The horizontal dotted lines are the boundaries of the pinning potential well. The motion of a DW within the well is better visualized when the angle ψ is plotted against the position q, typically called a phase space plot in classical mechanics. Figure 5.16 (c) shows this phase space plot. The DW trajectory is elliptic and moves toward the center of the spiral due to damping. The center of spiral is the called the fixed point (q_f,ψ_f), which corresponds to the equilibrium value.

The trajectory of a DW when a dc current is applied at time zero is shown in Fig. 5.17. On contrary, now the equilibrium point is shifted in the vertical axis, i.e. q_f is zero whereas ψ_f is now non-zero. This is the most significant difference in field induced and current induced DW motion. Whereas the net effect of the magnetic field is to shift the equilibrium position of the wall, the resulting effect of the current

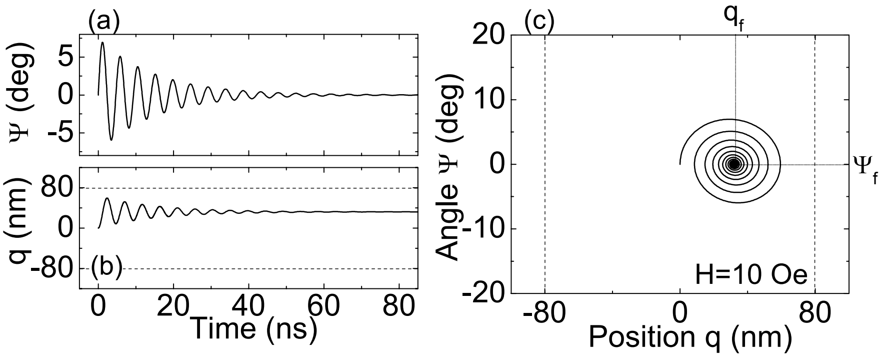

Figure 5.16: Numerical calculations showing the temporal evolution of (a) the angle and (b) the position of the DW. (c) Phase space plot constructed from (a) and (b). Magnetic field of 10 Oe is applied. No current is applied (u=0). The parameters used are H_K=750 Oe, Δ=22 nm, α=0.01, β=0. The pinning potential is defined as V=2×10^4 erg/cm^3 and d=150 nm.

is to change the equilibrium angle of the wall.

The fixed point (x_f,ψ_f) can be easily derived by setting $\dot{x}$ and $\dot{\psi}$ to zero in Eqs. (5.1) and (5.2). The results are

$$x_f = \frac{a + \beta v}{p} \tag{5.3}$$

$$\psi_f = \frac{1}{2}\arcsin(-v). \tag{5.4}$$

The dynamic effects of a DW trapped in a pinning potential derives from the first few spirals in the DW trajectory. In particular, the most pronounced effect occurs within the first spiral. Thus it will be useful to deduce an analytical formula for the first spiral. When the damping constant is small, the first spiral can be approximated with a closed ellipse. Later it is shown that the damping constant of the spiral is directly proportional to Gilbert damping constant α, and this number is typically small in materials (permalloy) that we are interested in. In order to obtain an analytical form of this closed ellipse, we thus assume $\alpha = 0$ and use a parametric approach. First

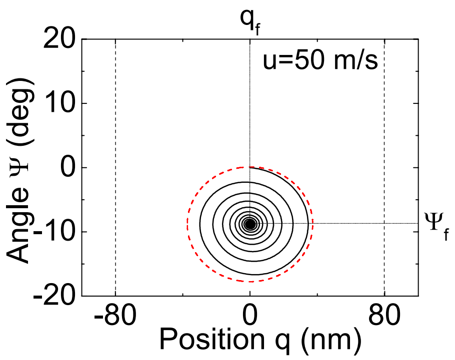

Figure 5.17: Solid line: Numerical calculations showing the phase space plot when a current (u=50 m/s) is applied at time zero. No magnetic field is applied. Dotted line: The first spiral of the DW trajectory calculated using Eq. (5.7). The parameters used are H_K=750 Oe, Δ=22 nm, α=0.01, β=0. The pinning potential is defined as V=2×10^4 erg/cm^3 and d=150 nm.

divide Eq. (5.1) with (5.2).

$$\frac{\dot{x}}{\dot{\psi}} = \frac{\partial x}{\partial \psi} = \frac{(\sin 2\psi + v)}{(a - px + \beta v)} \tag{5.5}$$

Direct integration of the Eq. (5.5) gives

$$-\frac{1}{2}px^2 + (\beta v + a)x - \left(-\frac{1}{2}px_0^2 + (\beta v + a)x_0\right) = \frac{1}{2}\cos 2\psi - v\psi - \left(\frac{1}{2}\cos 2\psi_0 - v\psi_0\right) \tag{5.6}$$

where the integration limits are taken from time 0 (x_0, ψ_0) to time t (x, ψ). As will be clear later, when the angle ψ becomes large, the DW trajectory is no longer an ellipse. Here we consider the case where ψ is small, i.e. only the elliptical trajectories. The non-linear terms in Eq. (5.6) can therefore be linearized. Since ψ is assumed to be small, the center of the ellipse ψ_f is also small and thus we expand the cosines in Eq. (5.6) around $\psi = \psi_f$. The resulting equation reads

$$\frac{(x - x_f)^2}{R_x^2} + \frac{(\psi - \psi_f)^2}{R_\psi^2} = 1 \tag{5.7}$$

As evident from the form of Eq. (5.7), the trajectory is a closed ellipse. The

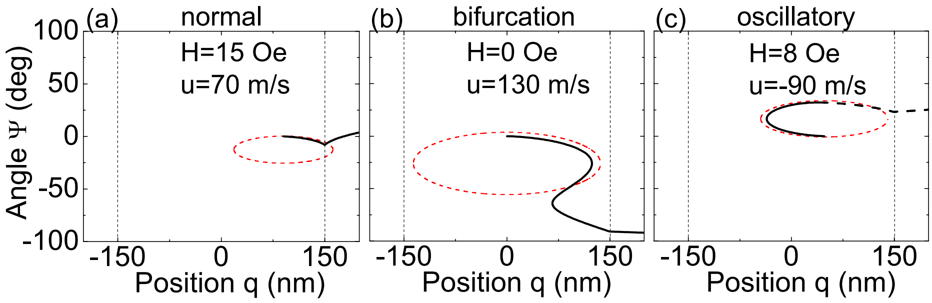

Figure 5.18: (a-c) Solid black lines: Numerical calculations showing the phase space plot when listed values of current (u) and field are applied. Dashed black line in (c) represent the trajectory of the DW after the current is turned off. Dotted red line: The first spiral of the DW trajectory calculated using Eq. (5.7). The parameters used are H_K=750 Oe, Δ=25 nm, α=0.01, β=0. The pinning potential is defined as V=2×10^4 erg/cm^3 and d=150 nm.

radius of the ellipse are expressed as

$$R_x^2 = \frac{2r^2}{p} \tag{5.8}$$

$$R_\psi^2 = \frac{r^2}{c} \tag{5.9}$$

where $r^2 = \frac{1}{2}c - v\psi_f + \frac{1}{2}px_f^2 - \left(-\frac{1}{2}px_0^2 + (a+\beta v)x_0 + \frac{1}{2}\cos 2\psi_0 - v\psi_0\right)$ and $c = \cos 2\psi_f$. The quantity in the big brackets represent the initial state, i.e. the state before the current pulse u (or v in the non-dimensional system) application. Here, $v_0 = \frac{u_0}{\omega_K \Delta}$, $x_0 = \frac{1}{p}(a_0 + \beta v_0)$ and $a_0 = \frac{\gamma H_0}{\omega_K}$, where u_0 and H_0 are the current and field applied before the current pulse. The red dotted line in Fig. 5.17 shows this analytical solution of the first spiral using the same parameters to numerically calculate the DW trajectory in Fig. 5.17. Since the damping is ignored in the analytical model, it overestimates the trajectory. Nevertheless, the agreement between the model and the calculation is sufficient to proceed.

Several mechanism of moving the DW out from the pinning potential well can be conceived. Here, three possible processes that can cause the depinning are shown. By tuning both magnetic field and current, it is possible to observe all three processes in the same pinning potential well. Figure 5.18 (a-c) show the three trajectories that result in depinning the DW. The black lines show the results of solving Eq. (5.1) and (5.2) numerically. The black solid lines show the DW trajectory during the current pulse, whereas the dashed line in (c) is the trajectory after the current is turned off. The red dotted lines are the expected first spirals calculated using Eq. (5.7). The three processes shown in Figure 5.18 (a-c) will be described below in this order.

5.5.2 Normal depinning

The first, and perhaps the most simple way to move the DW out from the potential well, or to depin the DW, is to expand the radius of the first spiral so that it reaches the boundary of the well. This is the process shown in Fig. 5.18 (a), where the sum of the first spiral radius and the fixed point position exceeds the boundary of the well. This criteria can be easily deduced graphically, i.e. $R_x + x_f > x_d$ from Eq. (5.7). Note that x_d is the non-dimensional representation of the width of the pinning potential ($x_d = \frac{d}{\Delta}$). Substituting terms from Eq. (5.3) and (5.8) gives the critical current v_c as

$$v_C = 2\beta(x_d - x_0)(-1 + \sqrt{1 - \frac{a + \beta v_0 - p(x_d + x_0)/2}{\beta^2(x_d - x_0)}}) + v_0 \tag{5.10}$$

We now need to define (x_0, ψ_0), the initial position and angle of the DW before the current pulse is turned on. When no magnetic field ($a_0 = 0$) or dc current ($v_0 = 0$) are applied before the current pulse, the initial conditions are $(x_0 = 0, \psi_0 = 0)$, according to Eq. (5.3) and (5.4). Substituting these values into Eq. (5.10) gives

$$v_C = 2\beta x_d(-1 + \sqrt{1 - \frac{a - p x_d/2}{\beta^2 x_d}}) \tag{5.11}$$

However, in the experimental setup, the magnetic field is usually turned on before the current pulse ($a_0 = a$). We ignore small dc currents applied throughout the experiment since they are small compared to the amplitude of the current pulse i.e. $v_0 \approx 0$. The initial condition becomes $(x_0, \psi_0) = (\frac{a}{p}, 0)$. Substituting these numbers

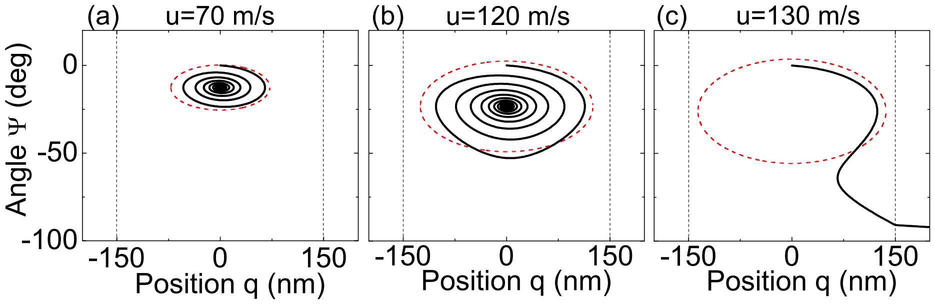

Figure 5.19: (a-c) Solid lines: Numerical calculations showing the phase space plot when listed values of current (u) are applied to show the bifurcation of the DW trajectory. No magnetic field is applied. Dotted red line: The first spiral of the DW trajectory calculated using Eq. (5.7). The parameters used are H_K=750 Oe, Δ=25 nm, α=0.01, β=0. The pinning potential is defined as V=2×10^4 erg/cm^3 and d=150 nm.

into Eq. (5.10) gives the expected experimental critical current

$$v_C = 2(x_d - \frac{a}{p})(-\beta + \sqrt{\beta^2 + \frac{p}{2}}) \tag{5.12}$$

which is linearly proportional to the magnetic field.

5.5.3 Bifurcation

When the current amplitude is increased to expand the radius of the spiral, the DW trajectory starts to deviated from an ellipse. Numerical solutions to Eq. (5.1) and (5.2) are shown in Figure 5.19 as black solid lines when the current is set to (a) u=70 m/s, (b) 120 m/s and (c) 130 m/s. No magnetic field is applied. The red dashed lines are the corresponding first spiral calculated using Eq. (5.7). As the current is increased, the trajectory at higher angles deviates from the ellipse. At the highest current (c), the trajectory completely changes its direction after reaching some high angle, i.e. the trajectory bifurcates.

In order to understand this behavior, it is useful to construct a phase portrait of the system. Figure 5.20 shows the phase portrait calculated using the parameters

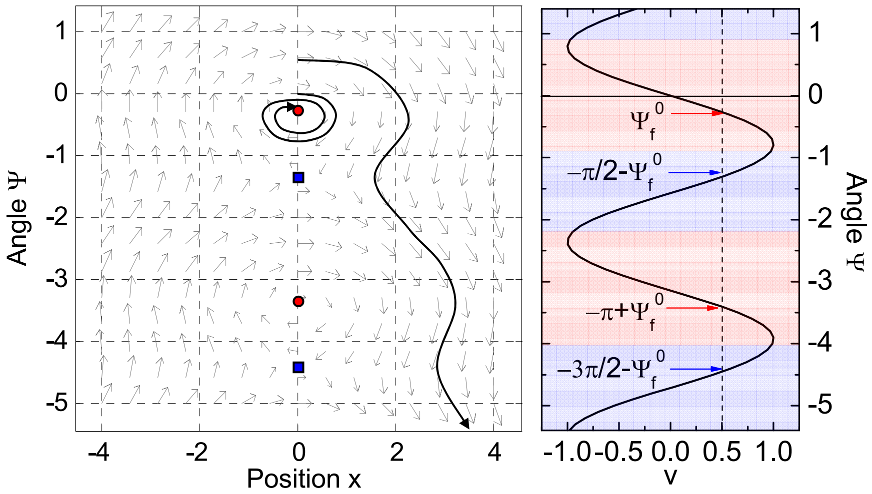

Figure 5.20: (a) Phase portrait of the differential equations (5.1) and (5.2). Arrows indicate the direction of trajectories. Parameters used are α=0.01, β=0, a=0, v=0.5, p=0.5. Two example trajectories are shown. Red circles and blue squares represent stable and unstable fixed points. (b) Graphical derivation of the stable and unstable fixed points, i.e. equation (5.4) is plotted. The intersections between the vertical dotted line and the solid sinusoid show the position of the fixed point. The background color represent the stability of the angle; red and blue correspond to stable and unstable ψ.

shown in the caption. The DW trajectory will follow the arrows once a ”point to pass” is determined.

We first seek the fixed points in the phase portrait. Since no magnetic field is applied and $\beta = 0$, $x_f = 0$ from Eq. (5.3). The values of ψ_f can be found from Eq. (5.4). Graphically, these solutions can be obtained by looking for the cross points of v and $-\sin(2\psi)$, which are plotted in Fig. 5.20 (b) for the same parameters used in (a). The colored arrows indicate the positions of ψ_f. Mathematically, the general solutions are expressed as $\psi_f = -\psi_f^0 + \frac{\pi}{2} \pm n\pi$ (blue arrows) and $\psi_f = \psi_f^0 \pm n\pi$ (red arrows). Here we define ψ_f^0 as the ψ_f that is closest to 0. The corresponding fixed points in the phase portrait are shown as colored circles.

Two exemplary trajectories are shown in black solid lines in Fig. 5.20 (a), where the points to pass are defined as $(0, 0)$ and $(0, 0.5)$. For the former case, the DW trajectory spirals and heads toward the center of the ellipse, or to one of the fixed points. This trajectory is similar to that shown in Fig. 5.17. On the other hand, when a different point $(0, 0.5)$ is chosen, the trajectory does not fall into the fixed points. It is rather repelled by a point represented by a blue square. This trajectory is similar to that observed in Fig. 5.19 (c).

The difference in the two trajectories is caused by the stability of the fixed point that each trajectory comes close by. In general, there are two types of fixed points, stable and unstable points. The stable and unstable fixed points determine the evolution of the DW trajectory. In order to distinguish the stability of the fixed points, we use the linear stability analysis. The characteristic equation of the two differential equations Eq. (5.1) and (5.2) is

$$\lambda^2 + \alpha(p + 2\cos 2\psi_f)\lambda + 2p(1+\alpha^2)\cos 2\psi_f = 0 \tag{5.13}$$

where λ is the eigenvalue of the characteristic equation. The solutions to the characteristic equation can be expressed as $\lambda = r \pm \sqrt{s}$ and the sign of r determines the stability. From Eq. (5.13), $r = -\alpha(p + 2\cos 2\psi_f)/2$. When r is negative (positive), the solution is stable (unstable). The stable (red) and unstable (blue) region of ψ_f are shown in Fig. 5.20 (b) as the background color. The stability of the fixed points in Fig. 5.20 (a) is also represented by the same color, i.e. the red points are the stable ones and the blue points are the unstable ones. Note that the trajectory in Fig. 5.20 (a) which do not fall into the stable point changes its direction to the next unstable point as it hits close to one of the unstable point. By doing so, interestingly, the amplitude of the position q of the trajectory also increases, which leads to depinning from the potential well, as seen in Fig. 5.19 (c).

The condition to cause this bifurcation of the DW trajectory can be estimated by assuming that the first spiral passes through the first unstable point. This is a very crude assumption because the analytical model of the first spiral assumes the angle ψ to be small, whereas for the bifurcation to occur, ψ must be large. Nevertheless, we proceed to obtain this condition. Form Fig. 5.20 (b), the closest unstable point is $(x_f, \psi_f) = (x_f, -\frac{\pi}{2} - \psi_f^0)$. Substituting these values into the first spiral Eq. (5.6) gives the critical current,

$$v_C = \frac{1}{1-2\beta^2/p}(\frac{2\beta}{p}A \mp \pi - v_0 \pm \sqrt{(\frac{2\beta}{p}A \mp \pi - v_0)^2 - (1-\frac{2\beta^2}{p})(4-\frac{2A^2}{p}-v_0^2)}) \tag{5.14}$$

where $A = a - a_0 - \beta v_0$. The $\mp$ sign stands for positive and negative critical current, respectively. As in normal depinning case, two different initial conditions are considered. We first take $(x_0 = 0, \psi_0 = 0)$, the case where no magnetic field or dc current is applied before the current pulse application. Substituting these values into Eq. (5.10) gives

$$v_C = \frac{1}{1-\frac{2\beta^2}{p}}\left(\mp\pi \pm \sqrt{(\frac{2\beta}{p}a \mp \pi)^2 - (1-\frac{2\beta^2}{p})(4-\frac{2a^2}{p})}\right) \tag{5.15}$$

When $(x_0, \psi_0) = (\frac{a}{p}, 0)$ is used, the case similar to the experimental setup, the critical current reads

$$v_C = \frac{1}{1-\frac{2\beta^2}{p}}\left(\mp\pi \pm \sqrt{\pi^2 - 4 + \frac{8\beta^2}{p}}\right) \tag{5.16}$$

which does not show any dependence on the magnetic field, i.e. v_C is constant.

The dependence of the bifurcation driven DW depinning on the current pulse length is not explicit in the formulas derived above. To clarify this dependence, Fig. 5.21 shows numerical calculations of the trajectories of a DW when a current pulse of (a) 100 ns and (b) 4 ns long are applied. Comparing the same current pulse amplitude, it is clear that when the current pulse is too short for the trajectory to reach the unstable fixed point, the DW does not depin. This can be seen in the trajectory when the amplitude is set to u=110 m/s, where it depins for 100 ns long pulse but not for the 4 ns long pulse.

5.5.4 Oscillatory depinning

The previous two sections described depinning of the DW during the current pulse application. We next study the last case where the depinning occurs after the current

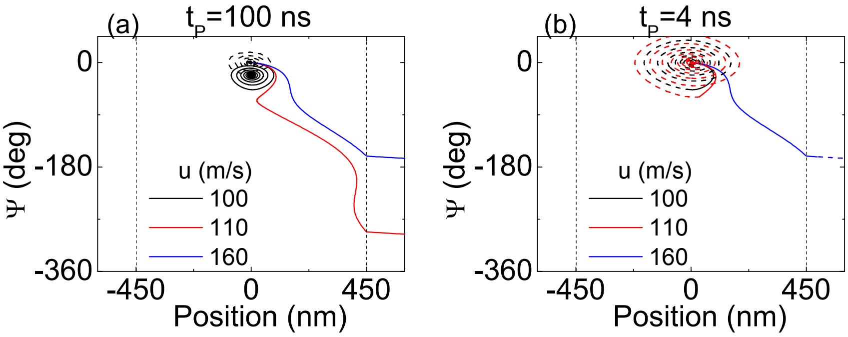

Figure 5.21: (a,b) Numerical calculations showing the phase space plot when (a) 100 ns and (b) 4 ns long current pulses are applied to show the pulse length dependent DW trajectory. No magnetic field is applied. The dotted lines are the DW trajectory after the current pulse is turned off. The parameters used are H_K=750 Oe, Δ=22 nm, α=0.01, β=0. The pinning potential is defined as V=2×10^4 erg/cm^3 and d=450 nm.

pulse is turned off, the case shown in Fig. 5.18 (c).

Interestingly, in this case, the depinning can become significantly sensitive to the current pulse length. Numerical solutions to Eq. (5.1) and (5.2) are shown in Figure 5.22 as black lines. The blakc solid and dashed lines represent the trajectory during and after the current pulse application,respectively. The amplitude of the current pulse is fixed to -90 m/s and the pulse length is varied; (a) 3.5 ns, (b) 7.0 ns and (c) 10.5 ns. A small magnetic field of 8 Oe is applied. For (a) and (c), the DW exits the pinning potential well after the current pulse is turned off. For (b), the DW stays in the well during and after the current pulse.

We first use the analytical form of closed ellipse Eq. (5.7), i.e. the first spiral, to understand this phenomena. The red dashed lines in Fig. 5.22 (a-c) show the first spiral, calculated using Eq. (5.7), when the current ($u = -90 m/s$) is applied. As evident from this first spiral, the DW will not exit the well during the current pulse application since the edge of the first spiral does not reach the boundary of the well. However, when the current pulse is turned off at the proper timing, it is possible to increase the radius of the ellipse after the current pulse. This is illustrated by the green dashed lines in Fig. 5.22 (a-c), which represent the first spiral after the current

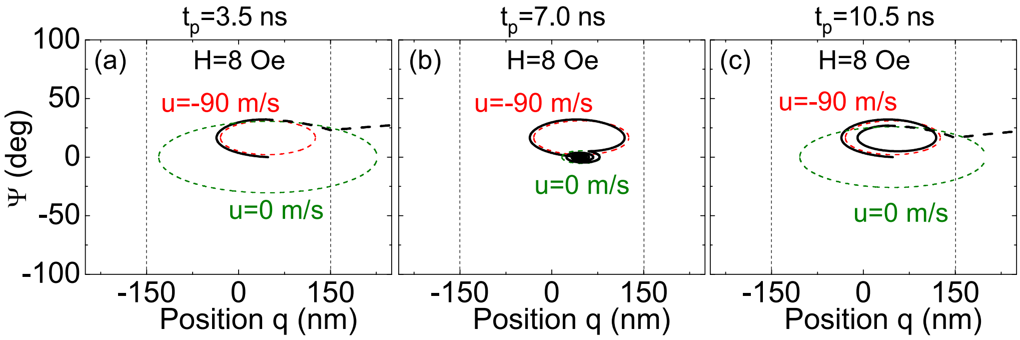

Figure 5.22: (a-c) Solid lines: Numerical calculations showing the phase space plot when a current pulse (u=-90 m/s) is applied for (a) 3.5 ns, (b) 7.0 ns and (c) 10.5 ns. Magnetic field is set to 8 Oe. The dashed black lines represent the trajectory of the DW after the current pulse is turned off. Dotted red line: The first spiral of the DW trajectory calculated using Eq. (5.7) when the current is on. Dotted green line: The first spiral of the DW trajectory calculated using Eq. (5.7) when the current is off. The parameters used are H_K=750 Oe, Δ=25 nm, α=0.01, β=0. The pinning potential is defined as V=2×10^4 erg/cm^3 and d=150 nm.

pulse.

These first spirals are calculated from Eq. (5.7) using the following procedure. The point (x,ψ) when the current pulse is turned off is taken from the numerical calculation and substituted into Eq. (5.7) as (x_0,ψ_0). Since the current is turned off, the new center of ellipse, or the new fixed point becomes (x_0,0). Note that the magnetic field is still turned on after the current pulse.

For the cases shown in Fig. 5.22 (a) and (c), it is clear that the edge of the new first spiral exceeds the boundary of the well, allowing the DW to exit. Note that the radius of new ellipse shrinks when the DW undergoes two rotations before the current is turned off due to damping; compare the radius of the green dashed lines for (a) and (c). The radius of the new first spiral depends on when the angle ψ_{OFF} when the current pulse is turned off. The bigger the ψ_{OFF}, the larger the radius of the new ellipse. The case when ψ_{OFF} is small is shown in Fig. 5.22 (b), where no depinning occurs.

In order to estimate the pulse length that can cause the depinning, we must obtain an analytical formula of the first spiral that includes the time dependence. However, the expression of the first spiral in Eq. (5.7) does not contain any time dependence. Therefore, we use a different approach to obtain the time dependence.

As shown in Fig. 5.18 (c), the angle ψ does not have to be large compared to the bifurcation regime. Thusthe two differential equations Eqs. (5.1) and (5.2) can be linearized assuming $\psi << 1$. The non-linear terms in Eqs. (5.1) and (5.2) are expanded around ψ_f to obtain the linearized differential equations

$$(1+\alpha^2)\dot{x} = \alpha(a - px + \beta v) + 2c(\psi - \psi_f) \tag{5.17}$$

$$(1+\alpha^2)\dot{\psi} = (a - px + \beta v) - 2\alpha c(\psi - \psi_f) \tag{5.18}$$

where $c = \cos(2\psi_f)$. Linearization of the differential equations allows separation of variables, x and ψ. Rearranging Eqs. (5.17) and (5.18) leads to two second order ordinary differential equations

$$(1+\alpha^2)\ddot{x} + \alpha(2c+p)\dot{x} + 2cpx = 2cpx_f \tag{5.19}$$

$$(1+\alpha^2)\ddot{\psi} + \alpha(2c+p)\dot{\psi} + 2cp\psi = 2cp\psi_f \tag{5.20}$$

These differential equations are similar to those of damped harmonic oscillators and can be directly solved. The initial conditions are assumed as,

$$x(0) = x_0 \tag{5.21}$$

$$\psi(0) = \psi_0. \tag{5.22}$$

Substituting these initial conditions into Eqs. (5.17) and (5.18) gives the second set of initial conditions,

$$\dot{x}(0) = \frac{1}{1+\alpha^2}\left[\alpha(a - px_0 + \beta v) + 2c(\psi_0 - \psi_f)\right] \tag{5.23}$$

$$\dot{\psi}(0) = \frac{1}{1+\alpha^2}\left[(a - px_0 + \beta v) - 2\alpha c(\psi_0 - \psi_f)\right] \tag{5.24}$$

The solutions to Eqs. (5.17) and (5.18) are obtained by substituting the above

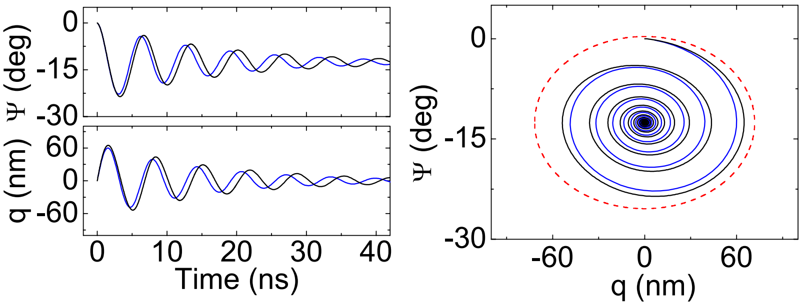

Figure 5.23: Comparison of the analytical solution from Eq. (5.25) and (5.26) (blue) to the numerical calculated position (a) and angle (b) of a DW. The reconstructed phase space plot are shown in (c) with the analytical first spiral equation (Eq. (5.7) shown as the red dotted line. The parameters used are H_K=750 Oe, Δ=25 nm, α=0.01, β=0. The pinning potential is defined as V=2×10^4 erg/cm^3 and d=150 nm.

initial conditions and reads

$$x(\tau) = x_f + \left[(x_0 - x_f)(\cos\omega\tau + \frac{\kappa}{\omega}\sin\omega\tau) + \frac{S_x}{\omega}\sin\omega\tau\right]\exp(-\kappa\tau) \tag{5.25}$$

$$\psi(\tau) = \psi_f + \left[(\psi_0 - \psi_f)(\cos\omega\tau + \frac{\kappa}{\omega}\sin\omega\tau) + \frac{S_\psi}{\omega}\sin\omega\tau\right]\exp(-\kappa\tau) \tag{5.26}$$

where, $\kappa \equiv \alpha(1+\frac{p}{2})$, $\omega \equiv \sqrt{2p}$, $S_x \equiv \dot{x}(0) = \frac{1}{1+\alpha^2}\left[\alpha(a - px_0 + \beta v) + 2c(\psi_0 - \psi_f)\right]$ and $S_\psi \equiv \dot{\psi}(0) = \frac{1}{1+\alpha^2}\left[(a - px_0 + \beta v) + 2c\alpha(\psi_0 - \psi_f)\right]$. As always, $c = \cos(2\psi_f)$ and x_f and ψ_f are defined in Eqs. (5.3) and (5.4), respectively.

The blue solid lines in Fig. 5.23 (a) show the temporal evolution of the position and angle of the DW calculated from Eqs. (5.25) and (5.26), respectively. The black lines represent numerical calculation results. The analytical solutions agree well with the numerical results for the first few oscillations. The phase space plots are shown in Fig. 5.23 (b), where the analytical solutions and the numerical calculations are shown in blue and black solid lines, respectively. The red dashed line is the analytical formula of the closed ellipse from Eq. (5.7).

As can be seen in Fig. 5.23 (a), the position q and angle ψ oscillates with the same frequency but are 90 degree out of phase. From Eqs. (5.25) and (5.26), the oscillation period τ_{osc} is

$$\tau_{osc} \equiv \frac{2\pi}{\omega} = \frac{2\pi}{\sqrt{2p}} \tag{5.27}$$

It is also interesting to note that the decay rate of the radius of the spiral is determined by κ. The decay time τ_{decay} is thus given as

$$\tau_{decay} \equiv \frac{1}{\kappa} = \frac{1}{\alpha(1+p/2)}, \tag{5.28}$$

which is inversely proportional to the Gilbert damping constant.

Finally, in order to illustrate the three regimes, normal depinning, bifurcation and oscillatory pulse length dependence, numerical calculation results are shown. Figure 5.24 show the calculated depinning probability maps (in this case, the probability is either one (red) or zero (blue)) when (a) 100 ns and (b) 4 ns long current pulses are used. The parameters used are to fit the data of the T_C and V_C walls in 300 nm wide nanowires whose data are shown in Fig. 5.9 (e) and (f), respectively.

To illustrate the depinning process, selected trajectories are shown in Fig. 5.24 (c) and (d), where the dotted lines correspond to the trajectories after the current pulse is turned off. The trajectories are shown for fields and currents where cross points are marked in (a) and (b). From the trajectories, it is clear that the depinning process is different at high field and low field. At low fields, bifurcation induced depinning occurs for both 100 ns and 4 ns long current pulses. However, at high fields, normal depinning occurs for the 100 ns long pulse case, whereas depinning occurs after the current pulse is turned off for the 4 ns long pulse case, which is representative of the oscillatory depinning regime. It is also clear that in the oscillatory depinning regime, the current to observe depinning is lower than the critical current for either normal or bifurcation induced depinning.

The black solid lines in Fig. 5.24 (a) and (b) are the analytical solutions of the critical current (u_C) derived from Eq. (5.11) and Eq. (5.15). The two equations for the critical current v_C are compared and the one with lower v_C is plotted. At higher fields, normal depinning has lower v_C, where as at lower fields, bifurcation induced depinning has lower v_C. The crossover from normal to bifurcation induced depinning occurs at ±42 Oe. When the current pulse length is 100 ns (a), the analytical solutions

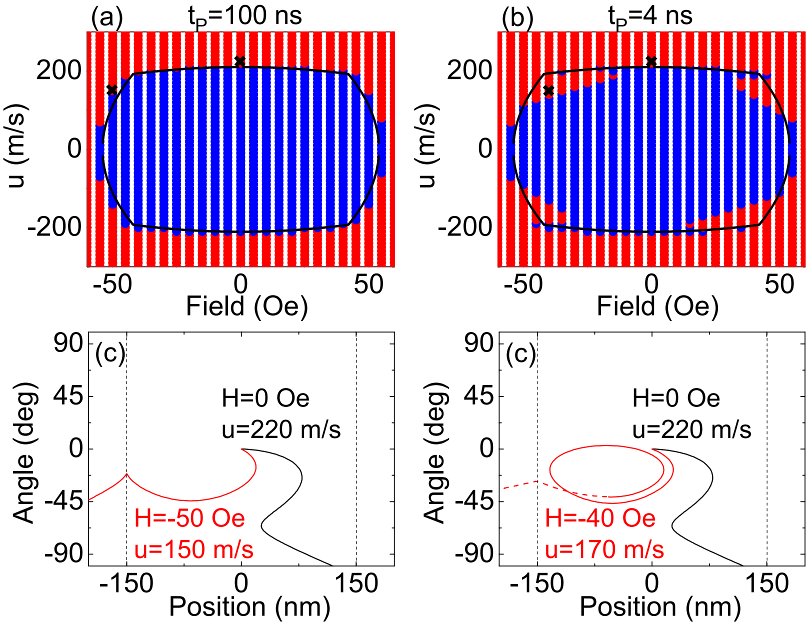

Figure 5.24: Numerically calculated depinning probabilities maps (red corresponds to one, blue corresponds to zero), plotted against the current (u) and magnetic field. The current pulse lengths are set to (a) 100 ns and (b) 4 ns. The black solid lines are the analytical solutions of the critical current (u_C) derived from Eq. (5.11) and Eq. (5.15). At ±42 Oe, the depinning mechanism changes: bifurcation induced depinning occurs at low field whereas normal depinning occurs at high field. The parameters used are to fit the data shown in Fig. 5.9 (a) and (c): H_K=950 Oe, Δ=35 nm, α=0.01, β=0. The pinning potential is defined as V=8.64×10^4 erg/cm^3 and d=150 nm.

agree well with the numerically calculated solutions. The discrepancy between the analytical solutions and the numerical calculations for the 4 ns long pulse case is due the oscillatory depinning occurring at high fields.

5.5.5 Comparison with experiments

Experimental results obtained in the previous sections are now compared with the 1D model. First the field dependence of the critical current densities are compared to that expected from the analytical solutions Eq. (5.11) and Eq. (5.15). The solid lines in Fig. 5.9 and 5.10 show the best fit to the data using the parameter shown in Table 5.3.

The fitting parameters used are H_K, β and d. The potential depth V is determined from the zero current depinning field, $V = 2H_{DP}M_S$. The DW width Δ is set to the values obtained from micromagnetic simulations (see Chapter 2.4 and Fig. 2.4) and H_K is used as one of the fitting parameters. In the fitting process, H_K and Δ determines the critical current near zero field, i.e. the bifurcation regime, whereas d and β determines the crossover from bifurcation induced to normal depinning.

Although the fitting seems to work fairly well, the parameters obtained from the fitting shows some limit of applying 1D model to a system where significant heating is occurring. The H_K values of the vortex walls seem too high, whereas that of the transverse walls are too small compared to what is expected from micromagnetic simulations (see Fig. 2.4). The values of β are in reasonable range compared to those obtained in other experiments. On the other hand, the pinning potential width d becomes too large when the wire width is decreased. In addition to Joule heating, DW transformation also contributes to the depinning process, which is not included in the model, which may account for some of the discrepancy.

The dependence of the critical current at the zero field on the current pulse length, shown in Fig. 5.11 (a), is compared to the 1D model using numerical methods. As shown in Fig. 5.21, the bifurcation induced depinning is suppressed when the current pulse length is too short. Numerical calculations are performed to calculate the pulse length dependence of the critical current at zero field. In order to avoid

w (nm)	state	H_{DP}^+	H_{DP}^-	H_K (Oe)	Δ (nm)	V^+ (erg/cm^3)	V^- (erg/cm^3)	d (nm)	β
300	T_C	-54	54	900	36	86400	86400	150	0.01
	T_A	-41	119	900	36	65600	190400	250	0.01
	V_C	-51	49	1550	22	81600	78400	350	0.01
	V_A	-20	120	1550	22	32000	192000	250	0.01
200	T_C	-48	45	1200	30	76800	72000	300	0.004
	T_A	-32	70	1200	30	51200	112000	350	0.004
100	T_C	-19	7	1500	23	30400	11200	400	0.001

Table 5.3: Parameters obtained from fitting the analytical critical currents (Eqs. (5.11) and (5.15)) to experimental data.

other depinning process to take place, either normal or oscillatory depinning, a large pinning potential width is used (d=450 nm). Figure 5.25 shows the minimum u needed to cause bifurcation induced depinning, or u_C, plotted against the current pulse length using parameters for (a) transverse wall and (b) vortex wall in a 300 nm wide nanowire. The parameters are shown in the caption. The insets show plots of the inverse of pulse length against u_C. The current density J_C is converted from u_C using the relationship $J = \frac{eMu}{\mu_B P}$, where e is the electron charge, M is the magnetization (800 Oe), μ_B is the Bohr magnetron and P is the spin polarization of the current. P is set to one for simplicity. The trend agrees with the experimental results.

The dependence of the critical current on the depth of the pinning potential V is plotted in Fig. 5.26 for a 100 ns long current pulse. The parameters used are the same as those in Fig. 5.25 (b). The corresponding zero current depinning fields are plotted in the top axis. When the potential depth is small (H_{DP} up to ~10 Oe), the critical current scales linearly with potential depth. However, for deeper potential wells, surprisingly, the critical current shows almost no dependence on the well depth[94]. This is consistent with the experimental results shown in Fig. 5.11 (b). Note that pure thermal activation switching cannot explain the results shown in Fig. 5.11 (b). However, since the energy barrier of the system, dominated by the demag energy of the DW located at the nothc, is also temperature dependent, it is diffuclt to apply Ahrenius law to discuss these results using thermal activated switching.

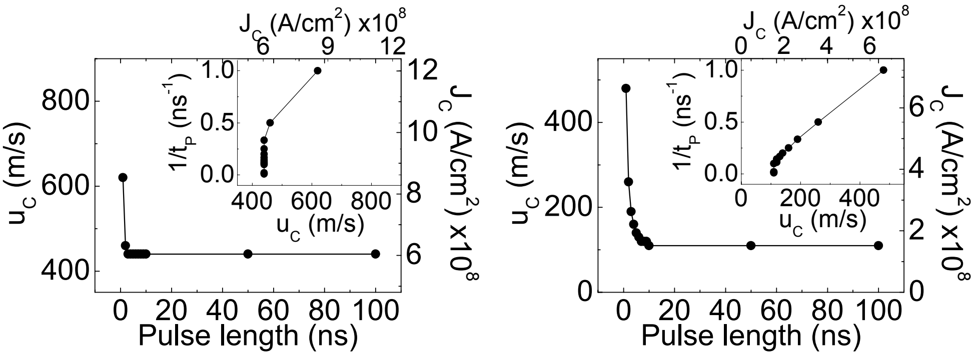

Figure 5.25: Numerically calculated critical current J_C, or u_C, plotted against the current pulse length using parameters for (a) transverse wall and (b) vortex wall in a 300 nm wide nanowire: (a) H_K=1800 Oe, Δ=36 nm, (b) H_K=750 Oe, Δ=22 nm. The pinning potential is defined as V=8×10^4 erg/cm^3 and q_0=450 nm. α=0.01, β=0. The insets show plots of the inverse of pulse length against u_C.

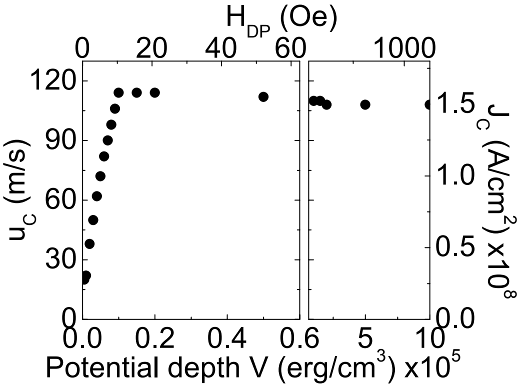

Figure 5.26: Numerically calculated critical current J_C, or u_C, plotted against the depth of the pinning potential depth V. 100 ns long current pulse is used to study the depinning. Parameters used are H_K=750 Oe, Δ=22 nm, d=450 nm, α=0.01 and β=0.

5.6 Observation of oscillatory depinning

5.6.1 Pulse amplitude dependence

Finally, the oscillatory depinning and transformation probability observed in the experiments, as was shown in Fig. 5.15 (a) and (b) for a V_C wall, are discussed. The oscillation of the depinning probability was first surprising; the DW leaves the pinning center when a short current pulse is applied but remains there when a longer current pulse is applied. This suggested the possibility that the DW is depinned from the pinning center after the current pulse is turned off. Later, the one-dimensional (1D) model revealed the mechanism of this phenomena[75], which conversely proved the importance of the 1D model. In this section, we investigate these oscillatory behaviors in detail and compare the results to the calculations from the 1D model.

Data shown are from a 300 nm wide permalloy nanowire with a triangularly shaped notch located 2 μm away from contact line A. The notch depth is ~30% of the wire width. Figure 5.27 (a) shows the depinning probability map plotted as a function of the amplitude and length of the voltage pulse. The initial DW structure is a head to head V_A wall and the applied magnetic field is -12 Oe. Note that the zero current depinning field is -20 Oe and 120 Oe (see Table 5.2) for this DW. An MFM image of the V_A wall is shown at the top of the figure for reference. The magnetization configuration and the applied field direction are shown in the image by white and black arrows, respectively. The depinning probability oscillates with the pulse length when a positive voltage is applied. Depinning of the wall is observed when the pulse voltage is higher than ~0.8 V. On the other hand, for negative voltages, the depinning probability shows little dependence on the pulse length. Depinning is only observed when the magnitude of the voltage pulse is larger than ~-1.1 V.

These results can be reproduced by numerically solving the two differential equations in the 1D model of the DW. Fig. 5.27 (b) shows the depinning probability from the 1D model using the parameter shown in the caption. The parameters are obtained by the following method. The anisotropy field H_K and the DW width Δ are estimated by micromagnetic simulations, as discussed in chapter 2.4 (see Fig. 2.4). For a 300 nm wide nanowire, H_K=750 Oe and Δ=23 nm. The pinning potential depth

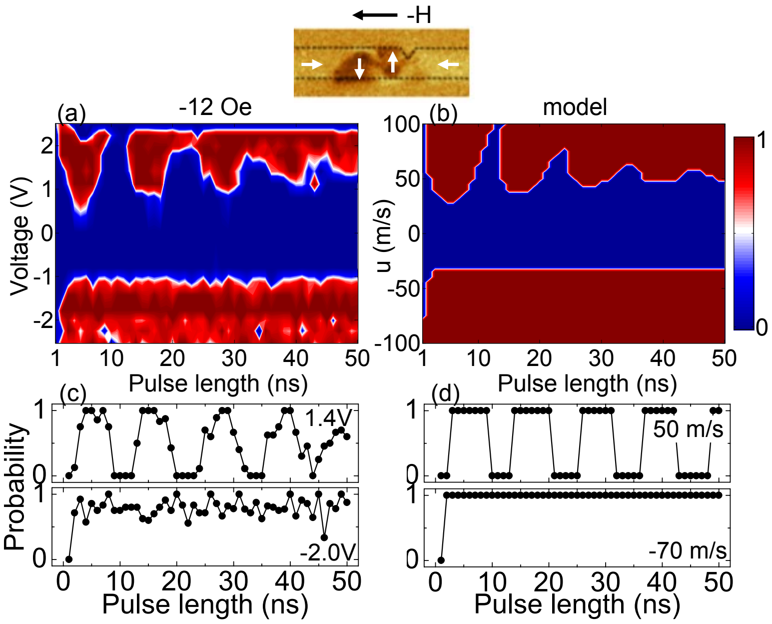

Figure 5.27: (a) Depinning probability map of a HH V$_A$ wall plotted against amplitude and length of the voltage pulse at a fixed field of -12 Oe. The color scale bar shown in the far right represents the probability. MFM image of the V$_A$ wall is shown on top. (b) Calculated depinning probability map using the 1D model. (c,d) Depinning probability as a function of a pulse length at fixed field (-12 Oe) and fixed voltage (see insets) for experiment (c) and calculation (d). Parameters used in the calculations are H_K=750 Oe, Δ=23 nm, V_{pin}=16000 erg/cm^3, $d = 320$ nm, $\alpha = 0.008$ and $\beta = 0.020$. H=-15 Oe is applied to mimic the experimental setup.

V_{pin} is estimated from the experimentally obtained zero current depinning field H_{DP} through the relationship $V_{pin} = H_{DP}M_S$. Since a negative magnetic field is applied in this case (H_B=-12 Oe), we take the zero current depinning field $H_{DP}^- = -20$ Oe. The potential depth V_{pin} equals 16000 erg/cm^3, assuming $M_S = 800$ emu/cm^3. The width of the notch potential d is then estimated using Eq. 5.27, or $t_{osc} = \frac{\pi}{\gamma}\sqrt{\frac{V_{pin}\Delta H_K}{Mq_0}}$ and substituting the experimentally obtained oscillation period t_{osc}. $d = 320$ nm is obtained from the data. These parameters are used to fit the experimental data with the fitting parameters being α and β. A magnetic field of -15 Oe is applied to mimic the experimental setup. Best fits are obtained when $\alpha = 0.008$ and $\beta = 0.020$. See Ref. [118, 126] for measured damping constant in permalloy films. For clarity, the depinning probabilities at fixed currents (u) are shown in Fig. 5.27 for experiments (c) and calculations (d).

Excellent agreement is obtained between the experiment and the calculation. It is interesting to note that the current direction that causes the depinning in the oscillatory regime is opposite to what is expected from the spin transfer torque theory. Since the field is applied in the -x direction, it is expected that electron flowing in the -x direction (negative pulse voltages) will assist the depinning process through spin transfer torque. However, the electron flow that exhibits the oscillation of the depinning probability is in the +x direction (positive voltage), which pushes the wall in the +x direction. Moreover, the minimum pulse amplitude needed to depin the DW is lower for the positive voltages (0.8 V) than the negative voltages (-1.1V). The fact that the DW is depinned from the notch with lower positive voltage pulse also supports that the depinning occurs after the pulse.

Fig. 5.28 (a) show the field dependence of the depinning probability plotted as a function of pulse length at fixed voltages. For negative voltage, the depinning probability abruptly changes from zero to one when the pulse length exceeds a certain duration (termed t_P^*, hereafter). Above t_P^*, the depinning probability is nearly independent of the pulse length. When the field magnitude is increased, t_P^* tends to decrease, which is the characteristics of the normal depinning. By contrast, for positive voltage, the average depinning probability changes from zero to one when the magnitude of the field is increased. Oscillations of the depinning probability are

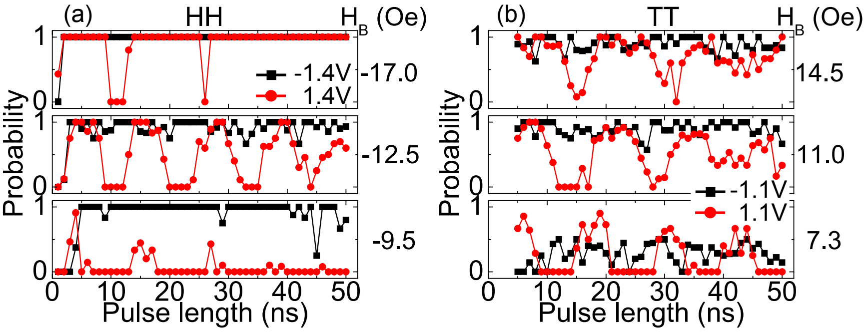

Figure 5.28: Field dependence of the depinning probability as a function of a pulse length at fixed voltages (see insets) for (a) HH and (b) TT T_A wall.

observed in this field range, however, the period tends to increase when the field magnitude is increased.

To show that the these oscillations are not deriving from the self field from the current pulse, results from the tail to tail (TT) V_A wall are shown in Fig. 5.28 (b). The applied field is positive in this case, opposite to that in Fig. 5.28 (a). This is to match the direction the field pushes the DW (-x in Fig. 5.1) for both HH and TT walls. As evident from Fig. 5.28, the depinning probability oscillates with pulse length only when the voltage pulse polarity is positive for both wall types. Thus it is likely that the self field plays little role in this process. In addition, for the TT wall, the dependence of the oscillation period on the applied field is more pronounced.

5.6.2 DC current dependence

Up to this point, the effect of the small dc probe current was neglected. It can be expected that the depinning probability may change, through spin transfer torque, when this dc current is increased. The depinning probability of the HH V_A wall is plotted in Fig. 5.29 (a) as a function of pulse length with different dc current levels. The voltage pulse amplitude is fixed to 1.1 V and the applied magnetic field is -12 Oe. Note that all of the previous experiments used 0.1 mA of dc current.

In Fig. 5.29 (a), at the lowest dc current, there is little effect on the depinning probability when the current direction is reversed. However, as the current amplitude is increased, the effect becomes significant. For negative dc currents, oscillations in depinning probabilities are observed at all current amplitudes. The oscillation period shows little dependence on the current amplitude. In addition, the long pulse limit of the depinning probability seems to increase as the dc current amplitude is increased. By contrast, for the positive dc currents, the depinning probability is nearly suppressed to zero at higher currents. Since the dc current flows in the same direction as with the current from the voltage pulse, it surprising that the depinning probability diminishes at higher current, since the total current will be higher. Note that the current that flows into the nanowire when a ±1.1 V voltage pulse is injected into the nanowire is, without the Joule heating effect, $\sim \pm 3.8$ mA.

Numerical calculations using the 1D model can reproduce these results. Fig. 5.29 (b) shows the calculation results using the same parameter set used in calculating Fig. 5.27 (b). The agreement between the experiment and calculation is fairly good. From these calculations, the spin polarization of the current can be deduced, which is estimated to be $P \sim 0.4$. The size of the spin polarization of the current in ferromagnetic materials is still under debate[127, 104, 128].

5.6.3 Reflection from the pinning potential

Oscillations of the depinning probability are also observed for the V_C walls. Figure 5.30 show maps of the depinning probability of HH V_C wall plotted as a function of the amplitude and length of the voltage pulse. The applied fields are (a) -42 Oe and (b) 49 Oe. The zero current depinning fields are -45 Oe and 54 Oe (see Table 5.2). Oscillations of the depinning probabilities are observed, however, for the current direction opposite to the what was observed in the V_A wall. For example, when a negative field is applied, oscillations of the depinning probability are observed in the positive voltages for the V_A wall (Fig. 5.27 (a)), whereas the oscillations are observed in the negative voltages for the V_C wall (Fig. 5.30 (a)). In fact for the V_C wall, oscillations of the depinning probability are seen in the current direction where the electron flow is in the same direction with the pressure from the field on the DW,

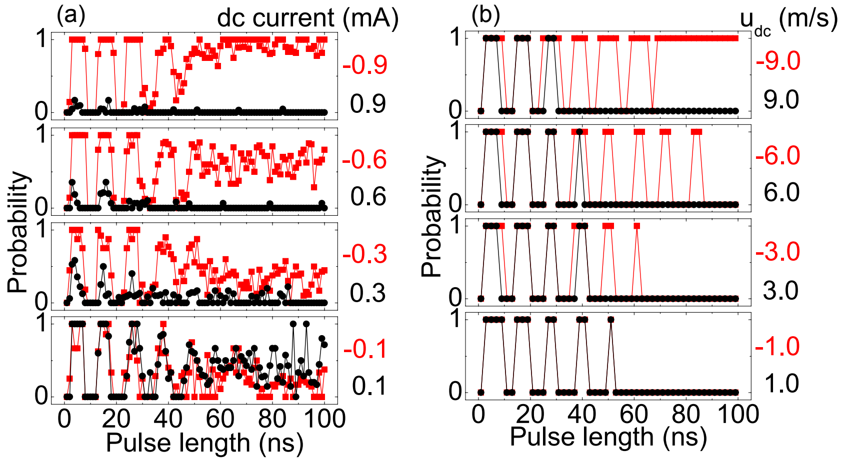

Figure 5.29: (a) Depinning probability of a HH T$_A$ wall plotted against the pulse length at selected dc currents. The values of the dc current are listed on the right. The amplitude of the voltage pulse is fixed to 1.1 V. (b) Calculated dc current (u_{dc}) dependence of the depinning probability. Parameters used in the calculations are H_K=750 Oe, Δ=23 nm, V_{pin}=16000 erg/cm^3, $d = 320$ nm, $\alpha = 0.008$ and $\beta = 0.020$. The amplitude of the current pulse is fixed at $u = 48$ m/s. H=-15 Oe and are applied to mimic the experimental setup.

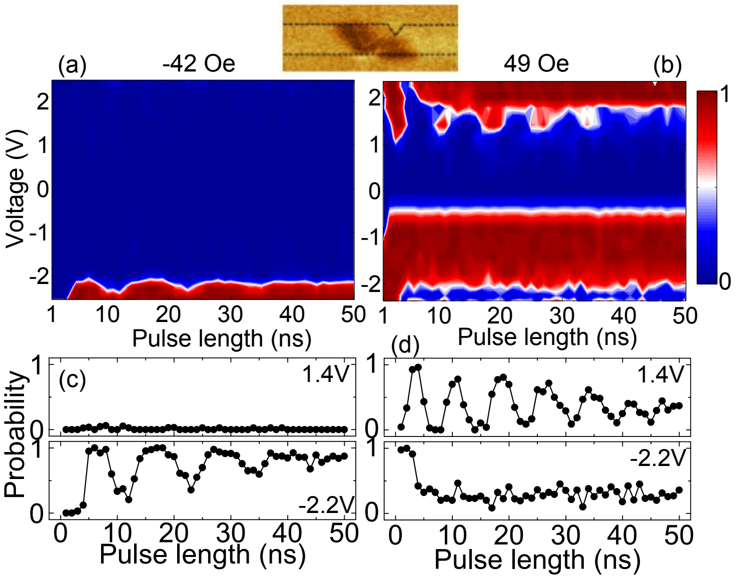

Figure 5.30: Top panels: Depinning probability map of a HH V_C wall plotted against amplitude and length of the voltage pulse at a fixed field of (a) -44 Oe and (b) 46 Oe. MFM image of the V_C wall is shown on top. Bottom panels: Corresponding cross section of the depinning probability as a function of a pulse length at fixed voltages (see insets).

which is not expected from the 1D model.

We now discuss the origin of the oscillatory depinning observed when the current pulse is applied in the ”wrong” direction. First the trajectory of the DW is calculated by numerically solving Eqs. (5.1) and (5.2). The colored solid lines in Fig. 5.30 (a) and (b) show the trajectories of the motion of (a) V_A wall and (b) V_C wall when a current of (a) u=30 m/s and (b) u=-22 m/s applied. Magnetic fields of (a) -15 Oe and (b) -50 Oe are applied to match the experimental condition. Colored dashed lines show the trajectory after the current pulse is turned off at (a) 5 ns and (b) 3.5 ns. The parameters of the V_C wall are estimated using the same method described above and are listed in the caption. The vertical dotted line represents one edge of the potential well; the other edge is not shown.

The DW trajectory after the current pulse shown in Fig. 5.30 (a) is the ”normal” oscillatory depinning, as described in Section5.5. The size of the DW trajectory is

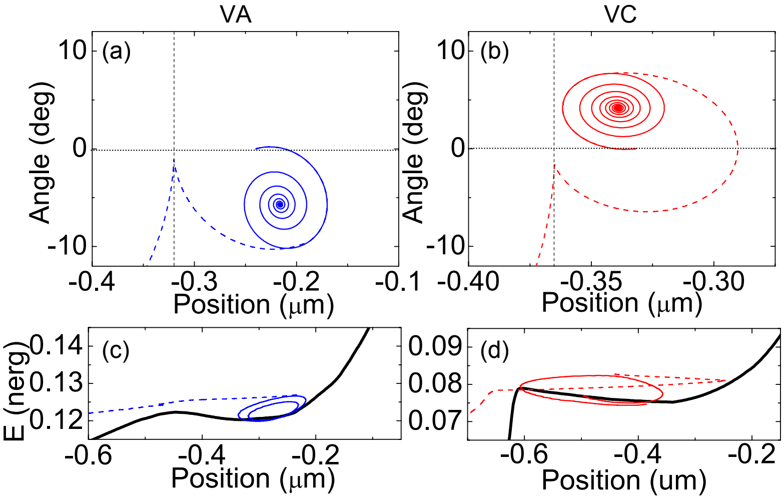

Figure 5.31: (a,b) DW trajectory calculated using the 1D model for (a) V$_A$ wall ($V = 1.6 \times 10^4$ erg/cm^3, d=320 nm) and (b) V$_C$ wall ($V = 4.4 \times 10^4$ erg/cm^3, d=365 nm). Parameters used for these vortex walls are H_K=750 Oe, Δ=23 nm, α=0.008 and β=0.020. Magnetic fields of (a) -15 Oe and (b) -50 Oe are applied. The amplitude and length of the current pulse are (a) 30 m/s, 5 ns and (b) -22 m/s, 3.5 ns. The dashed lines represent the trajectories after the current pulse is turned off. The vertical dotted line shows one edge of the pining potential. (c,d) DW trajectory (total energy) calculated using micromagnetic simulation for (c) V$_A$ wall and (d) V$_C$ wall. The thick black line shows the potential well provided from the notch. For all panels, the colored and black lines represent the trajectory during and after the current pulse, respectively.

amplified after the current pulse, owing to the extra momentum it possesses when the pulse is turned off, and thereby enabling the depinning process. The DW trajectory shown in Fig. 5.30 (b) explains the oscillatory depinning on the pulse length for the "opposite" current direction. After the current pulse is turned off, the trajectory undergoes half more cycle to depin the DW, compared to the "normal" depinning case.

The criterions of seeing this effect are: (1) DW trajectory during the current pulse should not exceed the edge of the pinning potential and (2) the DW should posses enough momentum when the pulse is turned off so that it can reach the edge of the potential after half more cycle. Note that since magnetic field is applied, the pinning potential is tilted for both cases, and thus the DW will never depin from the right edge of the well.

Micromagnetic simulations are performed to illustrate this effect more intuitively. The solid black lines in Fig. 5.31 (c) and (d) show the energy profile of the notch pinning potential, $E = \sigma w t + V_{sys} M_X H_X$. σ is taken from Fig. 5.4 (c) and (d). M_X is the x-component of the magnetization and V_{sys} is the total volume of the system (see Section 5.2 for details). Magnetic fields H_X of (c) -15 Oe and (d) -53 Oe are applied to mimic the experimental setup of Fig. 5.27 (a) and Fig. 5.30 (a), respectively. Note that the applied magnetic field tilts the potential energy profile.

In the simulation, we first place the DW in interest at the notch and apply the magnetic field. After the system reaches an equilibrium, zero rise-time step-function like current of (c) 1.5 mA and (d) -2.0 mA are applied. The energy of the system $E(t) = E_{TOT}(t) + E_0$ during the current application are plotted in colored lines. The trajectory of the energy undergoes a elliptical motion within the well and heads toward the center of this ellipse due to Gilbert damping. Note that since the current direction is opposite in Fig. 5.31 (c) and (d), the sense of rotation of the trajectory is opposite; it is counter-clockwise in (c) and clockwise in (d). The dashed line shows the energy of the system after the current is turned off to zero at (c) 15.4 ns and (d) 4.7 ns.

In Fig. 5.31 (c), the DW heads toward the left side of the potential after the current is turned off and consequently exits the well. This process illustrates that the

DW indeed move after the current is turned off. The DW can depin when its energy level is higher than the local energy barrier located at the edge of the potential well. The energy the DW possesses when it passes through the local energy barrier depends on the energy it has when the current pulse is turned off. Depinning occurs for every half cycles when the DW has high enough energy when the current pulse is turned off, leading to the oscillation of the depinning probability.

By contrast, in Fig. 5.31 (d), when the current is turned off at the highest energy point, the DW heads toward the right side of the well. Note that the DW undergoes a clockwise rotation during the current application in this case. When the DW hits the right edge of the well, it bounces back into the well and heads toward the left side of the wall. Note also that because of the applied magnetic field, the potential well is asymmetric. When the DW has high enough energy to overcome the local energy barrier at the left edge of the well, it can exit the well. The energy at this point also depends on the energy when the current is cut off.

It is not clear yet why the V_C wall is the one that shows the oscillation of the depinning probability in the "opposite" current direction. We infer that the energy landscape of the potential well of this wall is suited to cause this effect. Other factors that are left out here but must be taken into account are the direction of the vortex core polarity and the effect of the self fields from the current pulses.

5.6.4 Magnetic field dependence

Finally, we discuss the origin of the various oscillation periods observed both in depinning and transformation and in the two wall states V_A and V_C. In Fig. 5.32, all oscillation periods observed, both in the depinning (blue squares) and in the transformation (red circles) probability, for (a) V_A wall and in (b) V_C wall are shown and plotted as a function of the applied magnetic field H_B. The oscillation periods depends on the magnetic field.

The periods of DW undergoing one cycle in the well are calculated using micromagnetic simulations. First a DW is placed at the notch and magnetic field is applied. Then a small current is applied ($\pm 500\mu$A) to excite the DW. The current is set as small as possible (500 μA) to avoid non-linear effects at higher currents. As the current is applied, the position of the DW oscillates within the well. For both vortex walls V$_A$ and V$_C$, the excitation of the DW are studied for the two core polarities, up and down. Experimentally, the core polarity is an unknown parameter. At each field, the periods of the vortex wall with two core polarities and both current directions are obtained and are all showed together as solid diamonds in Fig. 5.32. Since the notch breaks the one dimensional symmetry, the oscillation periods are not the same for the core polarities and for the current directions. The agreement between the experimental results and the simulations is fairly good.

The inset of Fig. 5.32 (a) shows the oscillation periods of the transformation probability of the V$_A$ wall plotted as a function of the pulse voltage. At higher currents, the period increases. This is presumably due to the amplification of the trajectory at higher current amplitudes, which increases the cycle time.

The solid line represents the estimated oscillation period calculated from the 1D model and the DW potential energy landscape E shown in Fig. 5.4 (c) and (d). The oscillation period can be derived using the relationship derived in Eq. (5.27). Equation (5.27) can be rewritten to incorporate the pinning potential profile dependence of the oscillation period,

$$t_{osc}(q) = \frac{2\pi}{\gamma}\sqrt{\frac{2M_S}{H_K\Delta}\left(\frac{\partial^2\sigma}{\partial q^2}\right)^{-1}}. \tag{5.29}$$

The values of H_K and Δ are taken from the Fig. 2.4. The second derivatives of σ (shown in Fig. 5.4 (c) and (d)) with respect to the position of the DW are calculated and substituted into Eq. (5.29). The position of the DW along the pinning potential can be converted to the applied magnetic field. This is because when a magnetic field is applied, the central position of the DW shifts within the well at equilibrium. The relationship between the applied magnetic field and the position of the DW is

$$H = \frac{\left(\frac{\partial\sigma}{\partial q}\right)}{2M}. \tag{5.30}$$

Using Eq. (5.29) and (5.30), the magnetic field dependence of the oscillation period

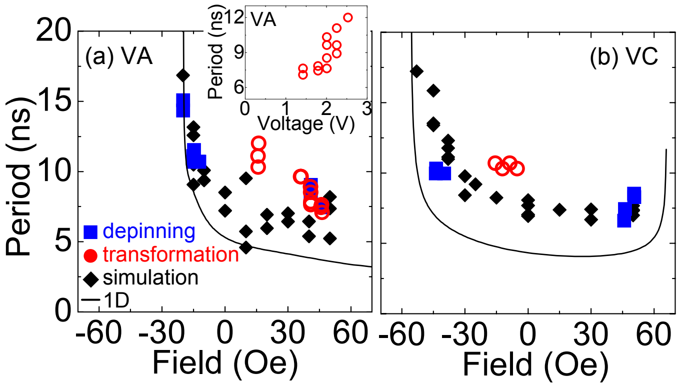

Figure 5.32: Oscillation periods of depinning (solid squares) and transformation (open circles) observed in (a) V_A wall and (b) V_C wall. Periods from micromagnetic simulations are shown as solid diamonds, where the periods of corresponding DWs undergoing small amplitude oscillation in the potential well are calculated. Solid line is the estimated oscillation period from pinning potential profile using Eq. (5.29). The parameters used are H_K=750 Oe and Δ=23 nm. Inset: Oscillation periods of the transformation probability of the V_A wall, plotted against the pulse amplitude.

can be obtained and are plotted as solid lines in Fig. 5.32 (a) and (b).

The period obtained in this manner is the zero current limit of the small amplitude oscillation. If σ were to be a perfect parabola, the oscillation period should be constant against the magnetic field; the variation in the periods represents the deviation of the well from a parabola. The oscillation period predicted from the pinning potential profile qualitatively agrees with the experimental results and the simulations. However, the values do not agree well, particularly for the V_C walls. This may be attributed to the uncertainty of the H_K and Δ values substituted into Eq. (5.29). The values we obtained from micromagnetic simulations reflects H_K and Δ for a DW located in an ideal nanowire without any pinning center. The effects of the pinning potential on H_K and Δ are neglected, which are yet to be understood.

5.7 Discussion

Depinning DWs from a pinning center turns out to be a very complicated phenomena. Depending on the applied magnetic field and the current pulse (both amplitude and length), the DW can depin, transform or remain as it is. In addition, at low magnetic field, the critical current to depin the DW becomes so high that significant heating occurs, which adds another parameter to consider, the temperature. For the racetrack memory, the zero field critical current is one of the most important parameters. Several methods are proposed to reduce the critical current at zero field in permalloy nanowires.

The first one is to look for a DW structure that has very small H_K and Δ. In the bifurcation regime, the critical current is determined by the product of H_K and Δ. Comparing the vortex and transverse walls, the product $H_K\Delta$ is significantly smaller for the vortex walls. However the critical current for the two DWs showed little difference (see Fig. 5.9). This was explained by (a) the vortex walls transforming into transverse walls before depinning and (b) the temperature of the nanowire becomes too high that thermal processes dominate the depinning. Consequently, $H_K\Delta$ is still too large for the vortex walls to depin at zero field. If $H_K\Delta$ can be lowered to a point where transformation does not take place, it may become possible to observe bifurcation induced depinning at lower current.

The second possibility, and a more realistic one, is to induce oscillatory depinning at zero field. This is because the critical current to induce oscillatory depinning is below the current to cause either normal depinning or bifurcation induced depinning (see Fig. 5.24 (b)). With regard to the trajectory of the DW for oscillatory depinning, the DW exits the pinning potential from the edge of the well, as in the normal depinning case. Thus in order to ensure that oscillatory depinning takes place at low field, it is important to induce normal depinning at as low field as possible. Intuitively, from Fig. 5.18, the criteria will be to reduce the width (d) of the pinning potential.

Mathematically, this condition can be found by equating Eq. 5.10 and Eq. 5.14 and find the field a^* where the crossover occurs. If a^* can be reduced close to zero, normal depinning can take place at low field. Solving for a^* by equating Eq. 5.10

and Eq. 5.14 is mathematically possible, but the solution is not readable. To obtain a simpler formula, Eq. 5.12 and Eq. 5.16 are instead equated to find a^*. Although the generality of the initial conditions are lost, it still gives the dependence of a^* on various parameters. The result is

$$a^* = px_d - \frac{p(\mp\pi \pm \sqrt{\pi^2 - 4 + \frac{8\beta^2}{p}})}{2(1 - \frac{2\beta^2}{p})(-\beta + \sqrt{\beta^2 + \frac{p}{2}})}. \tag{5.31}$$

To simplify the form, we assume $\beta \ll 1$ and neglect terms that are of the order of β^2. This gives

$$a^* = px_d - \frac{pk}{2(-\beta + \sqrt{\frac{p}{2}})}. \tag{5.32}$$

$$H_a^* = \frac{V}{M_S} - \frac{kV\Delta}{2M_S d(-\beta + \sqrt{\frac{V\Delta}{2M_S dH_K}})}$$

where $k = (\mp\pi \pm \sqrt{\pi^2 - 4})$ is just a constant. H_a^* is plotted as a function of potential well width using different β in Fig. 5.33. The horizontal dashed line is the zero current depinning field. H_a^* can be significantly reduced when the well width becomes of the order of DW width. In addition, large β can contribute to reducing H_a^*. Thus a narrow pinning potential well, whose width is comparable to the size of the dynamics DW width, is necessary to reduce the critical current at zero field.

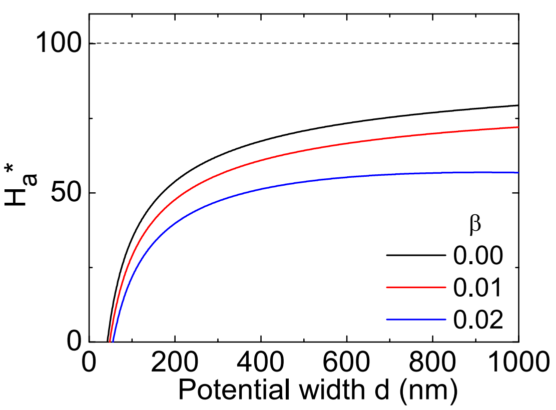

Figure 5.33: Cross over field H_a^*, i.e. the magnetic field at which the critical current for normal depinning and bifurcation induced depinning equals, plotted against the parabolic potential well width d with three different β. The parameters used in the calculations are, $H_K = 750$ Oe, $\Delta = 22$ nm and $V = 8 \times 10^4$ erg/cm^3. The horizontal dashed line is the zero current depinning field.

Chapter 6

DW velocity measurements

6.1 Introduction

6.1.1 History of DW velocity measurements

Along with the critical current density that determines the threshold current density needed to trigger domain wall (DW) motion, the DW velocity is the other crucial parameter that needs to be known for device applications. With regards to the racetrack memory, the DW velocity determines the operation speed, or the clock cycle, of the device. Thus solid understanding of how to control the DW velocity is necessary. In particular, the speed of current driven DWs is nearly an unknown parameter, only a few results have been reported. Moreover, the reported DW velocities are orders of magnitude smaller than what is reported in theoretical predictions.

Since the early 1950s, the DW velocity has been measured in magnetic materials from bulk to thin films. Most of these measurements relies on optical techniques based on magneto-optic interactions. In these types of measurements the laser spot size determines the spatial resolution, i.e. the minimum length scale that can be probed. Typically the laser spot size ranges from minimum 500 nm to more than a few microns, which makes it difficult to measure DW velocities in magnetic nanostructures. The application of bubble domains to memory and logic devices extended the investigation of DW velocity and numbers of different techniques were introduced to measure the velocity, which do not rely on the magneto-optic interactions. One of the most powerful technique is the extended Sixtus-Tonk method [129, 130]; a method based on measuring the induced voltage in pick-up coils caused by the change in the magnetization of the material, or the DW motion. This concept can be applied to measure DW velocities in magnetic nanostructures, however the device fabrication and the detection of the small induced voltage remain as difficult tasks.

A more suited approach for measuring DW velocity in magnetic nanostructures was presented in 1999 from Ono et.al[131]. They used the giant magnetoresistance (GMR) effect to infer the position of the DW in a 500 nm wide 2 mm long magnetic wire. Although their devices were 2 mm long due to technical issues of their measurement method, this approach is very attractive for measuring DW velocities in small structures. However, with regards to measuring current driven DW velocity, GMR based measurement method faces a problem; a significant amount of current shunting occurs through the non-magnetic layer, which also causes additional problems such as the self field (Oersted field from the current passing through the device) effect.

To overcome these issues, we use a single layered magnetic material that shows relatively large anisotropic magnetoresistance (AMR) effect. Contrary to GMR, where the resistance is proportional to the total magnetization of the magnetic free layer, AMR provides information of the magnetization configuration of the magnetic layer through resistance measurements. In soft magnetic materials, such as in permalloy, the resistance of a patterned nanowire tells whether a DW is located in the section where the resistance is measured. By monitoring the nanowire resistance in real time, it is possible to estimate the DW velocity.

6.1.2 Experimental setup

Figure 6.1 shows the scanning electron microscopy (SEM) image of the permalloy nanowire with the experimental setup laid on top of the image. 100-300 nm wide permalloy nanowires are used. The nanowire has two straight arms perpendicular to each other. These arms are connected via a quarter circle whose radius is 3 μm. Both end of these arms are tapered to a sharp point to prevent the formation of DWs

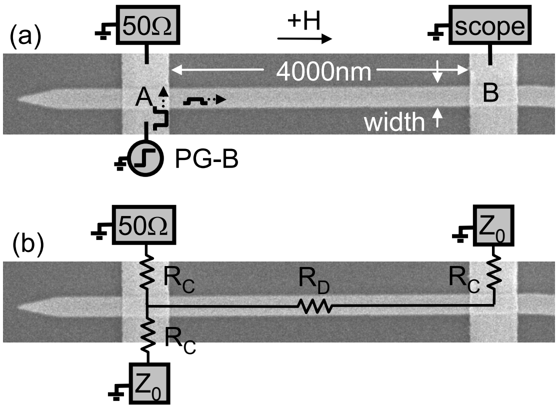

Figure 6.1: Scanning electron microscopy image of a permalloy nanowire (horizontal) and its electrical contacts (vertical lines). (a) A schematic illustration of the real-time resistance measurement setup is overlaid on the image. (b) Equivalent resistance network of the measurement setup shown in (a).

outside the contact line [121] and to assist annihilation of any DW that enters this region. See Fig. 6.13 (a) for the full SEM image of the device. Only the horizontal arm is used to measure the DW velocity.

High frequency probes are used to make contact to the devices. Most of the data presented in this chapter are taken with probes of dc-40 GHz bandwidth. The local field generation method is used to inject a DW into section A-B of the nanowire. A pulse generator (PG-B, Picosecond Pulse Labs, model 10300B) is connected to contact line A. A 50 Ω termination is connected to the other end of line A. Two types of measurement configurations are used in this chapter, the pulse generator is either connected to the upper half of line A or to the lower half of line A. The details of these two setups are described in the next section. A 6GHz real-time oscilloscope (Agilent Technologies, model 54855A) is connected to contact line B via a probe.

6.2 Time resolved resistance measurements

6.2.1 Procedure of detecting moving DWs

The pulse that is injected into line A, whose purpose is to create a DW in section A-B, splits into two pulses at the intersection of line A and the nanowire. The amplitudes of the split pulses depend on the resistance ratio of contact line A and section A-B of the nanowire. In all nanowires, the resistance of the contact line is $\sim 80-85\Omega$. The resistance of section A-B of the nanowire varies with the wire width; it ranges from $\sim 370\Omega$ (300 nm wide) to $\sim 1180\Omega$ (100 nm wide). The amplitudes of the voltage pulse that flow into the oscilloscope (V_{SC}) and into the 50 Ω termination (V_{50}) are expressed by

$$V_{SC} = \frac{Z_0 2V_{IN}}{2R_D + 3(R_C + Z_0)} \tag{6.1}$$

$$V_{50} = \frac{Z_0(R_D + (R_C + Z_0)2V_{IN}}{(R_C + Z_0)(2R_D + 3(R_C + Z_0))} \tag{6.2}$$

where R_D is the resistance of section A-B of the nanowire and R_C is half the resistance of the contact line. See Fig. 6.1 (b) for the definitions of the resistances. Z_0 is the impedance of the transmission line (50 Ω). The voltage measured by the oscilloscope is roughly inversely proportional to the nanowire resistance R_D. Conversely, the nanowire resistance can be estimated from the measured scope voltage. As the voltage pulse propagates from line A to B, current flows into the nanowire and the magnitude of this current is simply $I_D = Z_0 V_{SC}$. To clarify, the role of the voltage pulse that is injected from line A is threefold; (1) to generate local magnetic field to inject a DW into section A-B, (2) to pass a voltage pulse (V_{SC}) to the scope to measure the nanowire resistance and (3) inject a current (I_D) into the nanowire, which turns out to be affecting the DW velocity. However, as shown in the previous chapter, the change in the resistance from a magnetized state to a state with a DW present in section A-B is ~0.2 to 0.3 Ω, approximately 0.1% change in the total resistance. To detect this small resistance change in real time is a challenging task. We thus employ a background subtraction method to resolve this small signal change.

The background of the signal is removed by conducting two sets of independent measurements to capture two traces in the oscilloscope and subsequently subtracting one from the other. The first set of measurement is to conduct the normal DW injection procedure, using the local field generation method, and capture a trace in the oscilloscope. We go over this procedure again to clarify the magnetic field sequence used here.

First a magnetic field $-H_{SAT}$, generated by the homemade electromagnet, is applied in one direction (take -x as an example) to magnetize the nanowire magnetization. Then the direction of this field is reversed to a field H to assist the subsequent injection and propagation of the DW. Note that H is equivalent to H_{INJ} in Chapter 5. With H turned on, the voltage pulse is injected from line A. Consequently, the DW is injected into section A-B and it will propagate from A to B owing to the driving force, which can be either H or the current that flows in the nanowire, or both. As mentioned above, the injected voltage pulse will split into two voltage pulses and one will reach the oscilloscope to obtain V_{SC}. To avoid any hysteretic effect of the electromagnet, the magnetic field is then ramped up to H_{SAT}. This procedure is repeated over more than 16,000 times to acquire an averaged trace V_S in the oscilloscope.

The second measurement is conducted in the same manner as the first one, except that the direction of H_{SAT} is reversed. A magnetic field H_{SAT} is first applied to magnetize the nanowire. This field is then reduced to H without changing its direction. The same voltage pulse is injected from line A with H turned on, however, no DW is injected this time since the generated local field stabilize the magnetic configuration of the nanowire. The voltage pulse that reaches the oscilloscope now contain no information of the DW, i.e. it represents the resistance level of the magnetized state. Again, to avoid any hysteretic effect of the electromagnet, the magnetic field is then changed to $-H_{SAT}$. This procedure is also repeated over more than 16,000 times to acquire an averaged reference trace V_R in the oscilloscope.

Figure 6.2 (a) and (b) show the magnetic field sequence measured using the real time oscilloscope via the Hall voltage from the Hall sensor attached to one end of the electromagnet. The field sequences shown are examples of (a) normal procedure to inject a DW and (b) the procedure to acquire the corresponding reference trace. The red arrow indicates where the voltage pulse is injected from line A to create

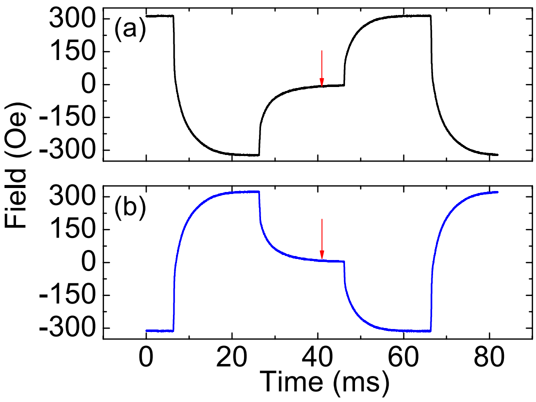

Figure 6.2: Magnetic fields measured during the DW velocity measurements. The two panels show the field cycling when (a) DW injection procedure is conducted and (b) corresponding reference trace measurement is performed. The red arrows indicate the time when the voltage pulse is injected to create DWs.

the DW. Note that the length of the voltage pulse is 100 ns, orders of magnitude smaller than the time scale shown in the figure. Conversely, the magnetic field during the DW injection/propagation process can be regarded as constant, even though the magnetic field needs ∼10 ms to reach the target field due to the inductance of the electromagnet.

6.2.2 Definition of parameters

Exemplary traces obtained in the oscilloscope using the two measurement procedures described above are shown in Fig. 6.3 (a). Since the difference between the two traces V_S and V_R are small, it is difficult to resolve the difference in the two in this plot. The black solid line in Fig. 6.3 (b) shows the difference between the two, $\Delta V \equiv V_S - V_R$. The non-zero ΔV represents the signal from the DW; ΔV is proportional to resistance difference between the state with and without a DW, which was defined as ΔR in the previous chapter. After the pulse is injected at time t=0, the signal ΔV increases to a non-zero value for a certain duration τ and then drops back to zero. This indicates that the DW is nucleated and injected into section A-B right after the voltage pulse is injected and being expelled from the region after τ. Since a 16 Oe magnetic field is

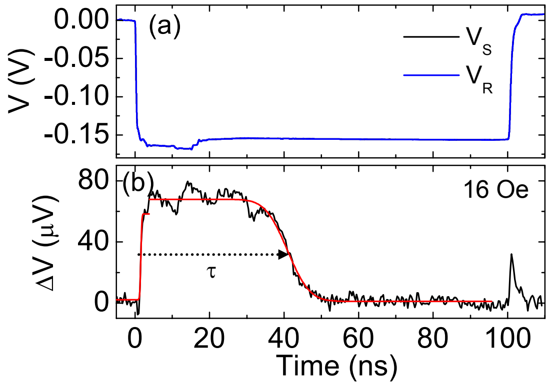

Figure 6.3: (a) Exemplary traces obtained in the oscilloscope when a DW is injected into the nanowire (black line) and when no DW exists in the nanowire (blue line). (b) Subtraction of the two traces shown in (a). The red line is a fit using Eq. (6.3) and (6.4).

applied while the pulse is injected, the DW is expected to move toward line B after it is nucleated in section A-B. Thus the drop in the signal corresponds to the DW leaving section A-B from the side of line B, indicating that it traveled a distance of nearly 4 μm.

In order to extract useful parameters out of the signal trace ΔV, we fit the trace with an analytical formula. The rise and fall part of the ΔV are fitted to, respectively,

$$\Delta V_{rise} = \frac{A}{2} erf(\frac{t - t_i}{\Delta\tau_N}) + A_0 \tag{6.3}$$

$$\Delta V_{fall} = \frac{A_1}{2} erfc(\frac{t - t_f}{\Delta\tau}) + A_2 \tag{6.4}$$

The red solid lines in Fig. 6.4 (b) show the fitted curves. Note that the small peak observed in the ΔV trace at the end of the voltage pulse (at ∼100 ns) is an artifact of the signal processing. A small jitter can cause this peak since the voltage change is abrupt at this point. Note that since the oscilloscope is triggered at time t=0, the time jitter is larger at longer time. It is negligible at the trigger point (at time t=0).

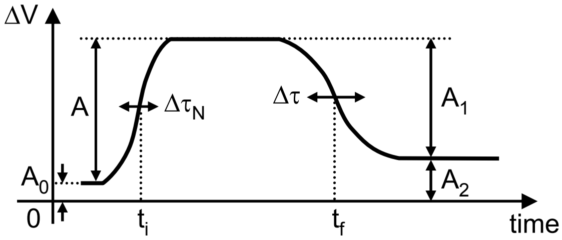

Figure 6.4: Definition of the parameters used in Eq. (6.3) and (6.4).

6.3 Field-driven DW velocity

6.3.1 Influence of current on field-driven DW velocity

In order to investigate the effect of the current on the field-driven DW velocity, we vary the sign and amplitude of the voltage pulse injected from line A. When a positive voltage pulse is injected, a positive current flows into the nanowire. Positive currents are defined as electrons flowing from line B to line A (towards the -x direction). The definition of x is shown at the top of Fig. 6.5. The current flows are shown by black dotted arrows in Fig. 6.5 (a-d).

In order to create a head to head (HH) wall in section A-B, a positive local field must be generated at line A. Positive field is defined as a field pointing toward the positive x direction. To generate a positive local field using a positive voltage pulse, the pulse generator and the 50 Ω termination need to be placed as shown in Fig. 6.5 (a). To change the current direction that flows into the nanowire, the pulse polarity needs to be changed. However, the local field generated by the negative voltage pulse will generate a negative local field when the configuration shown in (a) is used. By interchanging the position of the pulse generator and the 50 Ω termination, as shown in Fig. 6.5 (c), a negative voltage pulse can generate a positive local field, thereby creating a HH wall in section A-B.

To create a tail to tail (TT) wall in section A-B, now a negative local field needs to be generated. The experimental setup shown in Fig. 6.5 (b) and (d) allow to generate a negative local field using a positive and negative voltage pulse, respectively. The

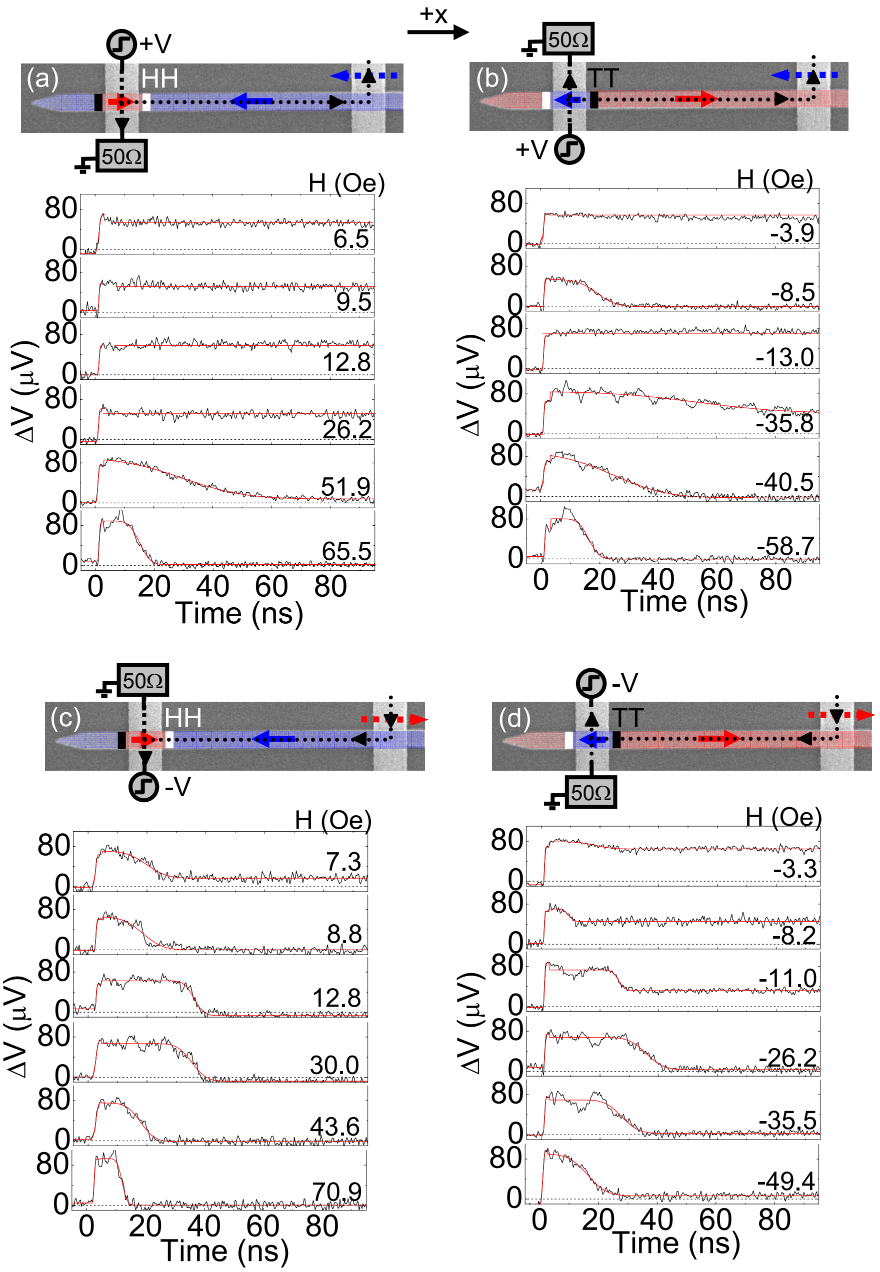

Figure 6.5: (a-d) Top panels: SEM images of the device with illustrations of the measurement circuit. The colored thick arrows indicate the magnetization direction of the nanowire. Dotted black lines and arrows show the current flow in the device. Dashed colored arrows on the right side show the direction of the local field generated by the current passing through line B. All four possible configurations, either a HH DW or a TT DW with positive or negative current flowing in the nanowire are shown. Bottom panels: Typical signal traces $\Delta V(t)$ for the fields indicated in each panel. A voltage pulse, ±2.8 V and 100ns long is injected to create a DW in section A-B. Solid red lines are fits using Eq. (6.3) and (6.4).

magnetization directions of the domains in the permalloy nanowire are represented by the colored thick arrows in Fig. 6.5. The white and black vertical lines represent a HH and TT DW, respectively.

As an example, data from 300 nm wide permalloy nanowires are shown. The signal traces ΔV taken at different fields for both HH and TT wall are shown in Fig. 6.5 (a-d) as black solid lines. Either 2.8 V or -2.8 V are used to create the DW. For these voltage amplitudes, a current density of approximately $\sim 1.4 \times 10^8 A/cm^2$ is flowing through the nanowire. The red solid lines are fits to the signal traces using Eq. (6.3) and (6.4). The magnetic field applied during these measurements are listed on the right side of each trace. In all traces, the rise part of ΔV seems to be nearly independent of the field and current direction. On the other hand, the fall part significantly depends on the magnetic field and the current direction. In each trace, there are some fluctuations in the ΔV level, which will be discussed later on. Note that in some cases, especially when a positive current is flowing in the nanowire (a, b), ΔV does not drop to zero and maintain its level after the DW injection, indicating that the DW does not exit from section A-B. In these cases, the traces are not fitted and the red lines are simply guides to the eye.

In addition, typically when a TT wall is injected using a negative voltage (d), ΔV changes its value to a non-zero value at t_f and maintain this level afterwards. The change in the ΔV level can be associated with either a change in the DW structure, which is proportional to the ΔR and thus ΔV, or a distribution in the DW velocity. Since the traces shown are an average of more than 16,000 injection events, a distribution in the DW velocity exists. It is possible that in some injection process, the DW did not exit section A-B, leading to a non-zero ΔV level at the long time limit (a non-zero A_2 in Fig. 6.4).

It should be noted that a local magnetic field is also generated at contact line B when a voltage pulse is passed through the nanowire. The direction of the this local field is indicated by the colored dotted arrows in Fig. 6.5 (a-d). When the direction of the local field generated at line B coincides with the direction of the local field generated at line A, the DW that has propagated through section A-B can exit from line B with the aid of the local field. On the other hand, when the two field opposes

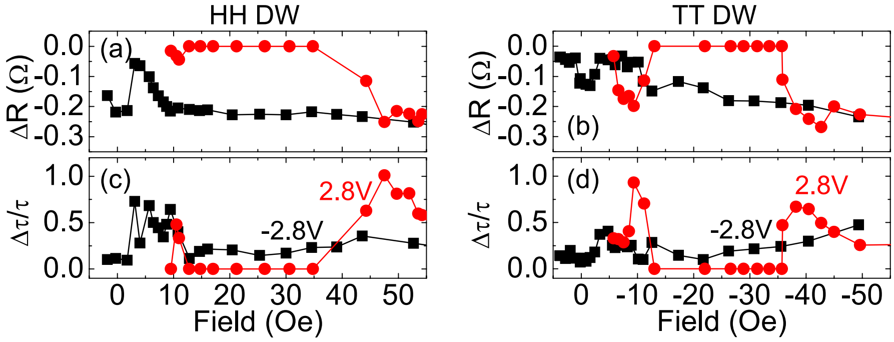

Figure 6.6: (a,c) The field dependence of the calculated ΔR from the signal amplitudes ΔV. Voltage pulses of 2.8 V (red cirlces) and -2.8 V (black squares) are used to inject a DW. (b,d) Normalized fall time of the signal traces. Left and right panels correspond to data from HH and TT wall, respectively.

each other, the propagated DW will suffer from crossing line B due to the local field. This is the case when a HH wall is created with a positive voltage pulse (a) or a TT wall is created with a negative voltage pulse (d). The size of the local magnetic field generated at line B depends on the current that flows into the nanowire. For 300 nm wide nanowires, the local field is 15 Oe when a 1.0 V voltage pulse is injected from line A. For the cases shown in Fig. 6.5 (a-d), where a ±2.8 V voltage pulses are used, ±42 Oe of a local field is generated. However, note that these numbers are based on a assumption that a homogeneous current is flowing through line B, which is probably not the case. Thus the estimated field should be regarded as a mean field that is generated around line B.

The parameters extracted from fitting Eq. (6.3) and (6.4) to the traces are shown in Figure 6.6. Either 2.8 V or -2.8 V are used to inject a HH or TT wall. First, we estimate the ΔR value of the DW propagating through section A-B from the amplitude A_1 of the fall part in the traces. In most cases, A_1 is proportional to ΔR of the DW that propagates through the nanowire. However, as seen in the Fig. 6.5 (d), when the ΔV level does not fall to zero after the DW is injected, this is not the case. The conversion of A_1 to ΔR can be done by rearranging Eq. (6.1) and are expressed as

$$\Delta R = \Delta V \frac{Z_0 V_{IN}}{V_{SC}^2}. \tag{6.5}$$

The field dependence of the calculated ΔR values are plotted in Fig. 6.6 (a) and (b) for HH and TT walls, respectively. When a HH wall is injected using a negative voltage pulse, ΔR ranges from ∼-0.20 to ∼-0.26 at fields higher than 10 Oe. Note that at even higher fields, the magnitude of ΔR further increases (see Fig. 6.10 (a)). For the positive voltage pulses, ΔR drops to zero below ∼35 Oe. This can possibly be related to the local magnetic field generated at line B, which prevents the HH wall to go across in this situation (see Fig. 6.5 (a) for the direction of the local field generated at line B).

To investigate whether the local field generated at line B prevents the wall to go across, a TT wall is injected using a positive voltage. In this case, the local field will aid the wall to go across line B. However, as shown in Fig. 6.6 (b), ΔR drops to zero at ∼-35 Oe, indicating that the wall does not exit section A-B. Moreover, non zero ΔR is observed at even lower fields (-6 Oe to -11 Oe), which cannot be accounted for by the local field. When a negative voltage is used to inject a TT wall, ΔR shows a non-zero value above ∼-10 Oe. However, compared to the ΔR of the HH wall injected using a negative voltage pulse, the magnitude is lower in the low field region. We infer that this is caused by the local field at line B preventing the TT wall to go across line B, thus reducing the probability that the wall exits section A-B. The drop in ΔR to zero in the low field range for the positive voltage cases therefore must be related to the direction of the current that flows into the nanowire.

The width $\Delta\tau$ of fall part, normalized to the mean time $\tau \equiv \tau_f - \tau_i$ the DW takes to exit section A-B, is plotted in Fig. 6.6 for (c) HH and (d) TT walls. When a positive voltage is used to inject a DW, the reduction in ΔR to zero at ±35 Oe is associated with a significant increase in $\frac{\Delta\tau}{\tau}$. In all cases, $\frac{\Delta\tau}{\tau}$ seems to increase when the magnitude of the field is below ∼12 Oe.

There are several possible explanations that can account for the finite $\frac{\Delta\tau}{\tau}$. First, the intrinsic width of the DW clearly leads to a progressive reduction of the ΔR as the DW crosses line B. Second, any variations in DW velocity in successive experiments

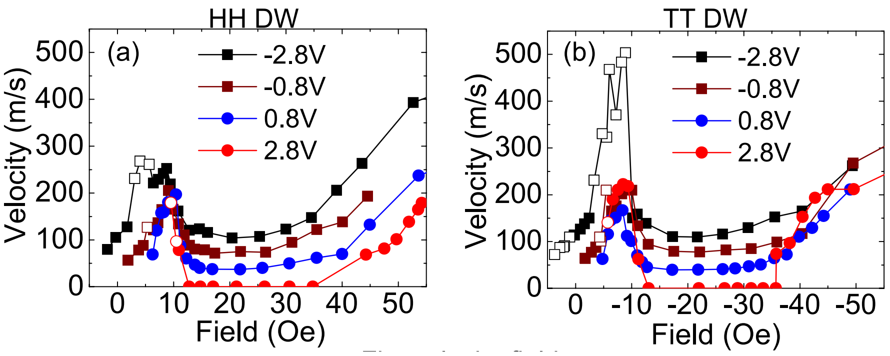

Figure 6.7: DW velocity plotted as a function of magnetic field. Various amplitudes of the voltage pulse are used to inject a (a) HH and (b) TT DW. The open symbols represent the DW velocity when the corresponding ΔR is smaller than ~0.1 Ω. Note that the experimental setup is limited to measurements above 40 m/s. Velocities below this limit are shown as zero velocities.

will cause a distribution of the exit times. Another possibility is that the DW profile might become significantly distorted, for example, due to pinning at defects along the edges of the nanowire. However, this is unlikely since the measured $\frac{\Delta\tau}{\tau}$ would require very large distortions, distortions larger than the length of the nanowire. Moreover, this would lead to an progressive increase in the magnitude of ΔV, which is not observed.

The DW velocity can be estimated by calculating the following quantity,

$$v = \frac{L}{\tau} \approx \frac{4\mu m}{t_f - t_i} \tag{6.6}$$

The dependence of the DW velocity on the magnetic field and the injected voltage pulse are shown in Fig. 6.7 for (a) HH and (b) TT walls. The open symbols represent the DW velocity when the corresponding ΔR is smaller than ~0.1 Ω. These points are representative of traces where the ΔV level does not drop to zero at the long time limit (non zero A_2 in Fig. 6.4). Thus it is likely that the open symbols do not represent the DW velocity and may represent the time the DW transforms into another wall structure that has a different ΔR, if any transformation may occur. Note that the experimental setup is limited to measurements of DW velocities above

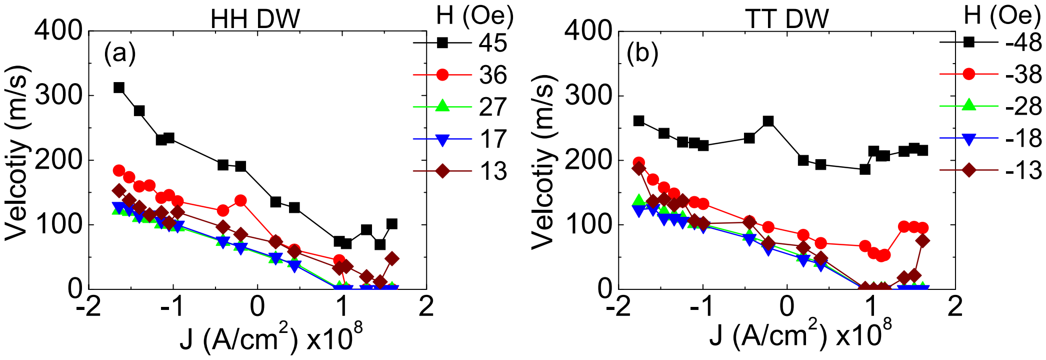

Figure 6.8: Field-driven DW velocities plotted as a function of the current density that flows through the nanowire. Corresponding magnetic fields are listed on the right. Left and right panels correspond to data from HH and TT wall, respectively.

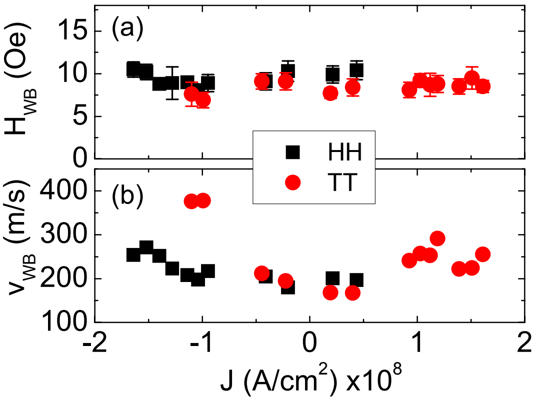

Figure 6.9: The Walker breakdown field (a) and the corresponding DW velocity (b) are plotted against the current density that flows in the nanowire. Black squares and red circles represent data for HH and TT walls, respectively.

40 m/s, since the maximum pulse length is 100 ns. Velocities below this limit are shown as zero velocities.

As a general trend, the DW velocity first increases as the field magnitude is increased. A maximum in the DW velocity is observed at $\sim \pm 10$ Oe. Further increase in the field results in a drop in the velocity. A minimum in the DW velocity is observed at around $\sim \pm 20$-30 Oe, above which the velocity starts to increase again. The field at which the velocity peaks is called the Walker breakdown field[132].

To visualize the effect of the current on the DW velocity, the DW velocity at selected fields are plotted as a function of current density in Fig. 6.8 for (a) HH and (b) TT walls. For both wall types, the DW velocity increases when the current density is increased in the negative direction. In most of the field values used here, the relationship between the DW velocity and the current density is approximately linear. At higher fields, the relationship seems to deviate from linear. The dependence of the Walker breakdown field H_{WB} and the velocity v_{WB} at this field are shown in Fig. 6.9 (a) and (b), respectively. The breakdown field shows little dependence on the current density, whereas v_{WB} shows non-linear dependence on the current density.

6.3.2 High field velocity

It is interesting to measure how fast the DW travels along the nanowire when the magnetic field is increased. Figure 6.10 (b) shows the DW velocity plotted as a function of magnetic field in a different 300 nm wide nanowire. The black squares (HH wall) and red circles (TT wall) represent the DW velocity when current densities are $\pm 1.5 \times 10^8$ A/cm^2, respectively. Although the velocity is not a linear function of the magnetic field, it increases up to ~800 m/s when the field exceeds 120 Oe. At higher fields, the difference in the velocity between positive and negative current density seems to diminish. The associated ΔV (A_1 in Fig. 6.4) are plotted versus magnetic field in Fig. 6.10 (a). Interestingly, ΔV shows a significant increase at higher fields.

Micromagnetic simulation reproduces the non-linear relationship between the DW velocity and the magnetic field. Figure 6.10 (c) show the DW velocity calculated from

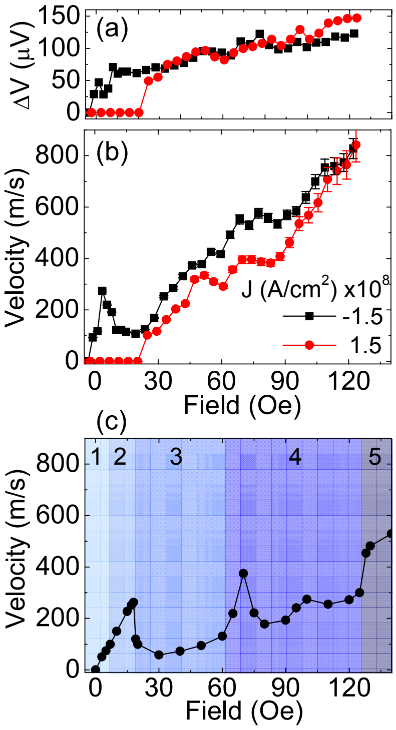

Figure 6.10: (a) Amplitudes of the signal traces ΔV (or A_1 in Fig. 6.4) and (b) DW velocity plotted as a function of magnetic field. The current density flowing through the nanowire is $\pm 1.5 \times 10^8 A/cm^2$. (c) DW velocity calculated from micromagnetic simulations. The background color and the numbers indicate regions with different propagation mode.

micromagnetic simulation. Simulation is conducted on a 4 μm long 300 nm wide 10 nm thick permalloy nanowire with a moving boundary condition employed[96]. The Gilbert damping constant is set to 0.02. The initial wall structure is a vortex wall. The DW velocity is calculated by first simulating the time it takes to travel 4μm. The velocity is deduced by dividing the distance 4μm by this travel time. From the simulations, the non-linear relationship derives from the change in the propagation mode that occurs at certain fields. The colors in the background and the symbols on top represent the propagation mode. When the field is below the Walker breakdown field, in region 1, the DW propagates along the nanowire maintaining its vortex structure, whereas in region 2, the structure changes from vortex to transverse wall during the propagation. Note that the transverse wall does not change its structure afterwards. Thus the Walker breakdown field (the boundary of region 2-3) is the breakdown field for the transverse wall. The breakdown field for the vortex wall is the boundary of region 1-2. When the field is above the Walker breakdown field, the structure change becomes periodic. For example, in region 3, the structure changes periodically between vortex wall and transverse wall. At higher fields, more complicated structures get involved. The DW structure also gets distorted at higher fields, which explains why ΔR increases at higher fields.

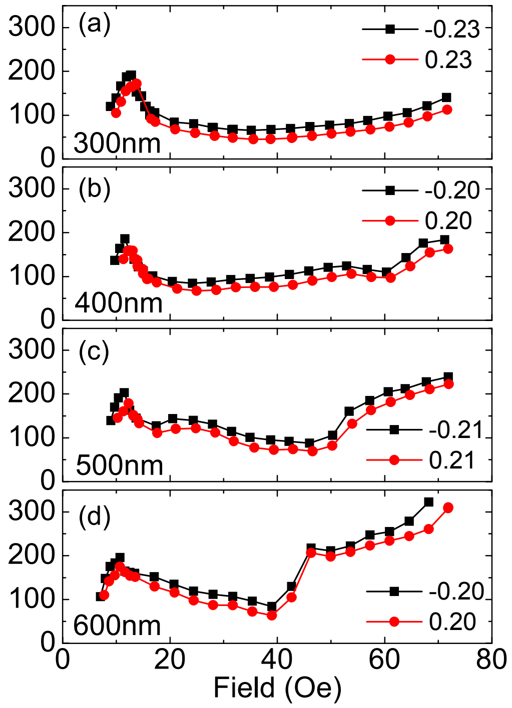

Figure 6.11: (a-d) DW velocity of a NiFeCo nanowire plotted as a function of magnetic field. The current density flowing through the nanowire is $\sim \pm 0.2 \times 10^8$ A/cm^2. The width of the nanowire are indicated at the bottom left of each panel. Data from the NiFeCo nanowires are only shown in this and the next figure.

6.3.3 Wire width dependence

According to micromagnetic simulations, the non-linear dependence of the DW velocity on the magnetic field derives from the changes in the DW structure during its propagation. Thus it can be expected that by changing the size of the nanowire, different DW structures can be involved during the DW propagation and consequently changes the field driven DW velocity.

Figure 6.11 (a-d) show the nanowire width dependence of the DW velocity versus field. The data shown here are from nanowires patterned from a film of SiOx/30 nm MgO/14 nm $Ni_{65}Fe_{20}Co_{15}$/15 nm Ru. The nanowire is 22 μm long and the width varies from 300 to 600 nm. DW velocities are measured at current densities of $\pm 0.2 \times 10^8$ A/cm^2. Discontinuities in the DW velocity are observed at higher fields. As

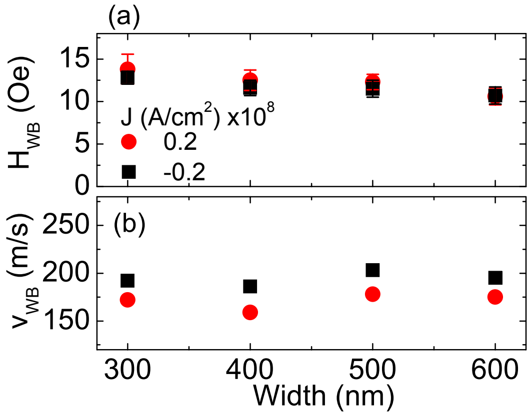

Figure 6.12: The Walker breakdown field (a) and the corresponding DW velocity (b) are plotted against the width of the NiFeCo nanowire. Black squares and red circles represent data for negative and positive currents flowing through the nanowire, respectively.

the nanowire width is increased, this discontinuity in the DW velocity becomes more pronounced. In addition, the field at which the discontinuity is observed becomes smaller when the width is increased. This can be explained by assuming the cause in the discontinuity is due to a change in the DW propagation mode. As the nanowire width is increased, it requires less field to accommodate a different wall structure that occurs in the next propagation mode.

The dependence of the Walker breakdown field H_{WB} and its maximum velocity v_{WB} on the nanowire width is shown in Fig. 6.12 (a) and (b), respectively. The breakdown field shows a slight dependence on the wire width, whereas the maximum velocity is nearly independent of the width.

6.4 Current driven DW velocity

In Fig. 6.7, when a DW is injected into section A-B using a high amplitude negative voltage pulse, a non-zero DW velocity is observed. The estimated ΔR is also non-zero near zero field, as shown in Fig. 6.6 (a) and (b), thus indicating that the DW is driven out from section A-B. The applied field is too small to cause DW motion since

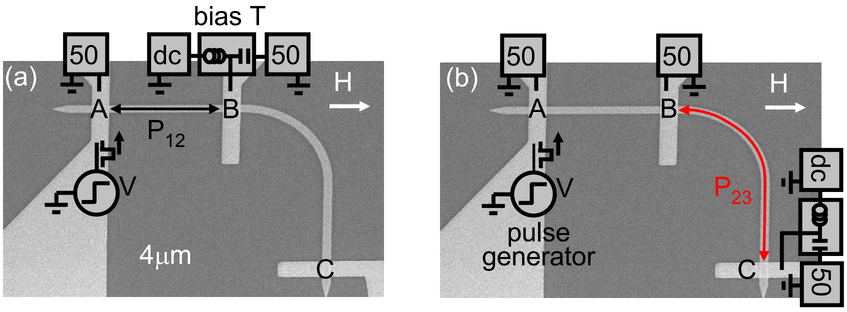

Figure 6.13: SEM images of the device with illustrations of the measurement circuit. Labels A, B and C are for the contact lines. The box labeled dc includes both a current source and a voltmeter connected in parallel. Solid arrows represent the portion of the permalloy nanowire where the resistance is measured: (a) A-B and (b) B-C.

it is below the propagation field, the minimum field required to move a DW along the nanowire (∼5 Oe). Therefore it is reasonable to expect that the DW was driven out from section A-B by current. In this section, we explore this current driven DW velocity in details.

6.4.1 Quasi-static velocity measurements

We first investigate whether the DW indeed travels ∼4μm and exits section A-B from the side of line B, when driven by current. To do this, we make use of the 90 degree corner of the permalloy nanowire and study the current driven motion in a quasi-static way. In quasi-static measurements, we use nanosecond long pulses to inject and move a DW, but measure the dc resistance of the device using voltmeters. Figure 6.13 (a) and (b) show the full SEM image of the permalloy nanowire with the experimental setup overlaid. Two different sets of measurements are conducted. In both cases, the local field generation method is used to inject a DW into section A-B of the nanowire. A magnetic field H is applied, if any, during the voltage pulse application. Note that this field (H) corresponds to H_{INJ} in Chapter 5.

First we measure the probability P_{AB} of injecting a DW in section A-B of the nanowire. The experimental setup shown in Fig. 6.13 (a) is utilized to study the effect of the current on P_{AB}. P_{AB} is found by repeating 50 times the injection procedure using the local field generation method. The resistance difference between the magnetized state (R_{SAT}) and the state after the injection procedure (R_i), i.e. $\Delta R \equiv R_i - R_{SAT}$, is used to find whether a DW is injected into section A-B. (ΔR is equivalent of ΔR_i in Chapter 5.) Voltage pulses that are 100 ns long and ±2.8 V are injected from line A to generate the local fields as well as to inject current into the nanowire. Injection of both head to head (HH) and tail to tail (TT) walls are investigated.

Black symbols in Fig. 6.14 (a-d) show the probability P_{AB}. For positive voltages, DWs are found in section A-B with near certainty, for both HH and TT walls, when $|H| < 5$ Oe. Fields outside this range exceed the DW propagation field along the nanowire so driving the DW out of this section. This is also true for negative voltages but, in the latter case, a significant drop in P_{AB} is observed close to zero field. One likely explanation is that the DW nucleated in the wire is driven out of section A-B by the current.

In order to validate this possibility we perform a second type of measurement in which we probe the probability P_{BC} of finding the domain wall in section B-C. The experimental setup shown in Fig. 6.13 (b) is now used to measure P_{BC}. Owing to the 50Ω termination connected to line B via the bias tee, there is nearly no pulse currents flowing into section B-C. Thus if the DW is driven out from section A-B and enters section B-C, it will come to rest. The red circles in Fig. 6.14 (a-d) show P_{BC} when a 100 ns long ±2.8 V voltage pulses are applied from line A to inject a DW in section A-B. These experiments confirm our hypothesis that the DW is indeed driven into section B-C, as discussed in detail below.

We first consider the case when a negative voltage pulse is used to create a HH DW. Values of P_{BC} close to one are observed near zero field, coincident with the dip in P_{AB}. This indicates that the DW was indeed driven by current alone from line A to section B-C. Note that the current density that flows in the nanowire when a -2.8 V pulse is applied is $\sim -1.4 \times 10^8$ A/cm^2. On the other hand, no such effect was observed for the TT DW case. As described previously, when the voltage pulse is injected from line A and passes through the nanowire and line B, a local magnetic

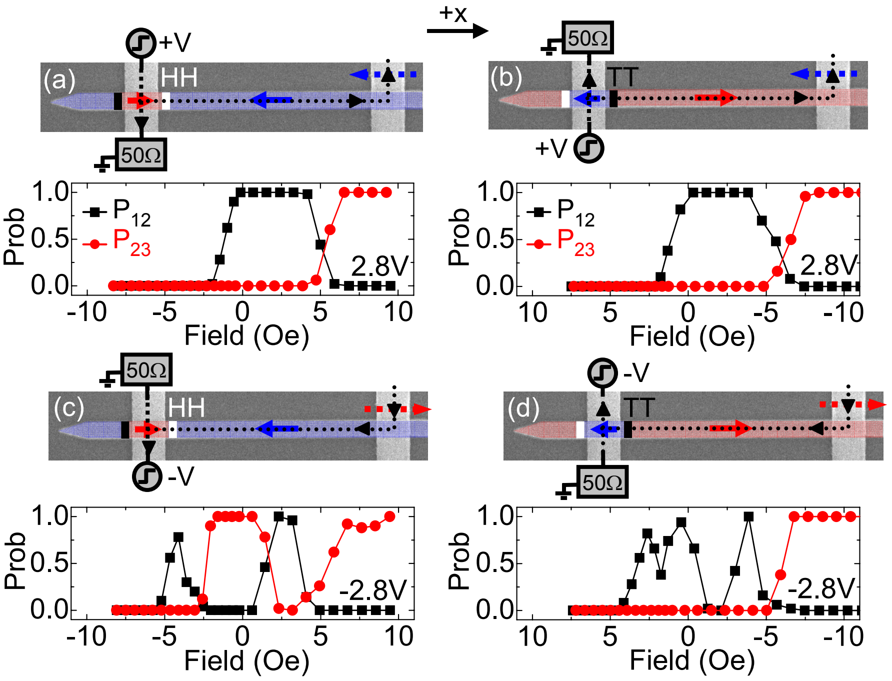

Figure 6.14: Top images: SEM images of the device with illustrations of the measurement circuit. The colored thick arrows indicate the magnetization direction of the nanowire. Dotted black lines and arrows show the current flow in the device. Dashed colored arrows on the right side show the direction of the local field generated by the current passing through line B. All four possible configurations, either a HH DW or a TT DW with positive or negative current flowing in the nanowire are shown. Bottom panels: Probability of injecting a DW into section A-B (black squares) P_{AB} and B-C (red circles) P_{BC} are plotted as a function of the field (H). All four possible configurations, either a HH DW or a TT DW with positive or negative current flowing in the nanowire are shown. A 100 ns long pulse is used in all cases. Dotted arrows represent the current flow, whereas the solid arrows represent the magnetization configuration.

field is generated at the vicinity of line B. For the case of TT wall injected using a negative voltage pulse, the local field at line B will prevent the DW from crossing. Thus, we infer that the TT DW is driven by the current close to line B, but that it is pinned to the left side of line B due to this local field. Note that we estimated this field, using crude assumptions, to be ~40 Oe when a -2.8V pulse is used, which is larger than the propagation field (~ 5 Oe)of the nanowire but significantly smaller than the DW nucleation field.

Finally, in all cases, regardless of the DW type or the voltage pulse polarity, when the magnitude of H exceeds the propagation field in the nanowire, and when the direction of H is such that it drives the DW towards section B-C (i.e. positive H for HH and negative H for TT), then P_{BC} jumps from zero to one.

The measurements above, using 100 ns long pulses, clearly show that in zero field the injected DWs move ~4 μm under current. By determining the minimum length of the pulse required to move the DW out of section A-B we can determine the DW velocity. In other words, when the pulse is too short the DW is trapped in this section. Under these circumstances two distinct values of ΔR are found when a DW is trapped in section A-B.

Fig. 6.15 shows histograms of ΔR when two different voltage pulses with amplitudes of -1.8V and -2.8V are used to inject a DW into section A-B. The histograms counts all experiments done with voltage pulse length varying from 1-20 ns. The two ΔR states correspond to two different DW states which are inferred as being vortex ($\Delta R \sim -0.3\Omega$) and transverse wall ($\Delta R \sim -0.23\Omega$). Since no artificial pinning site (notch) is patterned along the nanowire, the chirality of the DW cannot be inferred from the the size of ΔR. The pulse length dependence of P_{AB} can be measured for both domain wall types by identifying them from ΔR.

Figure 6.16 show maps of the probability of a transverse wall (a,c,e) and a vortex wall (b,d,f) being remained in section A-B (P_{AB}) plotted as a function of pulse amplitude and length. The applied field H are shown at the right edge of each map. The right and left panels correspond to HH and TT DWs, respectively. In all field range, when a positive voltage pulse is used, a transverse wall remains in section A-B, regardless of the length of the pulse. Note that below ~ ±1.8 V, no DW is

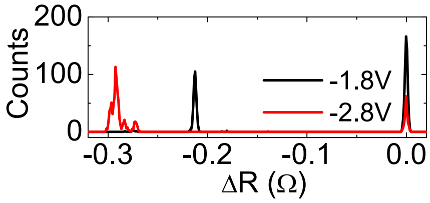

Figure 6.15: Histograms of ΔR when -1.8V (black line) and -2.8V (red line) voltage pulses (1-20 ns long) are used to inject a DW into section A-B. Corresponding DW structures, vortex (V) and transverse (T) walls are labeled with symbols.

nucleated since the local field generated at line A becomes too small to nucleate a reversed domain below this voltage amplitude. For the negative voltage pulses, P_{AB} shows dependence on the pulse length and magnetic field. At zero field, in a narrow amplitude window just above -1.8 V, a transverse DW is trapped in section A-B with very high probability, independent of pulse length. For higher amplitudes vortex DWs are found in section A-B up to pulse lengths of ~25-30 ns above which no DW is found. We thus surmise that the vortex DWs are driven out by sufficiently long voltage pulses. At higher fields (large in magnitude), the probability of a transverse wall being trapped becomes higher at higher voltage amplitudes. On the other hand, the maximum pulse length where the vortex wall being trapped becomes shorter. It is not clear why transverse walls are trapped at higher fields. Two possible scenarios can be considered, either a transverse wall is nucleated and trapped, or a vortex wall is first nucleated but then is transformed into a transverse wall during its subsequent propagation, and is then trapped.

The vortex wall velocity is estimated from the minimum pulse length needed to drive the DW out from section A-B. In order to determine the minimum pulse length, the pulse length dependence of P_{AB} is fitted to the complementary error function formula, as expressed in Eq. (6.4). Examples of line sections through the probability maps of the vortex wall at fixed voltages are shown in Fig. 6.17 (a-c). Fits to the data using Eq. 6.4 are shown as the blue lines. Note that the times the DW enters section A-B in these plots are slower compared to those in Fig. 6.5. The origin of this difference is not clear, however, since ΔR is measured long after the voltage

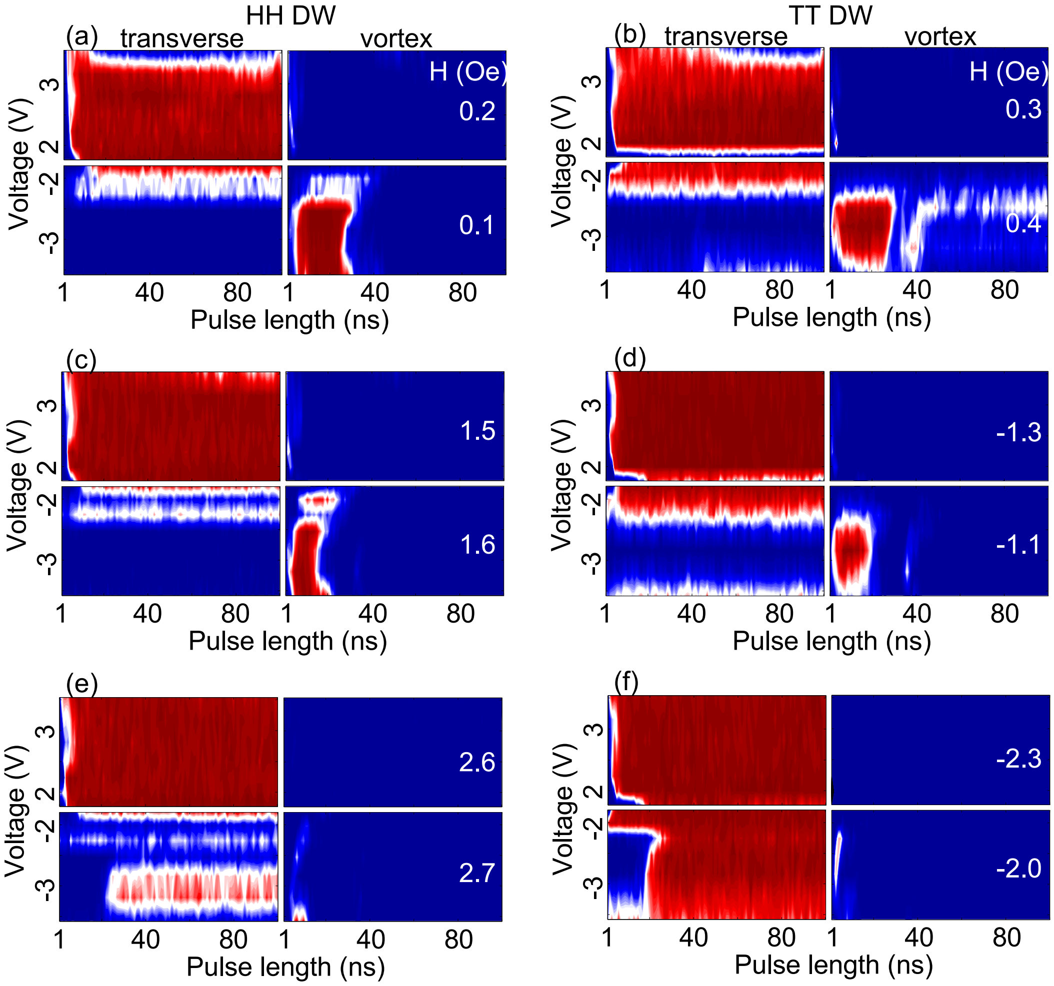

Figure 6.16: (a-f) Injection probability (P_{AB}) maps for transverse walls (left panels) and vortex walls (right panels) plotted against the amplitude and length of the voltage pulse. The color scale represents the probability. The applied magnetic fields are indicated in each panel. The wall types are (a,c,e) HH and (b,d,f) TT walls.

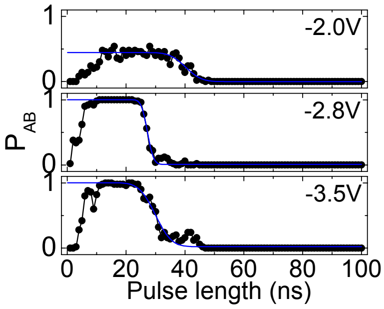

Figure 6.17: Injection probability P_{AB} of a HH vortex wall plotted against the pulse length with various pulse amplitudes, -2.0 V, -2.8 V and -3.5 V. Blue lines are fits to the data using Eq. (6.4).

pulse is injected, the time the DW enters section A-B estimated from the quasi-static measurements (Fig. 6.17) may not represent the true values. Thus it is safer to take the values from Fig. 6.5 for the starting point, which can be approximated as time zero, i.e. set $t_i = 0$ in Eq. (6.6). The dependence of the vortex wall velocity on the pulse amplitude is plotted in Fig. 6.18 for (c) HH and (d) TT DWs, respectively.

In addition, the average probability of the vortex wall being trapped in section A-B (P_{AB}) is plotted as a function of the pulse voltage at different fields in Fig. 6.18 for (a) HH and (b) TT DWs, respectively. These values are taken from the fitting parameter A_1 in Eq. (6.6). Note that this average probability does not represent the probability of current driven DW motion, it is proportional to the number of events that a vortex wall is injected into section A-B.

In each case the velocity increases as the current density is increased to $J \sim -1.5 \times 10^8 A/cm^2$, above which a slight drop is observed. Both HH and TT DWs exhibit similar velocities, indicating that the wall motion is not significantly affected by the self fields created by the voltage pulse.

6.4.2 Time resolved velocity measurements

Thus far, using the quasi-static measurements, we have confirmed that the DW is indeed driven by current over a distance of ~4 μm. The quasi-static measurements

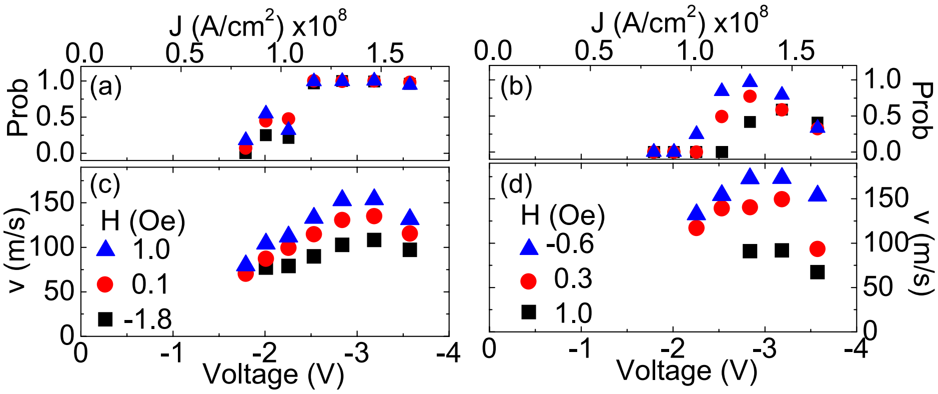

Figure 6.18: (a,b) Probability P_{AB} to inject a (a) HH and (b) TT vortex wall into section A-B of the nanowire. (c,d) Vortex DW velocities for (c) HH and (d) TT DWs plotted against the voltage pulse amplitude with various magnetic fields close to zero. Corresponding current density that flows into the nanowire are shown at the top of each panel.

also indicates that the DW driven by current has a vortex structure. We next study in detail these current driven DW (vortex) motion using the real-time resistance measurements.

The black solid lines in Fig. 6.19 show the signal traces ΔV taken at different fields close to zero for both (a) HH and (b) TT wall. Voltage pulses that are 100 ns long and -2.8 V high are used to inject the DW. The red solid lines are fits to Eq. (6.3) and (6.4). See Fig. 6.4 for the definition of each parameters. For small and zero fields the signal is nearly constant before decreasing, after a time t_f, to zero. At higher fields the signal is more complex. In particular, the signal decreases during the DW's motion along the wire which might be indicative of transformations in the DW state and/or distributions in the DW's velocity. Furthermore, in an intermediate field regime the signal decreases to a non-zero value A_2 (see 4 Oe trace in Fig. 6.19 (a)).

The amplitudes A_1 and A_2 are defined to represent, respectively, the approximate probability of a DW exiting or remaining in section A-B of the nanowire. In general, A_1 and $A2$ can be compared to P_{AB} and P_{AB} in the quasi-static measurements, respectively. A_1 and A_2 are plotted in Fig. 6.20 as a function of the applied field H

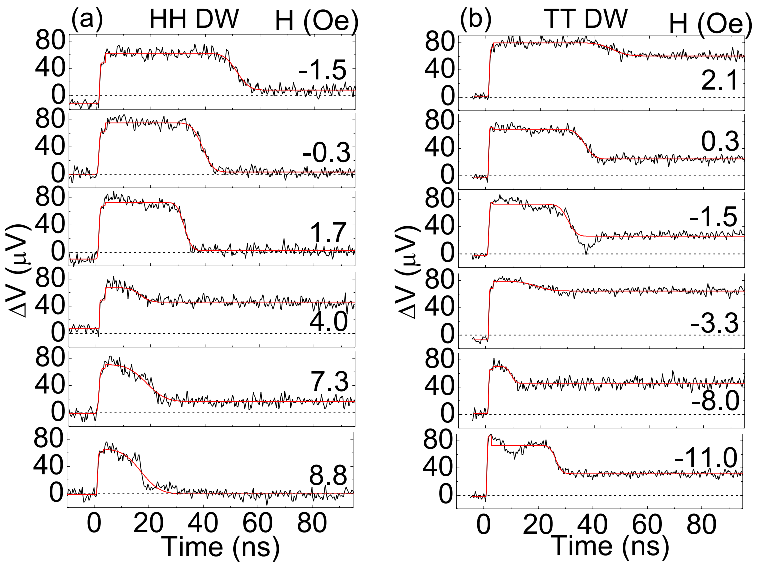

Figure 6.19: Typical signal traces $\Delta V(t)$ for the fields indicated in each panel. The voltage pulse is injected at t=0. A voltage pulse, -2.8 V and 100 ns long, is used to inject (a) HH and (b) TT DW. Corresponding current density that flows into the permalloy nanowire is $\sim -1.4 \times 10^8 A/cm^2$. Solid red lines are fits to the data using Eq. (6.3) and (6.4).

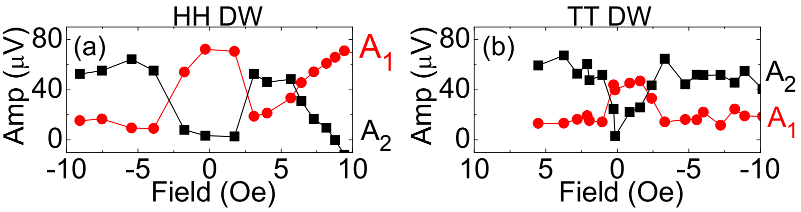

Figure 6.20: Amplitudes A_1 and A_2, defined in Eq. (6.4) (see Fig. 6.4 for details), plotted as a function of the applied field. -2.8 V 100 ns long voltage pulse is used to inject (a) HH and (b) TT DWs. A_1 and $A2$ can be compared to P_{AB} and P_{AB} in the quasi-static measurements, respectively.

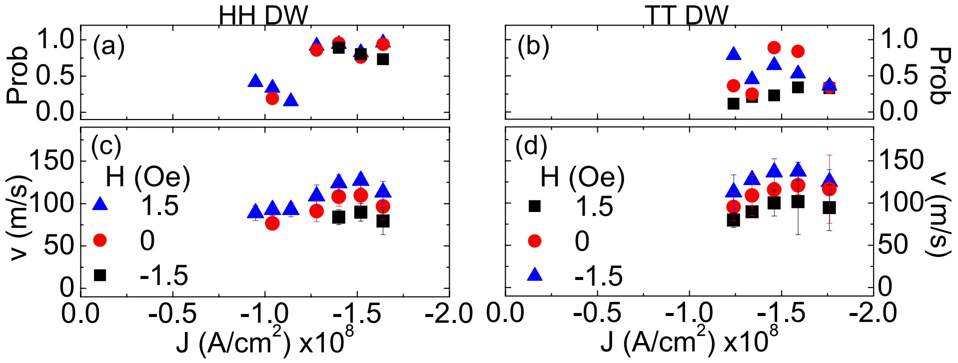

Figure 6.21: (a,b) Probability of (a) HH and (b) TT DWs exiting section A-B, or $\frac{A_2}{A_1+A_2}$ in Eq. (6.4), plotted against the current density flowing through the nanowire at various fields near zero. (c,d) DW velocity near zero field plotted versus the current density. Velocities of (c) HH and (d) TT DWs are shown. Error bars represent $\frac{\Delta\tau v}{\tau}$ in Eq. (6.4), where and v is the DW velocity.

for both (a) HH and (b) TT walls. These data show that the probability of a DW exiting section A-B (proportional to A_1) is high in a narrow field range near zero field, consistent with the quasi-static results, as shown in Fig. 6.14 (c) and (d).

The DW velocity is plotted as a function of current density in Fig. 6.21 for (a) HH and (b) TT DWs at three different fields. The field values are within the field range where A_1 is high. The DW velocity is estimated using Eq. (6.6). In good agreement with the quasi-static results (Fig. 6.18) the DW velocity increases as the current density is increased up to $J \sim -1.5 \times 10^8$ A/cm^2, above which a slight drop is observed. A maximum DW velocity of ∼110 m/s is observed in zero field. A slight drop in the DW velocity at the highest current density is observed both in the quasi-static and the real-time measurements. One possible explanation for the drop may be Joule heating, although the maximum temperature reached is only ∼130K at the highest current density. Another possible explanation is a change in the DW propagation mode analogous to the field induced Walker breakdown phenomenon, as described in Ref. [56].

6.4.3 Velocity of moving DW versus DW at rest

In all these experiments, the DW is injected into the nanowire with the aid of the local field generated around line A. First, it is important to estimate the contribution of the local field on the current driven DW motion. As can be seen in Fig. 3.7, the local field drops rapidly below the propagation field (∼5 Oe) within ∼300-450 nm. This indicates that the DW can travel a maximum distance of ∼450 nm without the aid of current if one assumes that the DW stops moving when the local field is below the propagation field. Thus the net distance the DW travels with current and without the aid of field is minimum ∼3500 nm, roughly 10% shorter than the full distance it travels.

The current driven velocity measured here are much higher than those which were previously reported in permalloy nanowires [36, 38]. It is possible that this discrepancy may be due to differences in the roughness of either the edges or the surfaces of the nanowires, arising from differences in the method of fabrication of the nanowire (lift-off versus ion-milling used here) and the under- and over-layers used here to promote smooth nanowire surfaces.

Another possibility arises since there is a difference in the initial state of the DW. In the previously reported velocities, the DW is initially at rest when the current pulse is applied. On the other hand, here the initial state of the DW is moving when the current pulse is applied due to the local field. Thus it is interesting to study whether a DW initially moving, due to the aid from the local fields, or initially at rest will have a different velocity when driven by current. Again, quasi-static measurements are performed to investigate this point.

The experiments carried out are basically the same as those described in Chapter 5. Figure 6.22 shows the SEM image of the nanowire with the experimental setup laid on. A pulse generator (PG-B1, Picosecond pulse labs, model 10300B) is connected to line A to generate the local field so as to inject a DW into section A-B. Another pulse generator (PG-B2, Picosecond pulse labs, model 10300B) is connected to line B via a bias tee. This pulse generator is used inject a current pulse into the nanowire, which may result in driving the DW out from section A-B. The nanowire width is 300 nm and no pinning centers (notches) are patterned along the nanowire.

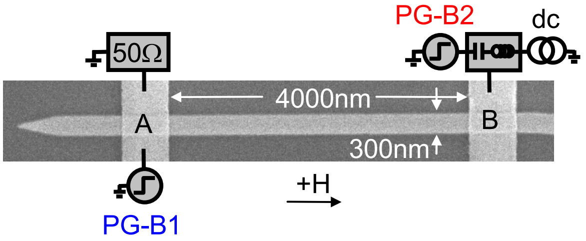

Figure 6.22: SEM images of the device with illustrations of the measurement circuit. Labels A and B are for the contact lines. The box labeled dc includes both a current source and a voltmeter connected in parallel.

The configuration shown in Fig. 6.22 can create a head to head (HH) wall in section A-B when a negative voltage pulse is injected from PG-B1. Negative pulses can push the DW towards line B (see Fig. 6.14 (c)). The amplitude of this voltage pulse is set to -2.8 V. No magnetic fields are applied during the injection process, i.e. $H \sim 0$. By varying the length of this injection voltage pulse, we can control the position of the DW within section A-B, assuming that the DW velocity is constant throughout the pulse application. The state of the DW, whether vortex or transverse, is studied by measuring the resistance level (ΔR_i) of the nanowire.

A second voltage pulse is then generated from PG-B2 to inject a current pulse into the nanowire. The amplitude and length of this voltage pulse is varied. Again, no magnetic fields are applied during the pulse application. The resistance level of the nanowire (ΔR_f) is measured after the pulse to study whether the DW is driven out from section A-B. This process of injecting a DW with the first pulse and attempting to move it with the second pulse is repeated 50 times to obtain the probability of DW motion. Since the second pulse is applied 90 ms after the first pulse, it is reasonable to assume that the DW is at rest when the second pulse hits the DW.

The probability maps of moving the vortex wall with current pulses are plotted in Fig. 6.23 as a function of first and second voltage pulse length. We define the pulse length of the first and second voltage pulses as t_1 and t_2, respectively. Maps are plotted for various amplitudes of the second voltage pulse, where the amplitudes are indicated on top of each map. Ideally, the vertical axis is proportional to the distance

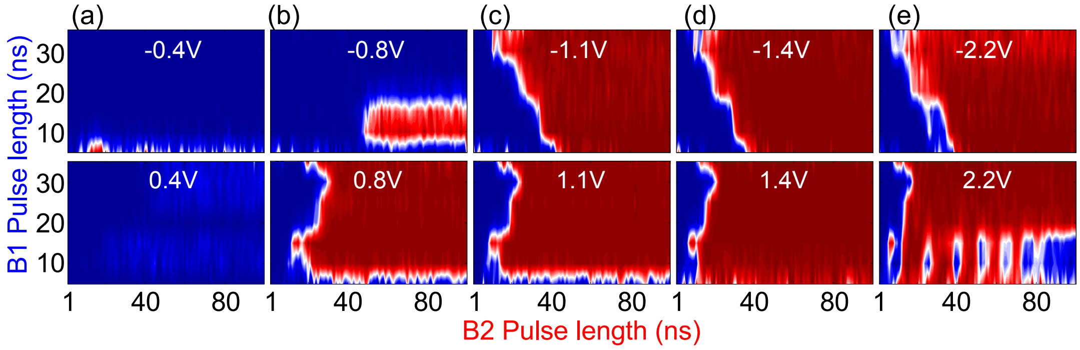

Figure 6.23: (a-e) Probability maps of a HH vortex wall exiting section A-B plotted against the lengthes of the first and second voltage pulse. The amplitude of the first pulse is -2.8 V and that of the second pulse is indicated in each panel.

the DW travels with the first injection pulse. The lateral axis then represents the time needed to move the DW out from section A-B. With regard to the second voltage pulse, positive pulses drive the DW towards line B, whereas negative pulses push the DW towards line A, according to spin transfer torque. The direction of the electron flow is shown in Fig. 6.24 for positive (a) and negative (b) voltage pulses from PG-B2. When the amplitude of the second voltage pulse exceeds ±0.8 V, transitions in the probability from 0 (blue) to 1 (red) are clearly observed. This indicates that the DW at rest indeed can be moved with current.

For positive pulses, the transition point occurs for shorter t_2 when t_1 is increased. Since the first pulse and the second pulse drives the DW in the same direction, we expect the DW to leave from line B-end. In Fig. 6.24 (a), the transition points in the maps are plotted for various (second) pulse amplitudes. The relationship between t_1 and t_2 in this figure is linear, indicating that the DW velocity is constant during the current pulse application.

For negative pulses, the opposite behavior is observed; as t_1 is increased, it requires longer t_2 to move the DW out. This is consistent with the picture that the first pulse drives the DW toward line B and the second one pushes it back to line A. Thus it is expected that the DW exits from line A-end. Fig. 6.24 (b) plots the transition points in the maps for various (second) pulse amplitudes. The t_1-t_2 relationship is

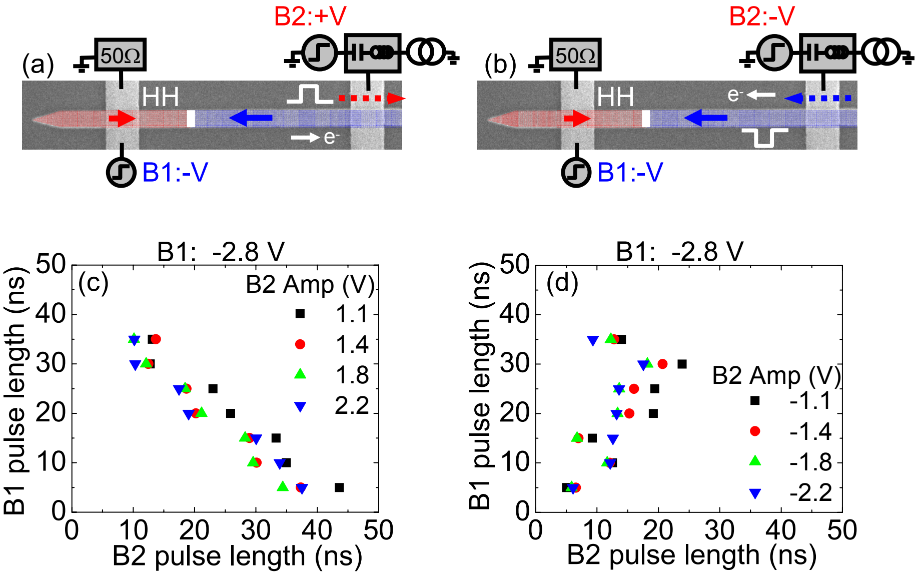

Figure 6.24: (a,b) SEM images of the device with illustrations of the measurement circuit. The colored thick arrows indicate the magnetization direction of the nanowire. Dashed colored arrows on the right side show the direction of the local field generated by the current passing through line B. The voltage pulse injected from line B is (a) positive and (b) negative polarity. The directions of the electron flow are shown by white arrows. (c,d) The pulse length needed to complete a HH vortex wall to move out from section A-B when the amplitude of the first voltage pulse is (c) -2.8 V and (d) 2.8 V. Data from various amplitudes of the second pulse are plotted.

not as clear as that shown in (a), however, it is clear that the trend is opposite. The oscillations in the probability observed when -2.2 V voltage pulses are injected to move the DW out may be due to the local field generated at line A when the second voltage pulse is applied.

These observation are consistent with spin transfer torque driven DW motion and agrees with the assumption that the DW velocity is constant during the current pulse application.

6.5 Analytical analysis using the 1D model

6.5.1 Model description

The one dimensional (1D) model can be used to interpret the dynamics of a domain wall (DW) motion. The objective of this section is to derive an analytical form for the DW velocity. We start from the differential Eqs. (2.29) and (2.30) introduced in Chapter 2. In this chapter, we study the case where no local pinning center exists along the nanowire, i.e. DW motion in an ideal nanowire. The pinning parameter is therefore set to zero ($p = 0$) in Eq.(2.29) and (2.30). The transverse field terms are also neglected, i.e. $a_x = 0$ and $a_z = 0$. To simplify the equations, we introduce two new parameters that are constant (time independent), $b_1 = a + \beta v + v/\alpha$ and $b_2 = a + \beta v - \alpha v$. Thus Eq.(2.29) and (2.30) can rewritten as,

$$(1+\alpha^2)\dot{x} = \alpha b_1 + \sin 2\psi \tag{6.7}$$

$$(1+\alpha^2)\dot{\psi} = b_2 + \alpha \sin 2\psi \tag{6.8}$$

6.5.2 Stability of DW motion

We first study the field driven motion of DWs. In order to obtain an intuitive picture of how the DW travel along a ideal nanowire, the differential equations (6.7) and (6.8) are solved numerically. Figure 6.25 shows the numerically calculated temporal evolution of the position and angle of a DW. Magnetic field of (a) 4 Oe, (b) 10 Oe and (c) 20 Oe are applied. Current is set to zero in the calculation. At small fields,

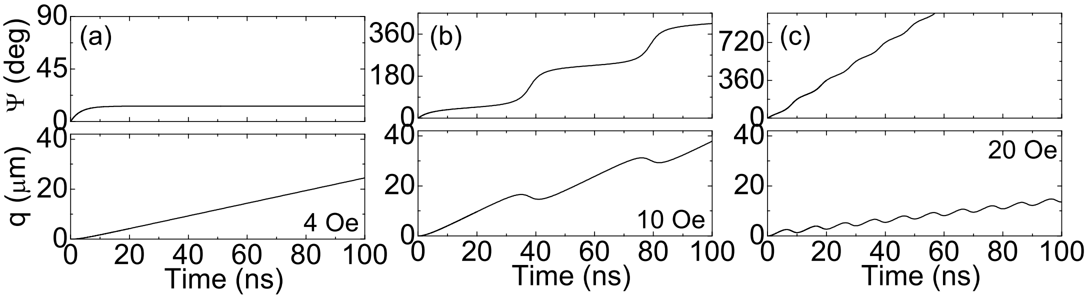

Figure 6.25: (a-c) Numerical calculation results showing the temporal evolution of the angle (top panels) and the position (bottom panels) of the DW. The applied magnetic field is indicated at the bottom right of each panel. Note that the scale of the angle is different for each panel. The parameters used are: H_K=1800 Oe, Δ=36 nm, α=0.01, β=0, u=0.

the position of the wall increases linearly with time and the angle saturates at long time. On the other hand, at high fields, the position as well as the angle periodically oscillates with time. The transition from linear time dependence to oscillatory time dependence of the DW position indicates change in the stability of the solutions of Eqs. (6.7) and (6.8).

To gain insights into the field driven DW motion, we use the linear stability theory to first analyze Eqs.(6.7) and (6.8). By rearranging Eqs.(6.7) and (6.8), we define functions $f(x,\psi)$ and $g(x,\psi)$ as

$$\dot{x} = \frac{1}{1+\alpha^2}(\alpha b_1 + \sin 2\psi) \equiv f(x,\psi) \tag{6.9}$$

$$\dot{\psi} = \frac{1}{1+\alpha^2}(b_2 + \alpha \sin 2\psi) \equiv g(x,\psi). \tag{6.10}$$

The above two differential equations are assumed to have equilibrium solutions (x_e, ψ_e), i.e. $f(x_e,\psi_e) = \dot{x_e} = 0$ and $g(x_f,\psi_f) = \dot{\psi_e} = 0$. A small perturbation $(u \ll 1, v \ll 1)$ is applied around the equilibrium solution to examine the stability of (x_e,ψ_e). Substituting $(x,\psi) = (x_e + u, \psi_e + v)$ into Eq.(6.9) and (6.10) gives $f(x_e + u, \psi_e + v) = \dot{u}$ and $g(x_e + u, \psi_e + v) = \dot{v}$. Note that since x_e and ψ_e are equilibrium solutions, $\dot{x_e} = 0$ and $\dot{\psi_e} = 0$. Expanding $f(x_e + u, \psi_e + v)$ and $g(x_e + u, \psi_e + v)$ around (x_e,ψ_e) and

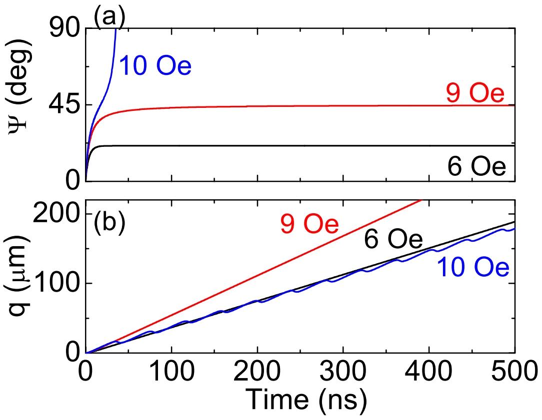

Figure 6.26: Numerical calculation results showing the temporal evolution of the angle (a) and the position (b) of the DW. The applied magnetic field is indicated for each colored line. The parameters used are: H_K=1800 Oe, Δ=36 nm, α=0.01, β=0, u=0.

keeping terms that are linear in u or v gives

$$\dot{u} = f(x_e + u, \psi_e + v) \simeq \frac{2}{1+\alpha^2}\cos(2\psi_e)v \tag{6.11}$$

$$\dot{v} = g(x_e + u, \psi_e + v) \simeq -\frac{2\alpha}{1+\alpha^2}\cos(2\psi_e)v \tag{6.12}$$

The differential equations (6.11) and(6.12) can be solved exactly. In order to have solutions that do not diverge, $\cos(2\psi_e) > 0$ in Eq. (6.12). This sets the stability condition for (x_e, ψ_e), that is,

$$-\frac{\pi}{4} \pm \frac{n\pi}{2} \leq \psi_e \leq \frac{\pi}{4} \pm \frac{n\pi}{2} \tag{6.13}$$

where n is an integer. In other words, instability occurs when ψ_e takes values that are out of the range shown in Eq. (6.13). The saddle point ψ_e^* is therefore given by

$$\psi_e^* = \frac{\pi}{4} \pm \frac{n\pi}{2}. \tag{6.14}$$

To illustrate the instability that occurs when ψ exceeds ψ_e^*, Fig. 6.26 shows the

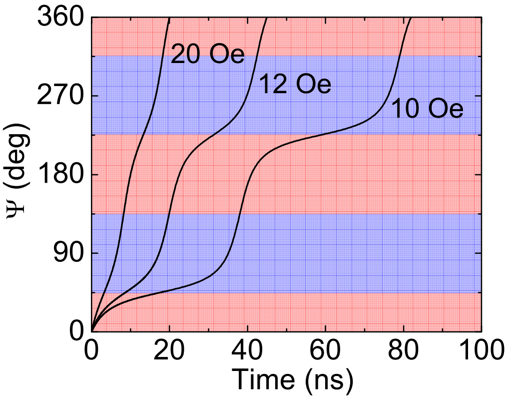

Figure 6.27: Numerical calculation results showing the temporal evolution of the angle of the DW. The applied magnetic field is indicated for line. The background colors represent the stability of the angle, red and blue represent stable and unstable angles, respectively. The parameters used are: H_K=1800 Oe, Δ=36 nm, α=0.01, β=0, u=0.

numerically calculated temporal evolution of the angle and position of a DW at three different fields. When the angle ψ is below 45 deg, i.e. below the stability range shown in Eq. (6.13), the angle saturates and the position increases linearly with time. As soon as ψ exceeds 45 degree, the angle rapidly increases and the position oscillates with time (see the blue solid lines). Figure 6.27 shows the numerically calculated temporal evolution of the position of a DW at another three different fields. At these fields, the position oscillates with time. The stabile and unstable region of ψ values from Eq. (6.13) are shown in Fig. 6.27 as red and blue background colors, respectively. The boundaries between the red and blue regions represent the saddle points. It is clear that in all cases, the saddle point is the same regardless of the magnitude of the field.

From Fig. 6.26, the instability occurs when the magnetic field is above 10 Oe. To find the this critical field, ψ_e is substituted into Eq.(6.8). Using $\dot{\psi}_e = 0$, values of b_2 that correspond to stable ψ_e, as shown in Eq. (6.13), are expressed as

$$\alpha \geq b_2 \geq -\alpha. \tag{6.15}$$

When b_2 takes value outside the range shown above, instability occurs in the solution.This is also apparent from Eq. (6.8) since $\sin 2\psi$ cannot take values larger than 1 and smaller than -1. Substituting the original parameters gives

$$\alpha - (\beta - \alpha)v \geq a \geq -\alpha - (\beta - \alpha)v \tag{6.16}$$

which shows the fields within the stability range. The field at which the instability occurs is called the Walker breakdown field. The equal sign in Eq. (6.16) represents the saddle point in a, which is equal to the Walker breakdown field,

$$a_{WB} = \alpha + (\alpha - \beta)v \tag{6.17}$$

6.5.3 Field driven DW velocity

Next we look for the time average DW velocity $< \dot{x} >$. We start from Eq.(6.8) since it only contains one variable, ψ. This differential equation can be solved exactly by integration. However, one needs to assume $b_2 - \alpha \sin(2\psi) \neq 0$ to do the integration. In the instability range ($b_2 > \alpha$), this condition will automatically be satisfied. Thus we start from the integrating Eq.(6.8) assuming $b_2 > \alpha$. Direct integration gives

$$\psi(\tau) = \arctan\left(\frac{1}{b_2}(\alpha - \sqrt{b_2^2 - \alpha^2}\tan(\frac{\sqrt{b_2^2 - \alpha^2}}{1 + \alpha^2}\tau + C_0))\right) \tag{6.18}$$

where C_0 is a constant. Since ψ periodically evolves in the instability regime, we calculate the time needed to change ψ for one cycle. In Fig. 6.27, in order to complete one cycle, ψ has to go through one stable (red region) and one unstable (blue region) regime, which adds up to 180 degree. The period $\Delta\tau$ of $\psi(\tau)$ to complete one cycle can be estimated by, for example, calculating the time needed to change ψ from $-\frac{\pi}{2}$ to $\frac{\pi}{2}$. Substituting $\psi = \pm\frac{\pi}{2}$ into Eq. (6.18) gives

$$\Delta\tau = \pm\pi\frac{1 + \alpha^2}{\sqrt{b_2^2 - \alpha^2}} \tag{6.19}$$

where the ± sign stands for $b_2 > 0$ (+) and $b_2 < 0$ (−). The periodic change in ψ is associated with the oscillation in the position of the DW (see Fig. 6.25 (b)). The change in the position (Δx) when ψ completes one cycle can be estimated from Eq. (6.7). Equation (6.7) is integrated using the substitution $\sin(2\psi) = \frac{1}{\alpha}(b_2 - (1+\alpha^2)\dot{\psi})$ from Eq. (6.8). The integration limit is taken from $\tau = \tau_1$ to $\tau = \tau_2$, where $\tau_{1(2)}$ are defined, respectively, as the start and end time of one cycle, or $\Delta\tau = \tau_2 - \tau_1$. The result is

$$\Delta x \equiv x(\tau_2) - x(\tau_1) = \frac{\alpha b_1 + b_2/\alpha}{1+\alpha^2}(\tau_2 - \tau_1) - \frac{1}{\alpha}\left(\psi(\tau_2) - \psi(\tau_1)\right). \tag{6.20}$$

$\Delta\tau$ can be substituted from Eq. (6.19) into $(\tau_2 - \tau_1)$. Note that, by definition, $\psi(\tau_2) - \psi(\tau_1) = \pi$. Thus the distance the DW travels when ψ changes over 180 degree is,

$$\Delta x = \pi\frac{\alpha b_1 + b_2/\alpha}{\sqrt{b_2^2 - \alpha^2}} - \frac{\pi}{\alpha}. \tag{6.21}$$

In order to obtain the average DW velocity $< \dot{x} >$, we divide Equation (6.21) with $\Delta\tau$, or with Eq. (6.19). The result is

$$\begin{aligned} < \dot{x} > &= \frac{\Delta x}{\Delta\tau} = \frac{\alpha b_1 + b_2/\alpha}{1+\alpha^2} \mp \frac{\sqrt{b_2^2 - \alpha^2}}{\alpha(1+\alpha^2)}. \\ < \dot{x} > &= \frac{1}{\alpha}(a + \beta v) \mp \frac{\sqrt{(a + \beta v - \alpha v)^2 - \alpha^2}}{\alpha(1+\alpha^2)} \end{aligned} \tag{6.22}$$

where the ∓ sign stands for $b_2 > 0$ (−) and $b_2 < 0$ (+). This is the time averaged DW velocity above the Walker breakdown limit.

We next look for the average DW velocity below the breakdown limit, i.e. when $b_2 \leq \alpha$. In Eq.(6.8), as long as $b_2 - \alpha\sin(2\psi) \neq 0$, we can directly integrate this differential equation. We first examine the case when $b_2 - \alpha\sin(2\psi) = 0$. Substituting $\sin(2\psi) = b_2/\alpha$ from Eq.(6.8) into Eq.(6.7) gives an expression for $\dot{x}$. As seen in Fig. 6.26 (a), when the field is below the breakdown limit, the velocity of the DW, or the slope of the position versus time curve, is constant. Thus the time averaged DW

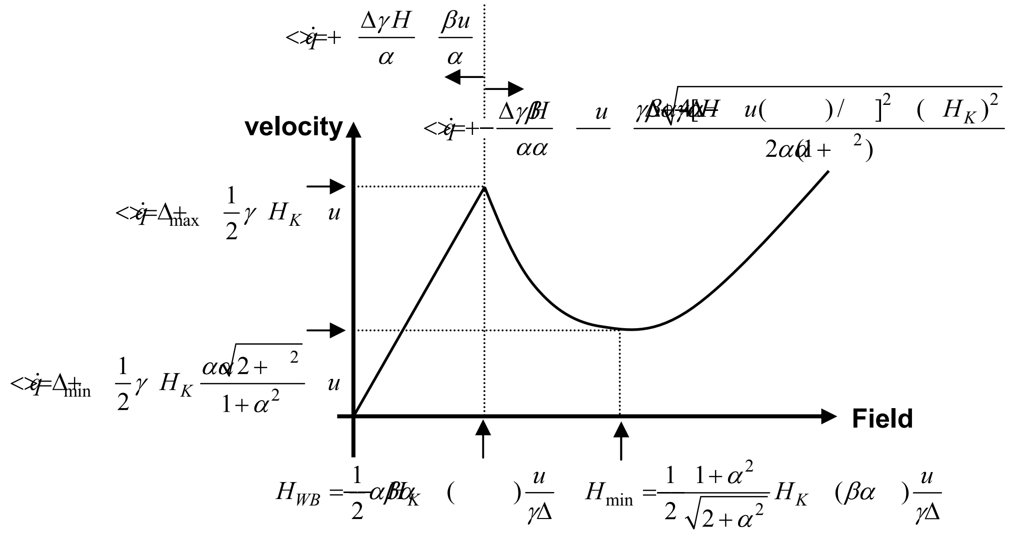

Figure 6.28: Analytical solutions of the 1D model showing the dependence of DW velocities on the magnetic field.

velocity equals the instantaneous DW velocity, which gives

$$< \dot{x} >= \frac{\alpha b_1 + b_2/\alpha}{1+\alpha^2} \tag{6.23}$$

When $b_2 - \alpha \sin(2\psi) \neq 0$, we can directly integrate Eq.(6.8). The solution is the same as that shown in Eq.(6.18), however, the number inside the square roots are now negative, meaning that we have imaginary numbers in the solution. From Fig.6.26 (a), we know that when $b_2 \leq \alpha$, or when we are below the breakdown limit, $\psi(\tau)$ approaches an equilibrium value ψ_e at the long time limit. This value can be found by setting $\tau \to \infty$ in Eq.(6.13), which gives

$$\psi(\tau \to \infty) = \psi_e = \arctan(\frac{\alpha + \sqrt{\alpha^2 - b_2^2}}{b_2}) \tag{6.24}$$

Substituting ψ_e into Eq.(6.7) provides and expression for $\dot{x}$, which turns out to be the same formula as Eq.(6.23).

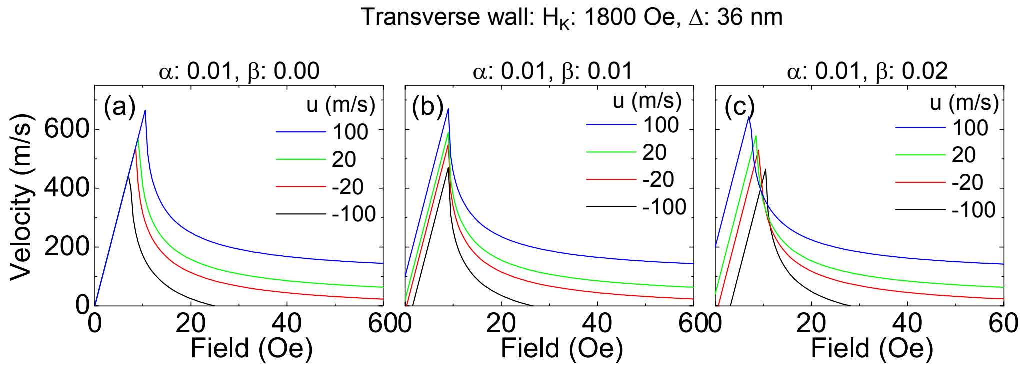

Figure 6.29: Numerical calculations of the DW velocity when various amplitudes of current (u) is passed. The size of β is changed for each panel. The parameters used describe a transverse wall in a 300 nm wide 10 nm thick permalloy nanowire. H_K=1800 Oe, Δ=36 nm, α=0.01, (a) β=0, (b) β=0.01, (b) β=0.02.

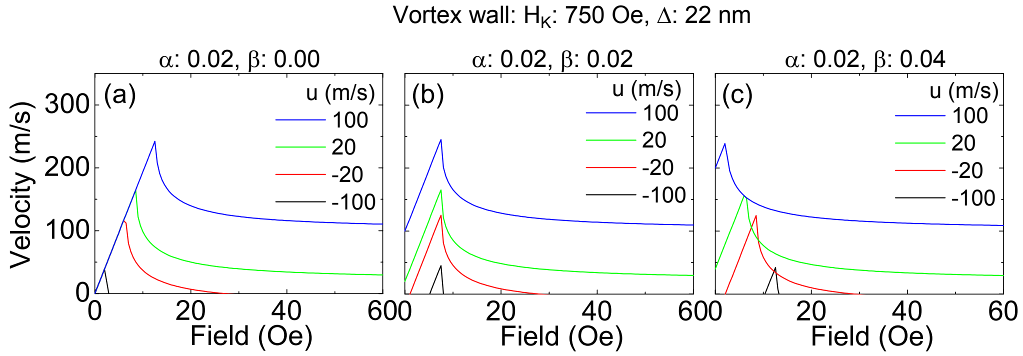

Figure 6.30: Numerical calculations of the DW velocity when various amplitudes of current (u) is passed. The size of β is changed for each panel. The parameters used describe a vortex wall in a 300 nm wide 10 nm thick permalloy nanowire. H_K=750 Oe, Δ=22 nm, α=0.02, (a) β=0, (b) β=0.02, (b) β=0.04.

We have thus obtained the time averaged DW velocity in the entire field range. A summary of the dependence of DW velocities on the magnetic field are shown in Fig. 6.28. Numerical calculation results are shown in Fig. 6.29 and 6.30 for two different sets of parameters, i.e. one for a transverse wall and the other for a vortex wall.

6.5.4 Current driven DW velocity

Current driven DW velocity can be treated within the same framework of field driven velocity. As derived in Eq. (6.13), instability occurs when $b_2 = \alpha$. In terms of current, stable solutions exist when

$$\frac{\alpha - a}{\beta - \alpha} \geq v \geq -\frac{\alpha - a}{\beta - \alpha}. \tag{6.25}$$

The saddle point for the current, or the Walker breakdown current, is

$$v_{WB} = \pm\frac{\alpha - a}{\beta - \alpha}. \tag{6.26}$$

The expression of the DW velocities are the same as that shown in Eq. (6.22) when $v > v_{WB}$ and Eq. (6.23) when $v < v_{WB}$. A summary of the analytical solutions to Eq. (2.29) and (2.30) are shown in Fig. 6.31, where the dependence of the DW velocity on current at zero field is shown. Numerical calculation results are shown in Fig. 6.29 and 6.30 for two different sets of parameters, i.e. one for a transverse wall and the other for a vortex wall.

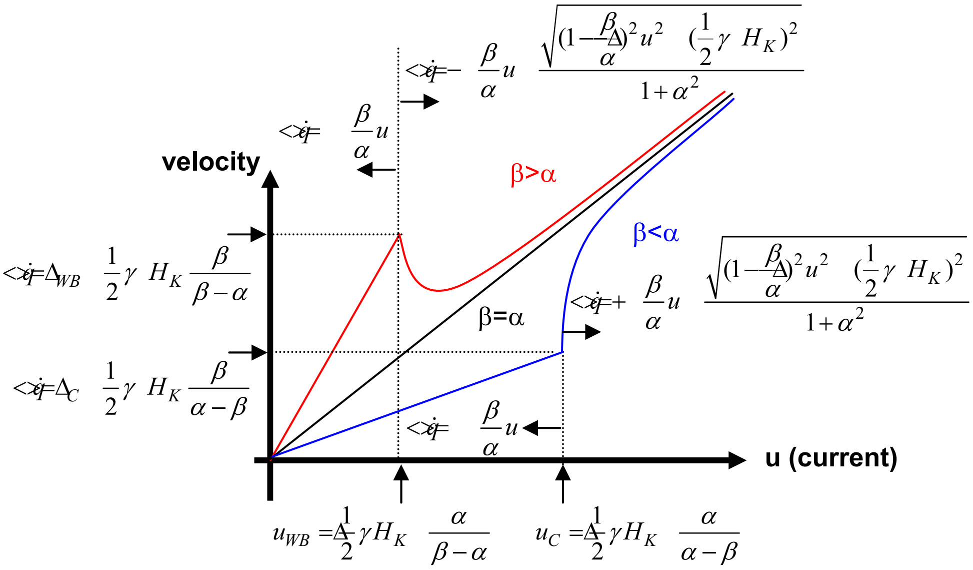

Figure 6.31: Analytical solutions of the 1D model showing the dependence of DW velocities on the current (spin torque parameter u).

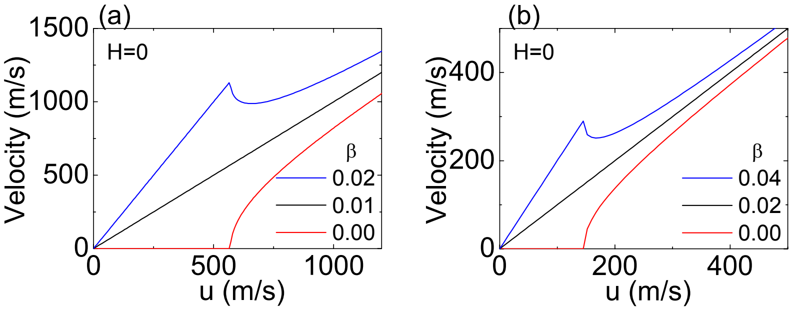

Figure 6.32: Numerical calculations of the DW velocity plotted against the spin torque parameter u. The size of β is changed for each curve. The magnetic field is set to zero. The parameters used describe (a) transverse wall (H_K=1800 Oe, Δ=36 nm, α=0.01) and (b) vortex wall (H_K=750 Oe, Δ=22 nm, α=0.02) in a 300 nm wide 10 nm thick permalloy nanowire.

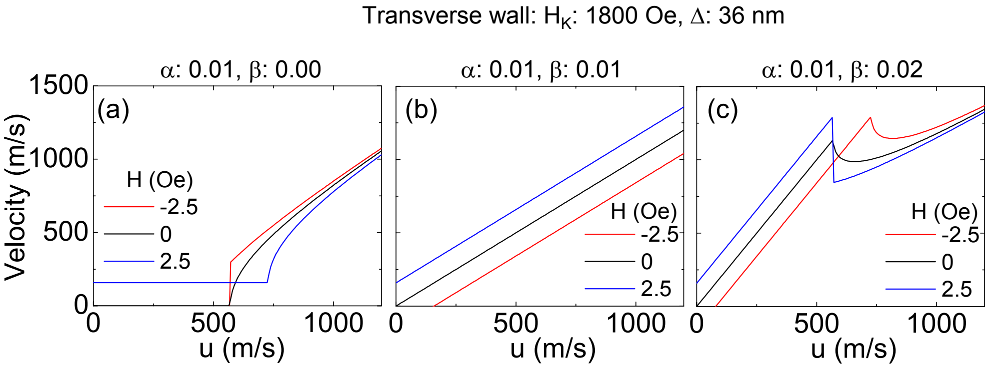

Figure 6.33: Numerical calculations of the DW velocity plotted against the spin torque parameter u. The size of β is changed for each panel. Colors represent different magnetic fields. The parameters used describe a transverse wall in a 300 nm wide 10 nm thick permalloy nanowire. H_K=1800 Oe, Δ=36 nm, α=0.01, (a) β=0, (b) β=0.01, (b) β=0.02.

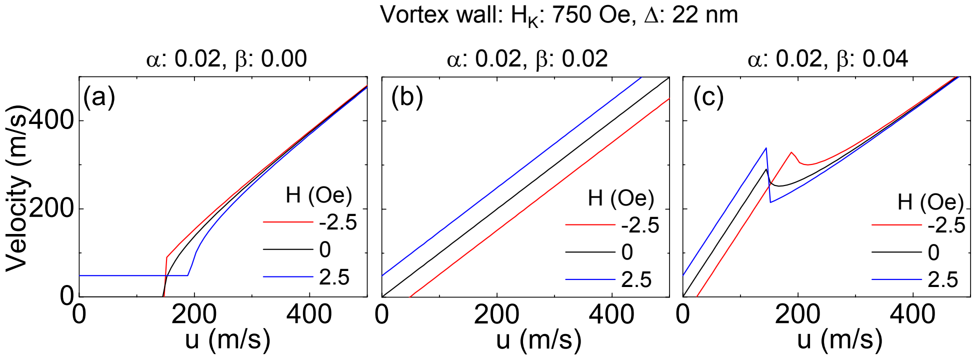

Figure 6.34: Numerical calculations of the DW velocity plotted against the spin torque parameter u. The size of β is changed for each panel. Colors represent different magnetic fields. The parameters used describe a vortex wall in a 300 nm wide 10 nm thick permalloy nanowire. H_K=750 Oe, Δ=22 nm, α=0.02, (a) β=0, (b) β=0.02, (b) β=0.04.

Correct Fig. 6.28 and Fig. 6.32.

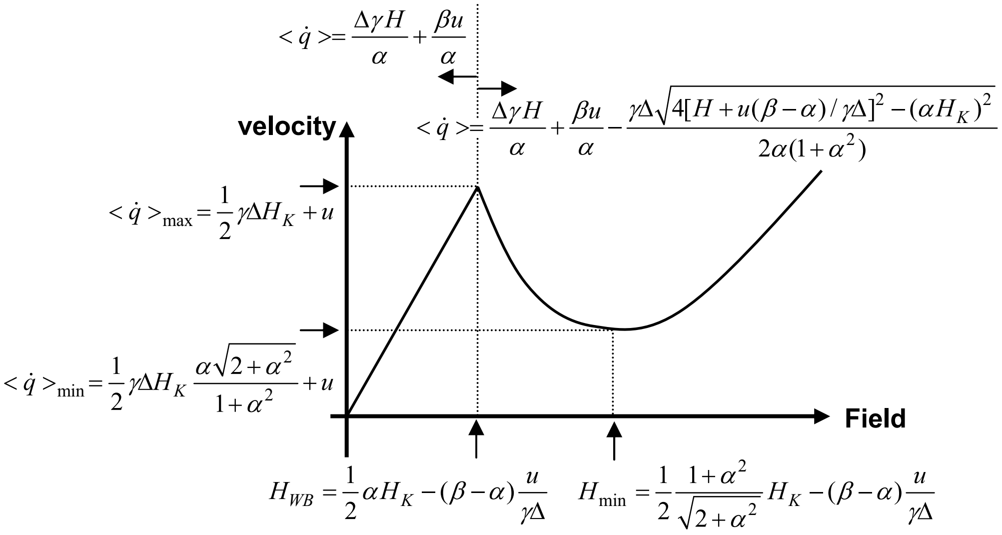

FIG. 1: Fig. 6.28: Analytical solutions of the 1D model showing the dependence of DW velocities on the magnetic field.

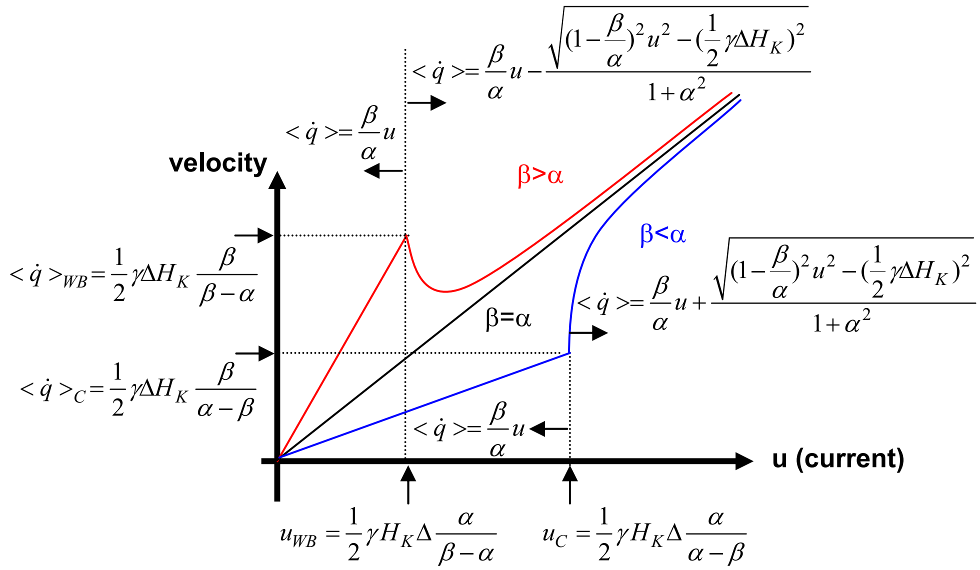

FIG. 2: Fig. 6.32: Analytical solutions of the 1D model showing the dependence of DW velocities on the current (spin torque parameter u).

6.6 Discussion

6.6.1 Size of the non-adiabatic spin torque term

The presence/absense of the non-adiabatic spin transfer torque (β in the 1D model) is attracting increasing interest due to its unique contribution to the DW velocity. One possible method to estimate the size of β is to study the current dependence of the Walker breakdown field. From Eq. 6.17, the change in the Walker breakdown field is proportional to the magnitude of the current that flows in the nanowire. When $\beta = \alpha$, the breakdown field becomes independent of the current. This is what is observed experimentally in Fig. 6.9 (a). Although the error bars are relatively large in this plot, the breakdown field shows little dependence on the current density. Since the structure of the DW that causes the breakdown is not clear in the experiments, data from Fig. 6.7 should be compared to both Fig. 6.29 (transverse wall) and Fig. 6.30 (vortex wall). Roughly speaking, it can be assumed that $\beta \sim \alpha$ from the comparison.

6.6.2 Comparison of current driven DW velocity to the electron drift velocity

The maximum current driven DW velocity observed is $\sim$ 110 m/s at the current density of 1.5×10^8 a/cm^2 (see Section 6.4 for details). It is interesting to first compare this velocity to the rate at which spin angular momentum is transferred from the electrons to the local moments. Although the arguments is rather hand-waving, it provides insight into current driven DW motion.

Assuming the g-factor (g) of the conduction electrons in permalloy being 2, the angular momentum that one electron possesses is $g\mu_B S \approx \mu_B$, where $S = 1/2$ is the electron spin and μ_B is the Bohr magnetron. When the electrons are moving with a drift velocity of v_d, the angular momentum that crosses an unit area in one second is $A_e \equiv v_d n_e \mu_B$, where n_e is the electron density.

The magnetic moment that an atom carries is defined as $X\mu_B$, where X is the net moment per atom in Bohr magnetron units. The magnetic moment per unit area is $A_a \equiv a n_a X \mu_B$, where a is the lattice constant and n_a is the atomic concentration.

The rate of transferring angular momentum from the electrons to one atom can therefore be expressed as

$$r \equiv \frac{A_e}{A_a} = \frac{v_d n_e}{a n_a X} \tag{6.27}$$

From Drude's model,

$$J = n_e e v_d = \sigma E \tag{6.28}$$

where J is the current density, σ is the conductivity and E is the electric field. In the two current model, the conductivity of the majority and minority spins are assumed to be different. The spin polarization of the current P is defined as

$$P = \frac{\sigma^{\uparrow} - \sigma^{\downarrow}}{\sigma^{\uparrow} + \sigma^{\downarrow}}. \tag{6.29}$$

where $\sigma^{\uparrow(\downarrow)}$ represents the conductivity of the majority (minority) spin. In terms of the drift velocity, Eq. (6.29) can be rearranged to read

$$v_d^{\uparrow} = \frac{1+P}{2}\frac{J}{e n_e^{\uparrow}} \tag{6.30}$$

$$v_d^{\downarrow} = \frac{1-P}{2}\frac{J}{e n_e^{\downarrow}}. \tag{6.31}$$

where $v_d^{\uparrow(\downarrow)}$ represents drift velocity of the majority (minority) spin. The two current model assumes that conduction channel of the majority and minority spins are separated. The Kirchoff law then reads

$$J = J^{\uparrow} + J^{\downarrow}, \tag{6.32}$$

where $J^{\uparrow(\downarrow)}$ is the current contribution of the majority (minority) spin and the current flow is assumed to be homogenous in the material. Equation (6.32) can be rearranged to read

$$n_e v_d = n_e^{\uparrow} v_d^{\uparrow} + n_e^{\downarrow} v_d^{\downarrow} \tag{6.33}$$

Substituting Eq. (6.33), (6.30) and (6.31) into Eq. (6.27) gives

$$r = \frac{J}{ean_a X}. \tag{6.34}$$

Note that in Eq. (6.34) the spin polarization of the current has vanished. This is because the two current model was not included in Eq. (6.27). To include, $A_e = v_d^{\uparrow} n_e^{\uparrow} \mu_B$ should be substituted into Eq. (6.27). Then Eq. (6.34) is replaced by

$$r = \frac{1+P}{2} \frac{J}{ean_a X}. \tag{6.35}$$

Since rate r represents the inverse of the time one atom needs to flip its moment, the product ra will provide the velocity of changing the atomic moments' direction, which can be compared to the DW velocity. Note that the velocity ra is exactly equivalent to the spin torque term u in the 1D model. Substituting the atomic density of permalloy $n_a \approx 8.975 \times 10^{22}$ cm^{-3} and the moment per atom $X \approx 0.9$ into Eq. (6.35), the velocity $ra \sim 35J(1+P)$ m/s . At the current density of $J \sim 1.5 \times 10^8$ A/cm^2, the current density where the maximum DW velocity was observed, $ra \sim 105$ m/s at $P = 1$, comparable to the DW velocity observed experimentally ($v \sim$110 m/s). However, if a more realistic value of P is used ($P \sim 0.4 - 0.9$ [127, 104, 128]), the rate of spin angular momentum transfer becomes slower than the DW velocity. In addition, Eq. (6.35) does not include any loss of the angular momentum transfer process, i.e. the efficiency is assumed to be 100%. Thus it is likely that processes other than the angular momentum transfer are contributing to the DW velocity, such as the linear momentum transfer process [50, 94].

The linear momentum transfer is naively characterized by the parameter β in the 1D model. The DW velocity below the breakdown ($b_2 < \alpha$) is expressed as $< \dot{x} >= \frac{\beta}{\alpha} u$ in the absence of magnetic field. Thus if the factor $\frac{\beta}{\alpha}$ becomes larger than 1, the DW velocity exceeds the rate of spin angular momentum transfer u.

Finally, the DW velocity is compared to the drift velocity of the electrons. In the two current model, if it is assumed that only the majority electrons contribute to the angular (and linear) momentum transfer process, Eq. (6.33) can be approximated as

$$n_e v_d \approx \frac{1}{2} n_e v_d^{\uparrow} \tag{6.36}$$

where the electron density of the majority electrons are assumed to be half of the total electron density. Substituting this equation into the Drude's model, Eq. (6.28), gives the expression for the majority electrons drift velocity

$$v_d^{\uparrow} \approx \frac{2J}{n_e e}. \tag{6.37}$$

The electron density in permalloy can be estimated from Hall measurements. Fig. 6.35 (a) shows a typical Hall voltage plotted against the out of plane magnetic field in permalloy Hall bars. Due to the anomalous Hall effect, the slope of the Hall voltage versus field at high field does not represent the normal Hall resistance. In order to obtain the normal Hall resistance, the slope at high field for both positive and negative fields are subtracted to remove the contribution from the anomalous Hall effect. The estimated electron densities are plotted in Fig. 6.35 (b) as a function of thickness of the permalloy film. Data from Ref. [23] are shown together. The dashed line is the expected electron density from the Drude's model, $n_e \approx n_a$, where $n_a \approx 8.975 \times 10^{22}$ cm^{-3} is the atomic density. One conduction electron per atom is assumed. The measured electron density is nearly half of that of the prediction from the Drude's model. Substituting $n_e \sim 5 \times 10^{22}$ cm^{-3} and $J \sim 1.5 \times 10^{8}$ A/cm^2 gives $v_d^{\uparrow} \sim 375$ m/s, more than three times faster than the DW velocity. The drift velocity will provide an upper limit on the current induced DW velocity.

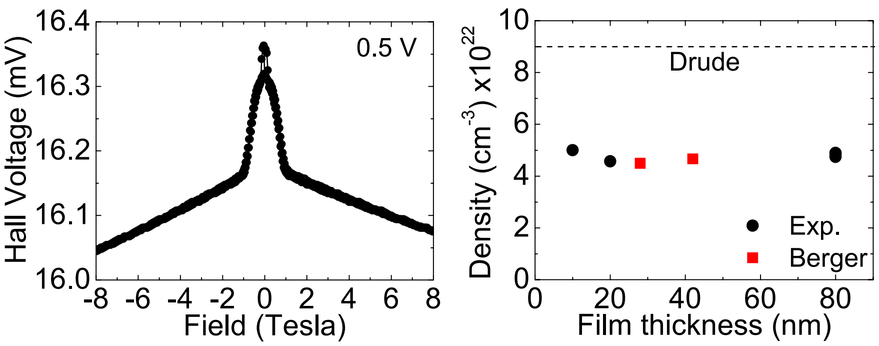

Figure 6.35: (a) Hall voltage measured for a 10 nm thick permalloy Hall bar. 0.5 V is applied along the Hall bar. (b) Electron density of permalloy, estimated from the Hall resistance measurements (black circles) are plotted as a function of film thickness. The red squares are data from Berger et.al. The dashed line is the expected electron density from the Drude's model, $n_e \approx n_a$, where n_a is the atomic density. One conduction electron per atom is assumed.

Chapter 7

Dynamics of propagating DWs

7.1 Introduction

As shown in the previous chapters, owing to the anisotropic magnetoresistance of permalloy, the resistance of the nanowire provides variety of information regarding the properties of DW. From dc-resistance measurements, not only the presence of the DW can be inferred by the resistance of the nanowire, but also the structure and even the chirality of a DW, if pinned at a pinning center, can be known by the resistance value. By measuring the nanowire resistance dynamically, or in real-time, the DW velocity can be estimated. In this chapter, it is shown that the dynamics of a propagating DW can be probed by combining both dc and real-time resistance measurements. Understanding the mechanisms of how DWs will propagate under the influence of field and current is essential in building devices based on DWs.

Theoretically, it has long been predicted that the propagation of DWs changes from a simple translation to more complex precessional modes, including changes in the DW structure as it propagates[133]. Experimentally, however, indirect evidence of this transition is only found from a sudden drop in the wall's velocity and direct observation of the precessional modes is lacking. In addition, with the advent of magnetic nanowires of dimensions comparable to the DW widths it is possible to imagine that DWs propagating along such wires will exhibit a well defined precessional mode due to confinement. By contrast, in extended structures, which have been

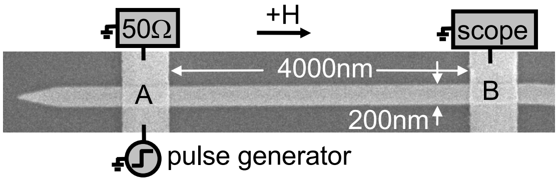

Figure 7.1: Scanning electron microscopy image of a permalloy nanowire (horizontal) and its electrical contacts (vertical lines). A schematic illustration of the real-time resistance measurement setup is overlaid on the image.

extensively studied in the past [134, 135, 136], many modes are accessible. It is shown in this chapter that DWs propagate along permalloy nanowires with a periodic variation in the chirality of the walls, a direct observation of the precessional mode. A combination of quasi-static and real time resistance measurement techniques are used to probe the precessional mode. The effect of the magnetic field and the current that passes through the nanowire on the precessional mode are studied.

7.1.1 Experimental setup

A scanning electron microscopy (SEM) image of a typical nanowire is shown in Fig. 7.1. The distance between the two contact lines, labeled A and B, is 4 μm and the width of the nanowire is 200 nm unless mentioned. The nanowire has two straight arms perpendicular to each other. These arms are connected via a quarter circle whose radius is 3 μm. Both end of these arms are tapered to a sharp point to prevent the formation of DWs outside the contact line [121] and to assist annihilation of any DW that enters this region. See Fig. 6.13 (a) for the full SEM image of the device. Only the horizontal arm is used here. Two types of nanowire are used in this chapter. For the time resolved resistance measurements (Section 7.2), nanowires without any artificial pinning sites are used. For the quasi-static measurements (Section 7.3), a nanowire with an artificial pinning site patterned $\sim 3\mu$m away from line A is used. The pinning site consists of a triangularly shaped notch on one side of the nanowire, whose depth is $\sim$30% of the wire width.

DC-40 GHz bandwidth probes are used to make contact to the devices. A pulse generator (PG-B, Picosecond Pulse Labs, model 10300B) is connected to contact line A. A 50 Ω termination is connected to the other end of line A. For the time resolved resistance measurements (Section 7.2), a 6GHz real-time oscilloscope (Agilent Technologies, model 54855A) is connected to contact line B, as shown in Fig. 7.1. For the quasi-static measurements (Section 7.3), a dc resistance measurement setup is connected to line B (see Fig. 7.6).

The local field generation method is used to inject a DW into section A-B of the nanowire. A magnetic field H is applied along the wire during the voltage pulse injection to assist the subsequent propagation of a DW. Note that this field H corresponds to H_{INJ} used in Chapter 5. A fraction of the injected voltage pulse flows into section A-B, thereby injecting current into the nanowire as the DW propagates along it. The current density that flows into the nanowire scales as $\sim 0.5 \times 10^8$ A/cm^2 per volt in these nanowires. Positive current is defined as current flowing from line A to B.

7.2 Time-resolved resistance oscillations

The DW injection and propagation experiment is repeated more than 16,000 times and the signal traces ΔV from each of these experiments are averaged to obtain an adequate signal to noise ratio. See Chapter 6 for details of the measurement method.

Figure 7.2 (a) and (b) show typical traces of the averaged signal ΔV obtained by the oscilloscope. A head to head (HH) wall is injected into section A-B using 100 ns long (a) -2.8 V and (b) 2.8 V high voltage pulses. As explained in the previous chapter, ΔV increase for the period of time τ for which the DW spends in section A-B. See Fig. 6.3 (b) for the definition of τ. Note that the size of increase in ΔV is proportional to the resistance difference between the magnetized state (R_{SAT}) and the state with a DW (R) in section A-B, or $\Delta R = R - R_{SAT}$. τ depends on the DW velocity which is influenced by both the field and the current. This is clearly seen by the DW velocity plotted in Fig. 7.3 as a function of the magnetic field. Negative and positive currents increase and decrease the DW velocity, respectively. The Walker breakdown field of this 200 nm wide nanowire is $\sim$14 Oe.

In Fig. 7.2 (a) and (b), oscillations of the signal amplitude are observed, for both

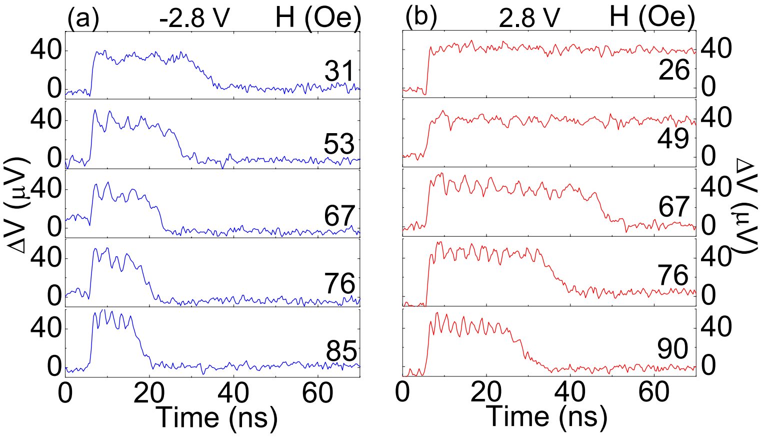

Figure 7.2: Real-time measurements of the DW propagation along the nanowire obtained by averaging the temporal evolution of the nanowire resistance 16,000 times. Signal traces ΔV shown are obtained using -2.8 V (a) and 2.8 V (b) voltage pulses to inject a HH DW are shown. Representative signal traces are shown at various fields indicated in each panel.

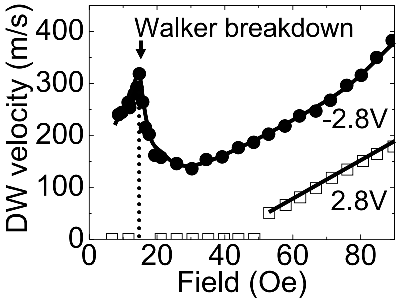

Figure 7.3: DW velocity versus magnetic field measured using -2.8 V (solid circles) and 2.8 V (open squares) voltage pulses to inject a HH DW. The Walker breakdown field is indicated in the figure. A 200 nm wide nanowire is used.

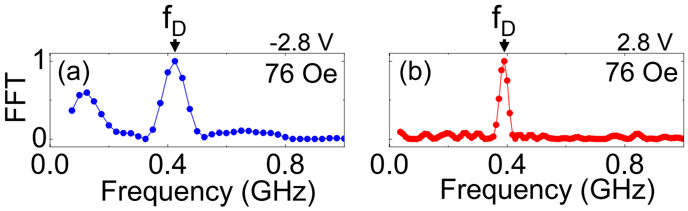

Figure 7.4: Exemplary FFT spectra of the signal trace ΔV shown when (a) -2.8 V and (b) 2.8 V voltage pulses are used to inject a HH DW. The applied field during the injection is 76 Oe. Note that the lower frequency feature seen in (a) simply corresponds to $\frac{1}{\tau}$. Definition of the oscillation frequency f_D is shown.

polarities of the voltage pulse, when the DW is propagating along section A-B. The signal amplitude does not oscillate when the DW moves out from section A-B, that is, after the ΔV levels drop to zero. Thus these oscillations must be related to the dynamics of the propagating DW. Since the signal amplitude is proportional to ΔR, or the size of the DW, these oscillations indicate that the size of the DW is periodically changing. This is particularly remarkable given that the signal represents an average of more than 16,000 successive independent DW injections and propagations along the nanowire. Thus this entire process must be highly repeatable and coherent.

Fast Fourier Transform (FFT) spectra of the signal traces are calculated to acquire the oscillation frequency. Exemplary FFT spectra of these traces are shown in Fig. 7.4 (a) and (b). The spectra is normalized to the peak value. In these spectra a well defined peak is observed. We define the frequency where the peak is observed as f_D. Note that the lower frequency feature seen in Fig. 7.4 (a) simply corresponds to the $\frac{1}{\tau}$.

The oscillation frequency f_D is plotted against the magnetic field in Fig. 7.5 for (a) head to head (HH) and (c) tail to tail (TT) walls. Voltage pulses of ±2.8 V are used to inject a DW into section A-B. For both wall types, the dependence of f_D on the magnetic field is approximately linear. Note that resistance oscillations are observed only when the field exceeds the Walker breakdown field (∼14 Oe). Although the current density ($\sim \pm(1.4 - 1.5) \times 10^8$ A/cm^2) that flows into the nanowire has a significant impact on the DW velocity (see Fig. 7.3), the dependence of f_D on the

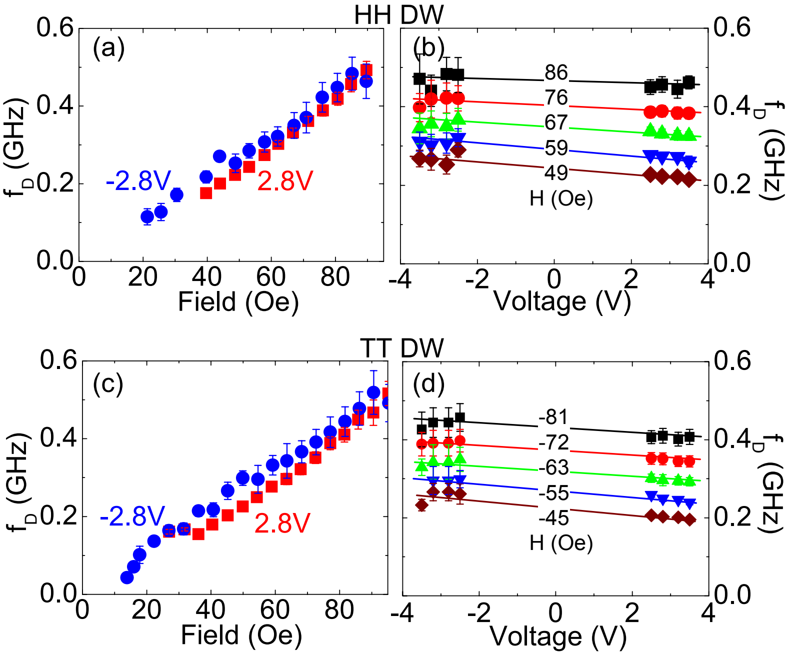

Figure 7.5: (a,c) Dependence of the frequency of the oscillations in resistance observed in the signal traces (ΔV) plotted versus field. Data shown are when ±2.8 V voltage pulses are used to inject a (a) HH and (c) TT DW. Oscillation frequency f_D is determined by taking the FFT spectra of each trace. Error bars correspond to the width of a Gaussian to which the peak structure in the FFT spectra is fitted. (b,d) Dependence of the oscillation frequency f_D on the amplitude of the voltage pulse in various magnetic fields. The definition of the error bars is the same as in (a,c). Solid lines are guides to the eye.

current density seems to be relatively small. In Fig. 7.5, the dependence of f_D on the amplitude of the voltage pulse, at selected fields, are shown for (b) HH and (d) TT walls. The dependence of f_D on the amplitude is small at each field for both wall types, however,f_D is systematically higher for negative as compared to positive currents of the same magnitude.

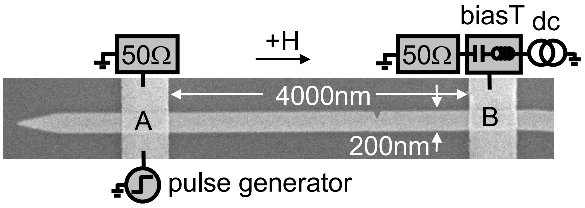

Figure 7.6: Scanning electron microscopy image of a permalloy nanowire (horizontal) and its electrical contacts (vertical lines). A schematic illustration of the quasi-static resistance measurement setup is overlaid on the image.

7.3 Chirality oscillations in propagating DWs

The resistance oscillations observed in the real-time measurements indicates that ΔR, or the size of the DW, is periodically changing as the DW propagates. As was shown in the previous chapters, the size of ΔR can be correlated with the DW structure. When a DW is pinned at an artificial pinning cite, not only the structure but also the chirality of the DW can be inferred by ΔR. However, it is rather difficult to infer the state of the DW in real-time measurements since some ambiguities remain in the conversion of the signal amplitude ΔV to ΔR using Eq. 6.5. Therefore we use quasi-static measurements in which ΔR of the DW state is measured, precisely, by dc-resistance measurements and use nanosecond long pulses to inject the DW into the nanowire as well as to pass currents.

The quasi-static resistance measurement setup, together with the SEM image of the nanowire and the contact lines, are shown in Fig. 7.6. The local field generation method is used to inject a DW into section A-B. A magnetic field H (equivalent to H_{INJ} in Chapter 5) is applied during the voltage pulse application to assist subsequent propagation of the DW. A triangularly shaped notch, whose depth is $\sim$30% of the width of the wire, is located 3μm away from line A to form a pinning center.

Figure 7.7 (a) shows a histogram of the ΔR value when a DW is injected into section A-B and trapped at the notch, using a 2.5V high 10 ns long voltage pulse. ΔR represent the difference in the nanowire resistance before and after the DW injection. Zero ΔR represents the state without any DW in section A-B. Three distinct non-zero

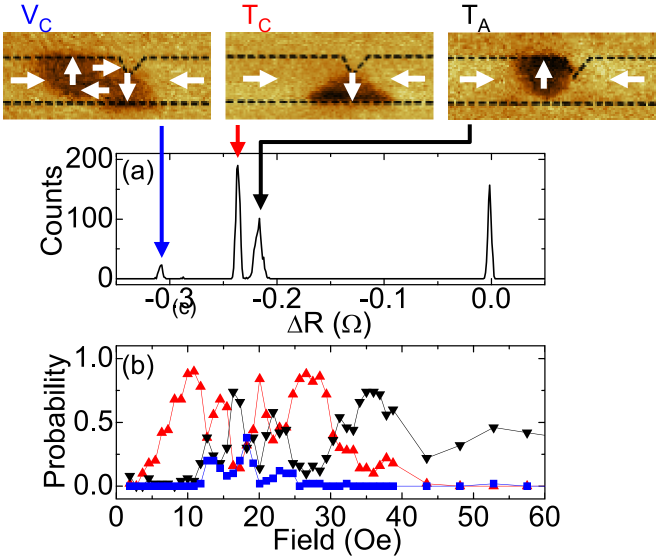

Figure 7.7: (a) Histograms of ΔR values measured in successive repeated experiments in which a HH DW is injected into the nanowire using a 2.5 V high, 10 ns long voltage pulse and is trapped at a notch located ~3 μm away from line A. The notch is triangularly shaped, as shown in the MFM images. ΔR is the difference in the resistance of the nanowire before and after the DW injection. The magnetic configurations corresponding to each ΔR peak are shown as MFM images. The white arrows in the MFM images denote the magnetization directions. (b) Probability of trapping a DW at the notch for V_C (blue), T_C (red) and T_A (black) walls as a function of the magnetic field. A 2.5 V, 10 ns long voltage pulse is used to inject a HH DW.

ΔR values are observed in the histogram, whose corresponding magnetic structures, imaged using magnetic force microscopy (MFM), are shown on the top of Fig. 7.7 (a). Two transverse walls with clockwise T$_C$ and anticlockwise T$_A$ chiralities and one clockwise vortex wall V$_C$ are observed. A small peak around ΔR ~-0.29 Ω presumably corresponds to the anticlockwise vortex wall V$_A$. The probability of injecting and trapping each type of DW at the notch is plotted as a function of H in Fig. 7.7 (b). The probability of injecting different types of DWs has a complex dependence on the magnetic field. Vortex walls can be injected and trapped in a relatively small field range with much lower probability than either of the two transverse walls. Note that the dimensions of the nanowire used here favor transverse walls.

The probabilities of trapping T$_A$, T$_C$ and V$_C$ DWs at the notch are plotted as a function of the pulse length at selected fields in Fig. 7.8 (a-d). HH (a, b) or TT (c, d) DWs are injected using -2.5 V (a, c) and 2.5 V (b, d) voltage pulses. For the case of positive voltages, oscillations in the trapping probability are observed for pulse lengths up to ~100 ns, the limit of our experimental setup. By contrast, for negative voltages, oscillations in the probability are seen only for much shorter pulse lengths, typically below ~30 ns. In both cases oscillations are clearly observed only for fields above ~14 Oe, which is close to the Walker breakdown field for these nanowires. Below this field the trapping probability is nearly independent of the pulse length.

In order to estimate the oscillation periods observed in the trapping probability, the curves are fitted to the following form.

$$P = A\exp(-\frac{t_P}{\tau_d})\sin(2\pi f_{QS} t_P + phase) \tag{7.1}$$

where A, τ_d, f_{QS} are the amplitude, decay time and frequency of the exponential sinusoid, respectively, and t_P is the pulse length. In Fig. 7.9, the oscillation frequency f_{QS} and the phase are plotted against the magnetic field for both wall types, (a, c) HH and (b, d) TT wall. In all plots, f_{QS} and the phase are compared for each DW structures. Whereas f_{QS} is approximately proportional to the field regardless of the DW state, the phases of the oscillations depend on the DW state. T$_A$ and T$_C$ walls are 180^o out of phase with each other and the V_C wall is 90^o out of phase from the

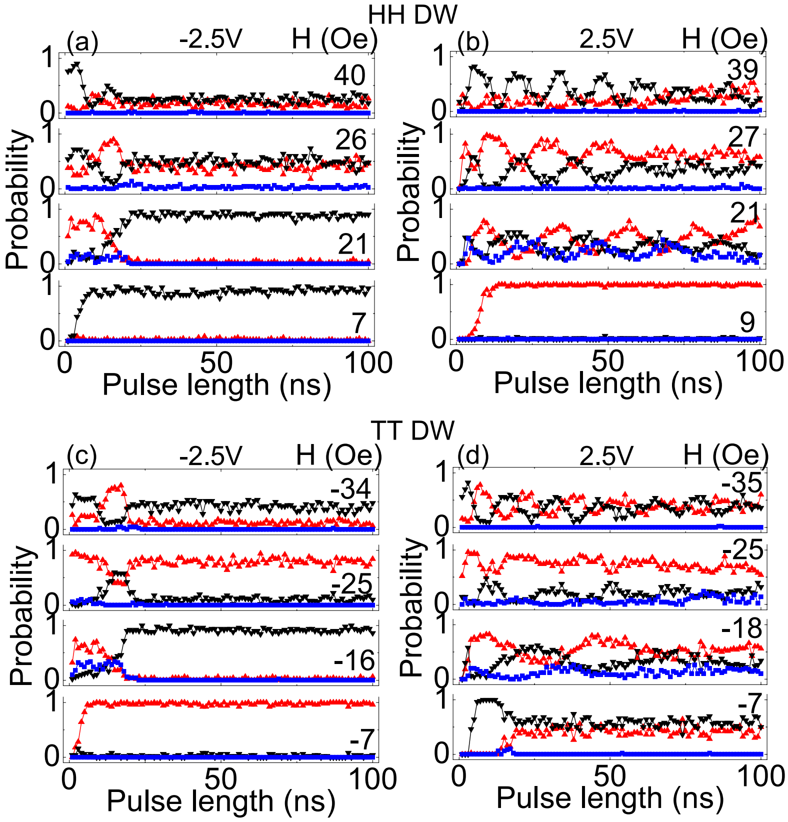

Figure 7.8: Probability of trapping a DW, V_C (blue), T_C (red) and T_A (black), at a notch plotted against the voltage pulse length at different fields. (a) and (b) represent the trapping probability when -2.5 V and 2.5 V voltage pulses are used to inject a HH DW, respectively. The same plots are shown for the TT DW in (c) and (d).

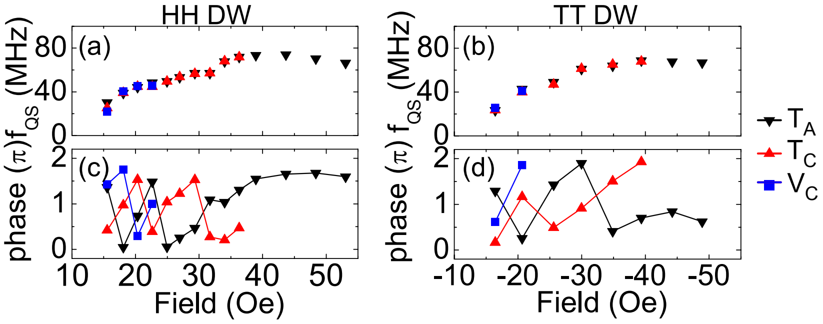

Figure 7.9: Frequency f_{QS} (a,c) and phase (b,d) of the oscillations of the trapping probability obtained by fitting them to Eq. (7.1). f_{QS} and the phase are plotted against the magnetic field for each wall structure. Phases are in units of π. Data shown are when 2.5 V voltage pulse is used to inject a (a,c) HH and (b,d) TT DW.

transverse walls. At higher fields, above $\sim \pm 40$ Oe, only T_A walls are trapped at the notch: in this field range we find that f_{QS} saturates and the phase of the oscillation varies little. The trend is the same regardless of the DW type.

The dependence of the f_{QS} and the phase on the voltage pulse amplitude is also investigated. Fig. 7.10 shows the pulse length dependence of the trapping probabilities for the transverse DWs at selected pulse amplitudes for both (a) HH and (b) TT walls. The pulse amplitude is varied from 2.5 V to 3.5V and the magnetic field is fixed at 25 Oe. The oscillation frequencies and phases, extracted by fitting Eq. (7.1) to the T_A wall trapping probabilities, are shown in Fig. 7.11 for (a) HH and (b) TT walls. At a fixed field the oscillation frequency is nearly independent of the amplitude, whereas the phase depends on the pulse amplitude. Detailed analysis of these data are discussed in the next section.

7.4 Micromagnetic simulations and the 1D model

7.4.1 Micromagnetic simulations

We first use micromagnetic simulations to identify the origin of the resistance oscillations seen in the time resolved measurements. Micromagnetic simulations were

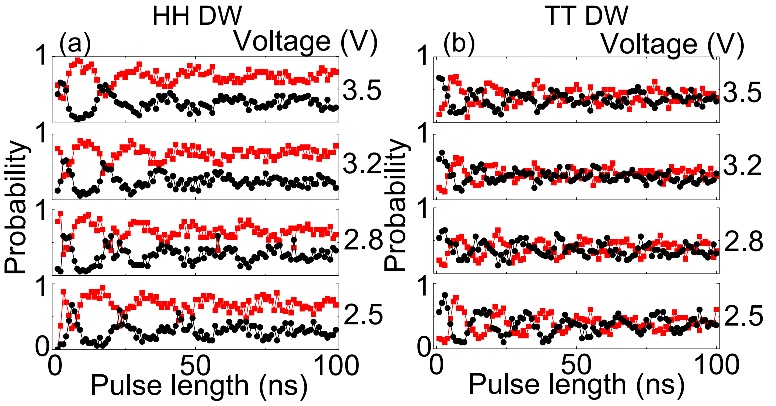

Figure 7.10: Probability of trapping a transverse wall, T_C (red) and T_A (black), at a notch plotted against the voltage pulse length for different pulse amplitudes. Data are shown for (a) HH and (b) TT walls. The applied magnetic field is 25 Oe.

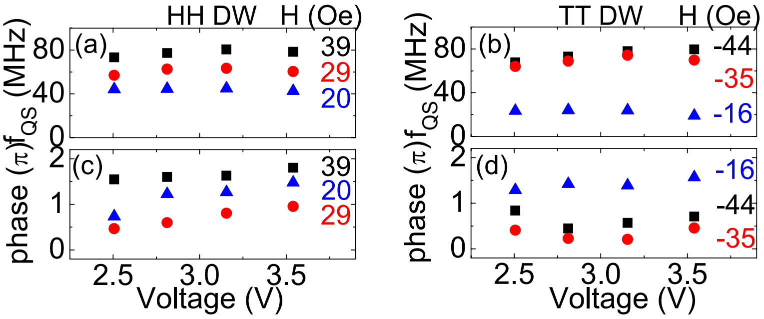

Figure 7.11: Dependence of the frequency f_{QS} (a,b) and the phase shift (c,d) of the oscillations of the trapping probability on the pulse amplitude. f_{QS} and phase shift are obtained from fitting the trapping probability to Eq. (7.1). Numbers on the side indicate the corresponding magnetic field used during the injection of a DW. Data are shown for (a,c) HH and (b,d) TT walls. Solid lines are guides to the eye.

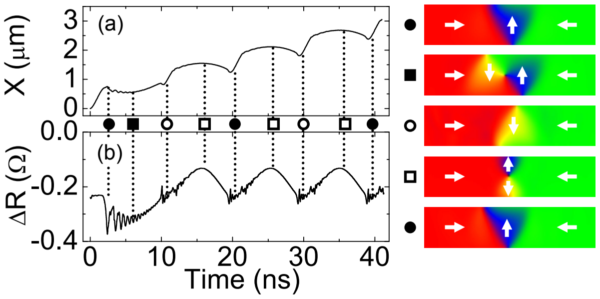

Figure 7.12: Temporal evolution of (a) the position of the DW and (b) the estimated ΔR of the nanowire calculated from micromagnetic simulations in an applied field of 20 Oe and zero current. Symbols and corresponding magnetic configurations show the structure of the DW at the extrema of each cycle of its motion.

carried out on permalloy nanowires with the same physical dimensions as those used in the experiments (200nm wide, 10nm thick), for fields above the Walker breakdown field. Moving boundary conditions are employed to avoid edge effects. The Gilbert damping parameter α is set to 0.01 to match the experimental value of the Walker breakdown field. A transverse wall with anticlockwise chirality (top panel of the images shown at the right hand side of Fig. 7.12 is chosen as the initial state to compute the temporal evolution of the position and the structure of the DW driven by magnetic field.

Fig. 7.12 (a) shows the temporal evolution of the DW position when a magnetic field of 20 Oe is applied (no current). The position of the DW oscillates as it propagates along the wire. These oscillations are associated with periodic changes in the DW structure, as indicated by the symbols[133]. The DW state oscillates periodically from a transverse wall of one chirality to a transverse wall of the opposite polarity via a vortex wall or an anti-vortex wall state.

The resistance fluctuation due to the change in the DW structure can be estimated from these simulations. Instead of calculating the resistance of the nanowire using finite element method calculations, we can estimate the resistance fluctuation, due to the change in the magnetization configuration, from the temporal evolution in the total anisotropic energy E_{ANI}. Both AMR and E_{ANI} take the same form with regards to the direction cosines of the magnetic moments and the nanowire's long axis, i.e. $AMR \propto \cos^2\theta$ and $E_{ANI} \propto \cos^2\theta$. This is because the nanowire's long axis coincides with the direction of the current flow as well as the direction of the magnetization easy axis. The resistance of the nanowire is thus expressed as

$$R = R_{SAT}(1 - \frac{\Delta\rho}{\rho}\frac{E_{ANI}}{K_u V}) \tag{7.2}$$

where $\frac{\Delta\rho}{\rho}$ is the AMR ratio, K_u is the anisotropy constant and V is the volume of the system. The resistance difference between the state with a DW in the nanowire and the magnetized state is then $\Delta R = R - R_{SAT}$ and is plotted in Fig. 7.12 (b). We take $K_u = 1000 erg/cm^3$, $V = 2000 \times 200 \times 10$ nm^{-3}, $\rho = 30\mu\Omega cm$ and $\frac{\Delta\rho}{\rho} = 1.5\%$ for permalloy. The magnitude of the estimated ΔR agrees well with the experimental values; compare these values with the ones shown in Fig. 7.7 (a). The amplitude of the signal trace ΔV can be calculated by substituting the resistance (Eq. (7.2) into Eq. (6.1) and subtracting the background.

The calculated ΔV converted from the simulated ΔR shown in Fig. 7.12 (b) are shown in Fig. 7.13 (a). ΔV calculated at different fields are shown in Fig. 7.13 (b) and (c). These curves can be compared to the experimental results shown in Fig. 7.2. Note that the absolute magnitude of the calculated ΔV do not match with the experimental data since the resistance of the contact lines are not incorporated into the calculations. In addition the amplitudes of the ΔV oscillations appear larger in the calculations. In the experiment, any incoherence in the resistance oscillation results in smearing the ΔV oscillation, i.e. destructive interference occurs. In other words, the amplitude of the ΔV oscillation observed in the experiments provides degree of the coherence.

Interesting features are observed in the calculated ΔV oscillations in Fig. 7.13. The frequency of transverse walls ($\Delta V \sim 90\mu$V) appearing increases as the magnitude of the field is increased. However, depending on the DW structures that appear between the transverse walls, the overall oscillation frequency of the ΔV changes. The DW structures involved in Fig. 7.13 (c) are only the transverse walls and the anti-vortex walls; vortex walls do not appear in this process. Thus the ΔV oscillation

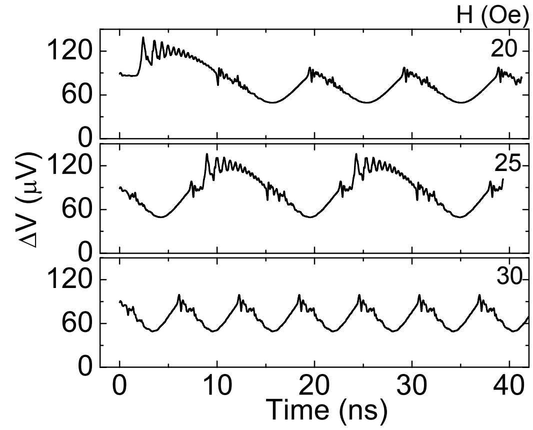

Figure 7.13: Calculated time dependence of ΔV, estimated from ΔR of the nanowire, using micromagnetic simulations. The applied field are shown at the right.

frequency coincides with the frequency the transverse walls appear. By contrast, in Fig. 7.13 (b), vortex and anti-vortex walls appear alternatively between the transverse walls. In this case, ΔV oscillation frequency is halved (oscillation period is doubled) compared to the frequency the transverse walls appear.

The period doubling are also observed in experiments. Figure 7.14 (a) show the signal traces ΔV obtained in a 300 nm wide permalloy nanowire. Here, a voltage pulse of 2.0 V high and 100 ns long is used to inject a TT wall. The applied magnetic fields are shown on the right side of each panel. This is the field range where the pressure from the field is compensated by current via spin transfer torque when a positive voltage pulse is used. Thus the DW velocity is significantly reduced. The corresponding FFT spectra of each trace shown in Fig. 7.14 (a) are shown in (b). In addition to the main peak, a secondary peak is observed in all cases. The frequencies (f_D) at which these peaks are observed are plotted in Fig. 7.15. Comparing the values of f_D between the 300 nm and 200 nm wide (see Fig. 7.5) nanowires, interestingly, it is the secondary peaks in the 300 nm nanowire that match f_D measured in the 200 nm wide nanowire. Note that the period doubling is also observed in the 200 nm wide wires in some field range, however the effect is more pronounced in the 300 nm wide ones. This is largely due to the size of the nanowire; the period doubling occurs

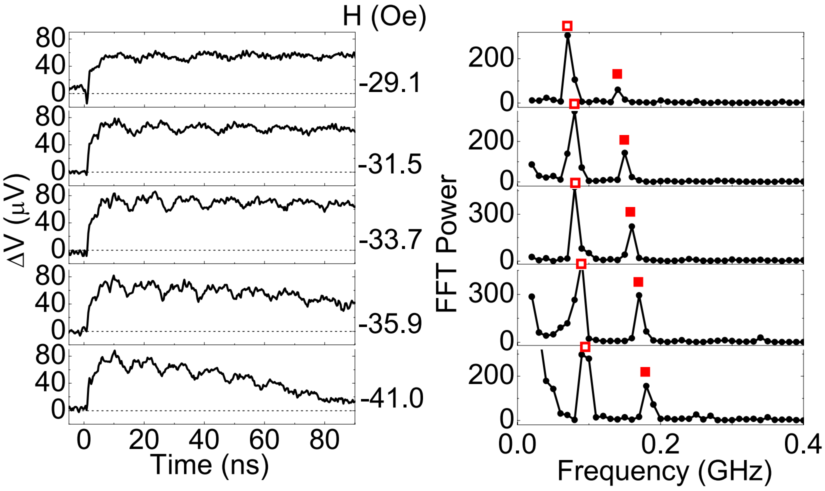

Figure 7.14: (a) Real-time measurements of the DW propagation along the nanowire obtained by averaging the temporal evolution of the nanowire resistance 16,000 times. Signal traces ΔV shown are obtained when a 2.1 V voltage pulse is used to inject a TT DW are shown. Representative signal traces are shown at various fields indicated in each panel. (b) FFT spectra calculated from the signal traces shown in (a). The square symbols illustrate the position of the first and second harmonics in the oscillation frequency. The nanowire width is 300 nm here.

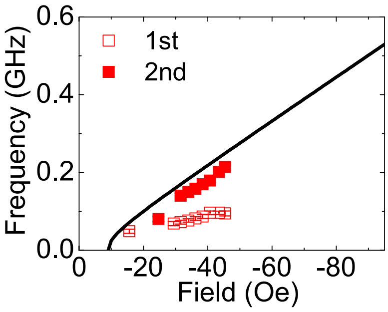

Figure 7.15: Dependence of the oscillation frequency f_D on magnetic field when 2.1V voltage pulses are used to inject a TT DW in a 300 nm wide nanowire. The first and second harmonics of the oscillation frequency are plotted. Error bars correspond to the width of a Gaussian to which the peak structure in the FFT spectra is fitted. The solid line represents values of f_D calculated using from Eq.(7.3), assuming zero current (u=0) and a value of α=0.01.

through the appearance of the vortex wall which is energetically more favored in the 300 nm wide nanowires.

7.4.2 1D model

It is interesting to compare f_D with the oscillation frequency calculated using the one dimensional (1D) model of DW motion. This frequency can be derived by computing the period of the oscillations in the position of the DW when driven by magnetic field above the Walker breakdown field. This was derived in Chapter 6 and is given by Eq. 6.19. The oscillation frequency thus reads

$$f_D = \frac{\gamma}{\pi(1+\alpha^2)}\sqrt{(H + (\beta - \alpha)\frac{u}{\gamma\Delta})^2 - H_{WB}^2} \tag{7.3}$$

where is γ is the gyromagnetic ratio, α is the Gilbert damping constant, β is the non-adiabatic spin torque term, Δ is the DW width and H_{WB} is the Walker breakdown field (see Eq. 6.17). The parameter $u = \frac{\mu_B JP}{eM}$ is the spin transfer torque term and μ_B is the Bohr magnetron, J is the current density, P is the spin polarization of the current, e is the electric charge and M is the saturation magnetization. The calculated f_D is approximately linear in field and the slope is given simply by $\sim \frac{\gamma}{\pi}$, which is two times the Larmor frequency. Since the current have little effect on f_D (see Fig. 7.5 (b, d)), we use Eq. (7.3) with $u = 0$, the case where no current is flowing in the nanowire. The calculated f_D for both 300 nm and 200 nm wide nanowires are shown in Fig. 7.15 and Fig. 7.16, respectively. The calculated f_D agrees well with the experimentally observed values.

The quasi-static results can be understood within the same framework. The structure of the DW will evolve periodically during the time that the DW travels from its point of injection to the pinning center (∼3 μm). This time is determined by the average DW velocity which depends on the field and the duration and magnitude of the current pulse. Thus, for a given field and current pulse amplitude the DW will arrive at the notch sooner when the spin polarized current drives the DW towards the notch and later when the current is in the opposite direction. For a given current

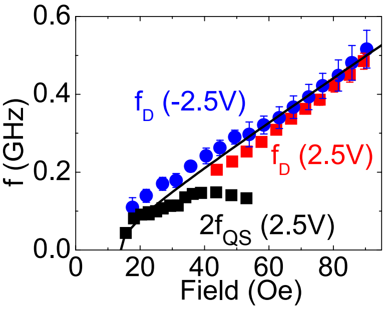

Figure 7.16: Dependence of the oscillation frequency f_D on magnetic field when ±2.5 V voltage pulses are used to inject a HH DW. Error bars correspond to the width of a Gaussian to which the peak structure in the FFT spectra is fitted. These data are compared with the oscillation frequency f_{QS} obtained from the quasi-static experiments shown in Fig. 7.9 (a). The solid line represents values of f_D calculated using from Eq.(7.3), assuming zero current (u=0) and a value of α=0.01.

direction the arrival time of the DW is then determined by the length of the current pulse unless the pulse is so long that the DW reaches the notch before the end of the pulse. On the other hand the frequency of the periodic structural changes is largely independent of the current (see Fig. 7.5 (b, d)). Therefore, the DW will have a distinct structure when it arrives at the pinning center, oscillating with the pulse length.

To illustrate this process, the temporal evolution of the position of the DW is calculated using the 1D model and are shown in Fig. 7.17 (a). Magnetic field of 20 Oe is applied and a current pulse, whose direction is such that the spin transfer torque opposes the field driven motion, is applied ($u = 140m/s$). Other parameters are listed in the caption. The length of the current pulse is 0 ns (black line), 11.8 ns (red), 23.6 ns (green) and 35.4 ns (blue). The times at which the current pulse is turned off are indicated by the arrows with the same color. The structure of the DW is represented by the circles; open and solid circles correspond to the two transverse walls with opposite chirality. MFM images are shown at the right to provide images of these hypothetical DW structures represented by the symbols. To simplify, assume that only two structures exist during the propagation and the DW structure changes from one to the other abruptly at each valley of the DW position.

In the experimental setup, the DW has to travel ~3 μm to reach the notch; this point is represented by the horizontal dotted line. When no current pulse is applied (black line), the DW reaches the notch at ~18 ns, where the structure of the DW is the open circle state. While the current pulse is turned on, the mean distance the DW travels is close to zero. After the current pulse is turned off, it starts to move toward the notch. Take for example the case where the current pulse is cut off at 11.8 ns (red line). The DW reaches the notch at ~26 ns, at which the DW structure is the closed circle state. The structure of the DW when it reaches the notch can thus be determined as a function of the current pulse length and is plotted in Fig. 7.17 (b) for the two transverse walls. Note that the probability here is either one or zero. The probability oscillates with the pulse length, as was observed experimentally in Fig. 7.8.

In Fig. 7.8, for positive voltages, when the current opposes the field driven motion of the DW, the DW moves so slowly that it never reaches the pinning site before the end of the 100 ns long voltage pulse used. Thus, we observe oscillations in DW structure for pulses up to 100 ns long as shown in Fig. 7.8 (b, d). This interpretation assumes that the DW structure does not evolve further once the DW is pinned at the notch. This assumption is consistent with the results for negative currents, in which the DW moves faster as the current pushes it towards the notch. In this case, when the current pulse exceeds the time for the DW to reach the notch (~15-20 ns in Fig. 7.8(a, c)), the trapping probability becomes constant, which would not be the case were the DW structure to continue to evolve once pinned. Note that slightly higher current densities can result in DW transformations, as seen in Chapter 5.

The periodic variation in DW structure thus accounts for both the oscillatory dependence of the DW trapping probability on current pulse length and the oscillations in DW resistance during motion. Moreover, the difference by a factor of two in frequencies of these oscillations can be readily understood since in the quasi-static measurements the T_A and T_C walls have different resistance values whereas in the time resolved measurements they have the same resistance. This is because the notch used in the quasi-static experiments is asymmetric so that the T_A and T_C walls are

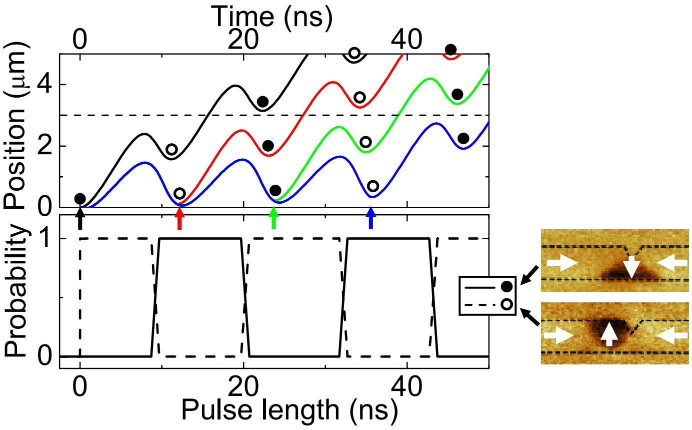

Figure 7.17: (a) Calculated temporal evolution of the position of the DW are shown when different lengthes of current pulses are applied. The amplitude of the current pulse is u=-140 m/s. The colored arrows indicate the time when the current pulse is turned off. (For the black solid line, no current is applied.) The open and solid circles represent the hypothetical state of the DW, i.e. transverse walls with opposite chirality. (b) The calculated probabilities of the virtual transverse walls plotted against the current pulse length. MFM images are shown at the right to provide images of the virtual DW structures represented by the symbols.

distinguishable. These oscillation frequencies are compared in Fig. 7.16 where f_D and $2f_{QS}$ are plotted. At low fields the frequencies are in reasonable agreement but presumably at higher fields the notch potential plays a significant role so accounting for the difference.

In summary, the precessional rotation of a magnetic domain wall associated with its translational motion was directly observed using quasi-static and time-resolved resistance measurements in permalloy nanowires. The domain wall dynamics are surprisingly coherent. The precession frequency monotonically increases with magnetic field as determined by the Larmor precession frequency. The precessional rotation of the domain wall can be used to set the DW's structure at a given position along the nanowire by a combination of magnetic field and spin polarized current.

Chapter 8

Conclusion

The current and field induced dynamics of magnetic domain walls (DWs) was investigated in permalloy ($Ni_{81}Fe_{19}$) nanowires by injecting single domain walls and monitoring their presence and motion in the nanowires from their resistance using both dc and high speed measurements.

It was shown that resistance measurements could be used to detect the presence of DWs of various structures and chiralities by combining resistance measurements with magnetic force microscopy imaging. Vortex and transverse DWs could readily be distinguished from the different resistance values that the nanowire exhibit due to their different size and associated transverse magnetization components. When an artificial pinning site is introduced in the nanowire, the chirality of both vortex and transverse DWs pinned at such a pinning center can be deduced from the nanowire's resistance due to the inhomogeneous current flow around the pinning center.

Current induced dynamics of magnetic domain walls (DWs) in permalloy ($Ni_{81}Fe_{19}$) nanowires were investigated. Resistance measurements are used to detect the presence of the DW in the nanowire. Combined with magnetic force microscopy imaging, the resistance of the nanowire can be correlated with the structure of the DW. Vortex and transverse DWs are observed in nanowires that were investigated. Furthermore, when DWs are pinned at a pinning center, the chirality of the DW can even be deduced from the nanowire's resistance level.

Time resolved resistance measurements of the nanowire enabled estimates of the

DW velocity, driven by magnetic field and/or current. The dependence of the DW velocity on magnetic field revealed the complex dynamics of such motion. As the magnetic field was increased from zero, the DW velocity was observed to increase to a maximum value at the so-called Walker breakdown field. Above this field the DW velocity decreases to a minimum value before increasing again at higher fields. Time resolved resistance measurements performed when the magnetic field is larger than the Walker breakdown field showed that DW structure is periodically changing as it propagates through the nanowire. Surprisingly, the change in the DW structure turns out to be highly coherent and reproducible.

When a current density of the order $\sim 10^8$ A/cm^2 is applied to the nanowire, the field-driven DW velocity can be increased or decreased by more than 100 m/s depending on the current direction. These large changes in DW velocity are attributed to the spin transfer torque effect arising from the interaction between the DW and the spin-polarized current. In the absence of any magnetic field, DWs can be moved with current at the velocity of ~100 m/s, significantly higher than the reported values in the literature but close to that predicted theoretically.

The current density needed to move the DW from a pinning center (notch) was investigated by measuring the nanowire's resistance before and after the application of a current pulse. The current density needed to depin a DW from a notch shows a non-linear dependence on the applied magnetic field. In all field ranges, transformations between different DW structures was observed, which strongly affects the depinning process. When the applied field is near zero, the critical current to depin the DW becomes nearly independent of the DW structure, which likely indicates that the DWs are transformed under current to the same DW state when they actually depin. However, significant Joule heating simultaneously occurs at the current densities needed to depin the DWs so that this needs to be considered.

When the current pulse length is tuned to certain values (at the nanosecond time scale), a lowering of the critical current is observed compared to the case when long current pulses are used. In addition, the probability of depinning the DW oscillates with the current pulse length, where the oscillation periods depend on the DW structure, applied magnetic field and the current density. These effects arise from current induced oscillations of the DW when trapped at a pinning center. The oscillation amplitude is amplified after the end of the current pulse, if the timing of the pulse matches the DW precessional period. Taking advantage of this dynamic amplification could open ways to reduce the critical current density to move DWs in magnetic nanodevices.

Bibliography

[1] Hubert, A. & Schafer, R. *Magnetic Domains: The Analysis of Magnetic Microstructures* (Springer, 2001).

[2] Bar'yakhtar, V. G., Chetkin, M. V., Ivanov, B. A. & Gadetskii, S. N. *Dynamics of topological magnetic solitons* (Springer-Verlag, 1994).

[3] Malozemoff, A. P. & Slonczewski, J. C. *Magnetic Domain Walls in Bubble Material* (Academic Press, New York, 1979).

[4] Slonczewski, J. C. Theory of domain-wall motion in magnetic-films and platelets. *J. Appl. Phys.* **44**, 1759–1770 (1973).

[5] Parkin, S. S. P. *et al.* Exchange-biased magnetic tunnel junctions and application to nonvolatile magnetic random access memory (invited). *J. Appl. Phys.* **85**, 5828–5833 (1999). Part 2B.

[6] Schumacher, H. W. *et al.* Phase coherent precessional magnetization reversal in microscopic spin valve elements. *Phys. Rev. Lett.* **90**, 017201 (2003).

[7] Schumacher, H. W., Chappert, C., Sousa, R. C., Freitas, P. P. & Miltat, J. Quasiballistic magnetization reversal. *Phys. Rev. Lett.* **90**, 017204 (2003).

[8] Back, C. H. *et al.* Minimum field strength in precessional magnetization reversal. *Science* **285**, 864–867 (1999).

[9] Tudosa, I. *et al.* The ultimate speed of magnetic switching in granular recording media. *Nature* **428**, 831–833 (2004).

[10] Worledge, D. C. Spin flop switching for magnetic random access memory. *Appl. Phys. Lett.* **84**, 4559–4561 (2004).

[11] Slaughter, J. *et al.* High speed toggle mram with mgo-based tunnel junctions. *IEDM Tech. Digest, 5-7 Dec.* 873–876 (2005).

[12] Worledge, D. C. Single-domain model for toggle mram. *IBM J. Res. & Dev.* **50**, 69–79 (2006).

[13] Kimel, A. V. *et al.* Ultrafast non-thermal control of magnetization by instantaneous photomagnetic pulses. *Nature* **435**, 655–657 (2005).

[14] Hansteen, F., Kimel, A., Kirilyuk, A. & Rasing, T. Femtosecond photomagnetic switching of spins in ferrimagnetic garnet films. *Phys. Rev. Lett.* **95**, 047402 (2005).

[15] Beaurepaire, E., Merle, J. C., Daunois, A. & Bigot, J. Y. Ultrafast spin dynamics in ferromagnetic nickel. *Phys. Rev. Lett.* **76**, 4250–4253 (1996).

[16] Hohlfeld, J., Matthias, E., Knorren, R. & Bennemann, K. H. Nonequilibrium magnetization dynamics of nickel. *Phys. Rev. Lett.* **78**, 4861–4864 (1997).

[17] Koopmans, B., van Kampen, M., Kohlhepp, J. T. & de Jonge, W. J. M. Ultrafast magneto-optics in nickel: Magnetism or optics? *Phys. Rev. Lett.* **85**, 844–847 (2000).

[18] Ohno, H. *et al.* Electric-field control of ferromagnetism. *Nature* **408**, 944–946 (2000).

[19] Chiba, D., Yamanouchi, M., Matsukura, F. & Ohno, H. Electrical manipulation of magnetization reversal in a ferromagnetic semiconductor. *Science* **301**, 943–945 (2003).

[20] Pugh, E. M. Band model for hall effect, magnetization, and resistivity of magnetic metals. *Phys. Rev.* **97**, 647–654 (1955).

[21] Berger, L. Exchange interaction between ferromagnetic domain-wall and electric-current in very thin metallic-films. *J. Appl. Phys.* **55**, 1954–1956 (1984).

[22] Berger, L. Motion of a magnetic domain-wall traversed by fast-rising current pulses. *J. Appl. Phys.* **71**, 2721–2726 (1992).

[23] Freitas, P. P. & Berger, L. Observation of s-d exchange force between domain-walls and electric-current in very thin permalloy-films. *J. Appl. Phys.* **57**, 1266–1269 (1985).

[24] Hung, C. Y. & Berger, L. Exchange forces between domain-wall and electric-current in permalloy-films of variable thickness. *J. Appl. Phys.* **63**, 4276–4278 (1988). Part 3.

[25] Hung, C. Y., Berger, L. & Shih, C. Y. Observation of a current-induced force on bloch lines in ni-fe thin-films. *J. Appl. Phys.* **67**, 5941–5943 (1990). Part 2B.

[26] Salhi, E. & Berger, L. Current-induced displacements and precession of a bloch wall in ni-fe thin-films. *J. Appl. Phys.* **73**, 6405–6407 (1993). Part 2B.

[27] Salhi, E. & Berger, L. Current-induced displacements of bloch walls in ni-fe films of thickness 120-740 nm. *J. Appl. Phys.* **76**, 4787–4792 (1994).

[28] Berger, L. Prediction of a domain-drag effect in uniaxial, non-compensated, ferromagnetic metals. *J. Phys. Chem. Solids* **35**, 947–956 (1974).

[29] Berger, L. Domain drag effect in the presence of variable magnetic-field or variable transport current. *J. Appl. Phys.* **50**, 2137–2139 (1979).

[30] Deluca, J. C., Gambino, R. J. & Malozemoff, A. P. Observation of a domain drag effect in amorphous gdcomo films. *IEEE Trans. Magn.* **14**, 500–502 (1978).

[31] Deluca, J. C., Gambino, R. J., Malozemoff, A. P. & Berger, L. Bias field-dependence of domain drag propagation velocities in gdcoau bubble-films. *J. Appl. Phys.* **52**, 6168–6172 (1981).

[32] Slonczewski, J. C. Current-driven excitation of magnetic multilayers. *J. Magn. Magn. Mater.* **159**, L1–L7 (1996).

[33] Tsoi, M. *et al.* Excitation of a magnetic multilayer by an electric current. *Phys. Rev. Lett.* **80**, 4281–4284 (1998).

[34] Myers, E. B., Ralph, D. C., Katine, J. A., Louie, R. N. & Buhrman, R. A. Current-induced switching of domains in magnetic multilayer devices. *Science* **285**, 867–870 (1999).

[35] Katine, J. A., Albert, F. J., Buhrman, R. A., Myers, E. B. & Ralph, D. C. Current-driven magnetization reversal and spin-wave excitations in co/cu/co pillars. *Phys. Rev. Lett.* **84**, 3149–3152 (2000).

[36] Yamaguchi, A. *et al.* Real-space observation of current-driven domain wall motion in submicron magnetic wires. *Phys. Rev. Lett.* **92**, 077205 (2004).

[37] Vernier, N., Allwood, D. A., Atkinson, D., Cooke, M. D. & Cowburn, R. P. Domain wall propagation in magnetic nanowires by spin-polarized current injection. *Europhys. Lett.* **65**, 526–532 (2004).

[38] Klaui, M. *et al.* Direct observation of domain-wall configurations transformed by spin currents. *Phys. Rev. Lett.* **95**, 026601 (2005).

[39] Klaui, M. *et al.* Controlled and reproducible domain wall displacement by current pulses injected into ferromagnetic ring structures. *Phys. Rev. Lett.* **94**, 106601 (2005).

[40] Florez, S. H., Krafft, C. & Gomez, R. D. Spin-current-induced magnetization reversal in magnetic nanowires with constrictions. *J. Appl. Phys.* **97**, 10C705 (2005).

[41] Grollier, J. *et al.* Switching a spin valve back and forth by current-induced domain wall motion. *Appl. Phys. Lett.* **83**, 509–511 (2003).

[42] Lim, C. K. *et al.* Domain wall displacement induced by subnanosecond pulsed current. *Appl. Phys. Lett.* **84**, 2820–2822 (2004).

[43] Yamanouchi, M., Chiba, D., Matsukura, F. & Ohno, H. Current-induced domain-wall switching in a ferromagnetic semiconductor structure. *Nature* **428**, 539–542 (2004).

[44] Wegrowe, J. E., Kelly, D., Jaccard, Y., Guittienne, P. & Ansermet, J. P. Current-induced magnetization reversal in magnetic nanowires. *Europhys. Lett.* **45**, 626–632 (1999).

[45] Wegrowe, J. E., Kelly, D., Truong, T., Guittienne, P. & Ansermet, J. P. Magnetization reversal triggered by spin-polarized current in magnetic nanowires. *Europhys. Lett.* **56**, 748–754 (2001).

[46] Tsoi, M., Fontana, R. E. & Parkin, S. S. P. Magnetic domain wall motion triggered by an electric current. *Appl. Phys. Lett.* **83**, 2617–2619 (2003).

[47] Ravelosona, D., Lacour, D., Katine, J. A., Terris, B. D. & Chappert, C. Nanometer scale observation of high efficiency thermally assisted current-driven domain wall depinning. *Phys. Rev. Lett.* **95**, 117203 (2005).

[48] Ravelosona, D. *et al.* Domain wall creation in nanostructures driven by a spin-polarized current. *Phys. Rev. Lett.* **96**, 186604 (2006).

[49] Nguyen, H. Y. T. *et al.* Exchange biased spin polarizer with an embedded nano-oxide layer for a substantially lower switching current density. *Appl. Phys. Lett.* **89**, 094103 (2006).

[50] Tatara, G. & Kohno, H. Theory of current-driven domain wall motion: Spin transfer versus momentum transfer. *Phys. Rev. Lett.* **92**, 086601 (2004).

[51] Thiaville, A., Nakatani, Y., Miltat, J. & Vernier, N. Domain wall motion by spin-polarized current: a micromagnetic study. *J. Appl. Phys.* **95**, 7049–7051 (2004). Part 2.

[52] Zhang, S. & Li, Z. Roles of nonequilibrium conduction electrons on the magnetization dynamics of ferromagnets. *Phys. Rev. Lett.* **93**, 127204 (2004).

[53] Li, Z. & Zhang, S. Domain-wall dynamics and spin-wave excitations with spin-transfer torques. *Phys. Rev. Lett.* **92**, 207203 (2004).

[54] Li, Z. & Zhang, S. Domain-wall dynamics driven by adiabatic spin-transfer torques. *Phys. Rev. B* **70**, 024417 (2004).

[55] Barnes, S. E. & Maekawa, S. Current-spin coupling for ferromagnetic domain walls in fine wires. *Phys. Rev. Lett.* **95**, 107204 (2005).

[56] Thiaville, A., Nakatani, Y., Miltat, J. & Suzuki, Y. Micromagnetic understanding of current-driven domain wall motion in patterned nanowires. *Europhys. Lett.* **69**, 990–996 (2005).

[57] Liu, X., Liu, X. J. & Ge, M. L. Dynamics of domain wall in a biaxial ferromagnet interacting with a spin-polarized current. *Phys. Rev. B* **71**, 224419 (2005).

[58] Dugaev, V. K. *et al.* Current-induced motion of a domain wall in a magnetic nanowire. *Phys. Rev. B* **74**, 054403 (2006).

[59] Tserkovnyak, Y., Skadsem, H. J., Brataas, A. & Bauer, G. E. W. Current-induced magnetization dynamics in disordered itinerant ferromagnets. *Phys. Rev. B* **74**, 144405 (2006).

[60] Xiao, J. A., Zangwill, A. & Stiles, M. D. Spin-transfer torque for continuously variable magnetization. *Phys. Rev. B* **73**, 054428 (2006).

[61] Ohe, J. & Kramer, B. Dynamics of a domain wall and spin-wave excitations driven by a mesoscopic current. *Phys. Rev. Lett.* **96**, 027204 (2006).

[62] Krueger, B., Pfannkuche, D., Bolte, M., Meier, G. & Merkt, U. Current-driven domain-wall dynamics in curved ferromagnetic nanowires. *cond-mat* 0608680 (2006).

[63] Shibata, J., Tatara, G. & Kohno, H. Effect of spin current on uniform ferromagnetism: Domain nucleation. *Phys. Rev. Lett.* **94**, 076601 (2005).

[64] Fernandez-Rossier, J., Braun, M., Nunez, A. S. & MacDonald, A. H. Influence of a uniform current on collective magnetization dynamics in a ferromagnetic metal. *Phys. Rev. B* **69**, 174412 (2004).

[65] Waintal, X. & Viret, M. Current-induced distortion of a magnetic domain wall. *Europhys. Lett.* **65**, 427–433 (2004).

[66] Viret, M., Vanhaverbeke, A., Ott, F. & Jacquinot, J. F. Current induced pressure on a tilted magnetic domain wall. *Phys. Rev. B* **72**, 140403 (2005).

[67] Parkin, S. S. P. *US Patent* **6898132 B2** (2004).

[68] Cowburn, R. P. & Welland, M. E. Room temperature magnetic quantum cellular automata. *Science* **287**, 1466–1468 (2000).

[69] Allwood, D. A. *et al.* Submicrometer ferromagnetic not gate and shift register. *Science* **296**, 2003–2006 (2002).

[70] Allwood, D. A. *et al.* Magnetic domain-wall logic. *Science* **309**, 1688–1692 (2005).

[71] Imre, A. *et al.* Majority logic gate for magnetic quantum-dot cellular automata. *Science* **311**, 205–208 (2006).

[72] Klaui, M. *et al.* Direct observation of domain-wall pinning at nanoscale constrictions. *Appl. Phys. Lett.* **87**, 102509 (2005).

[73] Thomas, L. *et al.* Observation of injection and pinning of domain walls in magnetic nanowires using photoemission electron microscopy. *Applied Physics Letters* **87**, 262501 (2005).

[74] Hayashi, M. *et al.* Dependence of current and field driven depinning of domain walls on their structure and chirality in permalloy nanowires. *Phys. Rev. Lett.* **97**, 207205 (2006).

[75] Thomas, L. *et al.* Oscillatory dependence of current-driven magnetic domain wall motion on current pulse length. *Nature* **443**, 197–200 (2006).

[76] Hayashi, M. *et al.* Influence of current on field-driven domain wall motion in permalloy nanowires from time resolved measurements of anisotropic magnetoresistance. *Phys. Rev. Lett.* **96**, 197207 (2006).

[77] Hayashi, M. *et al.* Current driven domain wall velocities exceeding the spin angular momentum transfer rate in permalloy nanowires. *Phys. Rev. Lett.* (accepted).

[78] Hayashi, M., Thomas, L., Rettner, C., Moriya, R. & Parkin, S. S. P. Direct observation of the coherent precession of magnetic domain walls propagating along permalloy nanowires. *Nature Phys.* (in press).

[79] Gilbert, T. L. A phenomenological theory of damping in ferromagnetic materials. *IEEE Trans. Magn.* **40**, 3443–3449 (2004).

[80] Koopmans, B., Ruigrok, J. J. M., Longa, F. D. & de Jonge, W. J. M. Unifying ultrafast magnetization dynamics. *Phys. Rev. Lett.* **95**, 267207 (2005).

[81] Levy, P. M. & Zhang, S. F. Resistivity due to domain wall scattering. *Phys. Rev. Lett.* **79**, 5110–5113 (1997).

[82] Tatara, G. & Fukuyama, H. Resistivity due to a domain wall in ferromagnetic metal. *Phys. Rev. Lett.* **78**, 3773–3776 (1997).

[83] Simanek, E. Spin accumulation and resistance due to a domain wall. *Phys. Rev. B* **6322**, 224412 (2001).

[84] Ruediger, U., Yu, J., Zhang, S., Kent, A. D. & Parkin, S. S. P. Negative domain wall contribution to the resistivity of microfabricated fe wires. *Phys. Rev. Lett.* **80**, 5639–5642 (1998).

[85] Klein, L. *et al.* Domain wall resistivity in srruo3. *Phys. Rev. Lett.* **84**, 6090–6093 (2000).

[86] Ebels, U., Radulescu, A., Henry, Y., Piraux, L. & Ounadjela, K. Spin accumulation and domain wall magnetoresistance in 35 nm co wires. *Phys. Rev. Lett.* **84**, 983–986 (2000).

[87] Kent, A. D., Yu, J., Rudiger, U. & Parkin, S. S. P. Domain wall resistivity in epitaxial thin film microstructures. *J. Phys. Condensed Matter* **13**, R461–R488 (2001).

[88] Danneau, R. *et al.* Individual domain wall resistance in submicron ferromagnetic structures. *Phys. Rev. Lett.* **88**, 157201 (2002).

[89] Prieto, J. L., Blamire, M. G. & Evetts, J. E. Magnetoresistance in a constricted domain wall. *Phys. Rev. Lett.* **90**, 027201 (2003).

[90] Pereira, R. G. & Miranda, E. Domain-wall scattering in an interacting one-dimensional electron gas. *Phys. Rev. B* **69**, 140402 (2004).

[91] Tang, H. X., Masmanidis, S., Kawakami, R. K., Awschalom, D. D. & Roukes, M. L. Negative intrinsic resistivity of an individual domain wall in epitaxial (ga,mn)as microdevices. *Nature* **431**, 52–56 (2004).

[92] Buntinx, D., Brems, S., Volodin, A., Temst, K. & Van Haesendonck, C. Positive domain wall resistance of 180 degrees neel walls in co thin films. *Phys. Rev. Lett.* **94**, 017204 (2005).

[93] Chiba, D., Yamanouchi, M., Matsukura, F., Dietl, T. & Ohno, H. Domain-wall resistance in ferromagnetic (ga,mn)as. *Phys. Rev. Lett.* **96**, 096602 (2006).

[94] Tatara, G. *et al.* Threshold current of domain wall motion under extrinsic pinning, beta-term and non-adiabaticity. *J. Phys. Soc. Jpn.* **75**, 064708 (2006).

[95] Thiele, A. A. Steady-state motion of magnetic domains. *Phys. Rev. Lett.* **30**, 230 (1973).

[96] Nakatani, Y., Thiaville, A. & Miltat, J. Head-to-head domain walls in soft nano-strips: a refined phase diagram. *J. Magn. Magn. Mater.* **290**, 750–753 (2005). Part 1 Sp. Iss. SI.

[97] McMichael, R. D. & Donahue, M. J. Head to head domain wall structures in thin magnetic strips. *IEEE Trans. Magn.* **33**, 4167–4169 (1997). Part 2.

[98] Laufenberg, M. *et al.* Quantitative determination of domain wall coupling energetics. *Appl. Phys. Lett.* **88**, 212510 (2006).

[99] Smit, J. Magnetoresistance of ferromagnetic metals and alloys at low temperatures. *Physica* **17**, 612–627 (1951).

[100] Campbell, I. A., Fert, A. & Pomeroy, A. R. Evidence for 2 current conduction iron. *Phil. Mag.* **15**, 977 (1967).

[101] Fert, A. & Campbell, I. A. 2-current conduction in nickel. *Phys. Rev. Lett.* **21**, 1190 (1968).

[102] Campbell, I. A., Fert, A. & Jaoul, O. Spontaneous resistivity anisotropy in ni-based alloys. *J.Phys. C Solid State Phys.* **3**, 95 (1970).

[103] Jaoul, O., Campbell, I. A. & Fert, A. Spontaneous resistivity anisotropy in ni-alloys. *J. Magn. Magn. Mater.* **5**, 23–34 (1977).

[104] Campbell, I. A. & Fert, A. *Transport properties of ferromagnets*, vol. 3 of *Ferromagnetic Materials* (North-Holland, 1982).

[105] Baibich, M. N. *et al.* Giant magnetoresistance of (001)fe/(001) cr magnetic superlattices. *Phys. Rev. Lett.* **61**, 2472–2475 (1988).

[106] Pratt, W. P. *et al.* Perpendicular giant magnetoresistances of ag/co multilayers. *Phys. Rev. Lett.* **66**, 3060–3063 (1991).

[107] Yuasa, H., Kamiguchi, Y. & Sahashi, M. Dual spin valves with nano-oxide layers. *J. Magn. Magn. Mater.* **267**, 53–59 (2003).

[108] Miyazaki, T. & Tezuka, N. Giant magnetic tunneling effect in fe/al2o3/fe junction. *J. Magn. Magn. Mater.* **139**, L231–L234 (1995).

[109] Moodera, J. S., Kinder, L. R., Wong, T. M. & Meservey, R. Large magnetoresistance at room-temperature in ferromagnetic thin-film tunnel-junctions. *Phys. Rev. Lett.* **74**, 3273–3276 (1995).

[110] Parkin, S. S. P. *et al.* Giant tunnelling magnetoresistance at room temperature with mgo (100) tunnel barriers. *Nature Mater.* **3**, 862–867 (2004).

[111] Yuasa, S., Nagahama, T., Fukushima, A., Suzuki, Y. & Ando, K. Giant room-temperature magnetoresistance in single-crystal fe/mgo/fe magnetic tunnel junctions. *Nature Mater.* **3**, 868–871 (2004).

[112] Hayakawa, J. *et al.* Current-driven magnetization switching in cofeb/mgo/cofeb magnetic tunnel junctions. *Jpn. J. Appl. Phys.* **44**, L1267–L1270 (2005).

[113] Schrag, B. D. *et al.* Neel "orange-peel" coupling in magnetic tunneling junction devices. *Appl. Phys. Lett.* **77**, 2373–2375 (2000).

[114] Parkin, S. S. P., More, N. & Roche, K. P. Oscillations in exchange coupling and magnetoresistance in metallic superlattice structures - co/ru, co/cr, and fe/cr. *Phys. Rev. Lett.* **64**, 2304–2307 (1990).

[115] Parkin, S. S. P., Bhadra, R. & Roche, K. P. Oscillatory magnetic exchange coupling through thin copper layers. *Phys. Rev. Lett.* **66**, 2152–2155 (1991).

[116] McGuire, T. R. & Potter, R. I. Anisotropic magnetoresistance in ferromagnetic 3d alloys. *IEEE Trans. Magn.* **11**, 1018–1038 (1975).

[117] Mitchell, E. N., Bale, H. D., Haukaas, H. B. & Streeper, J. B. Compositional and thickness dependence of ferromagnetic anisotropy in resistance of iron-nickel films. *J. Appl. Phys.* **35**, 2604 (1964).

[118] Silva, T. J., Lee, C. S., Crawford, T. M. & Rogers, C. T. Inductive measurement of ultrafast magnetization dynamics in thin-film permalloy. *J. Appl. Phys.* **85**, 7849–7862 (1999).

[119] Aharoni, A. Demagnetizing factors for rectangular ferromagnetic prisms. *J. Appl. Phys.* **83**, 3432–3434 (1998).

[120] Neudecker, I. *et al.* Spatially resolved dynamic eigenmode spectrum of co rings. *Phys. Rev. Lett.* **96**, 057207 (2006).

[121] Schrefl, T., Fidler, J., Kirk, K. J. & Chapman, J. N. Domain structures and switching mechanisms in patterned magnetic elements. *J. Magn. Magn. Mater.* **175**, 193–204 (1997).

[122] Bolte, M. *et al.* Magnetotransport through magnetic domain patterns in permalloy rectangles. *Phys. Rev. B* **72**, 224436 (2005).

[123] Scheinfein, M. R. Llg micromagnetics simulator.

[124] Yamaguchi, A. *et al.* Effect of joule heating in current-driven domain wall motion. *Appl. Phys. Lett.* **86**, 012511 (2005).

[125] Ishida, T., Kimura, T. & Otani, Y. Current-induced vortex displacement and annihilation in a single permalloy disk. *Phys. Rev. B* **74**, 014424 (2006).

[126] Sandler, G. M., Bertram, H. N., Silva, T. J. & Crawford, T. M. Determination of the magnetic damping constant in nife films. *J. Appl. Phys.* **85**, 5080–5082 (1999). Part 2A.

[127] Dorleijn, J. W. F. Electrical conduction in ferromagnetic metals. *Philips Res. Rep.* **31**, 287 (1976).

[128] Bass, J. & Jr., W. P. P. Current-perpendicular (cpp) magnetoresistance in magnetic metallic multilayers. *J. Magn. Magn. Mater.* **200**, 274–289 (1999).

[129] Sixtus, K. J. & Tonks, L. Propagation of large barkhausen discontinuities. *Phys. Rev.* **37**, 930 (1931).

[130] Tsang, C. H. & White, R. L. Transit-time measurements of domain-wall mobilities in yfeo3. *J. Appl. Phys.* **49**, 6052–6062 (1978).

[131] Ono, T. *et al.* Propagation of a magnetic domain wall in a submicrometer magnetic wire. *Science* **284**, 468–470 (1999).

[132] Schryer, N. L. & Walker, L. R. Motion of 180 degrees domain-walls in uniform dc magnetic-fields. *J. Appl. Phys.* **45**, 5406–5421 (1974).

[133] Nakatani, Y., Thiaville, A. & Miltat, J. Faster magnetic walls in rough wires. *Nature Mater.* **2**, 521–523 (2003).

[134] Ideshita, T., Fukushima, Y., Honda, S. & Kusuda, T. Dynamic collapse experiment in presence of inplane field. *IEEE Trans. Magn.* **13**, 1166–1168 (1977).

[135] Honda, S., Fukuda, N. & Kusuda, T. Mechanisms of bubble-wall radial motion deduced from chirality switching and collapse experiments using fast-rise bias field pulse. *J. Appl. Phys.* **52**, 5756–5762 (1981).

[136] Zimmermann, L. & Miltat, J. Instability of bubble radial motion associated with chirality changes. *J. Magn. Magn. Mater.* **94**, 207–214 (1991).